

POLITECNICO DI TORINO

Laurea Magistrale in Ingegneria Meccanica



**Politecnico
di Torino**

Master's Degree Thesis

**Investigation of dynamic gas bearings for
microturbomachinery**

Relatore: Prof. Federico Colombo

Candidato: Santiago Casas Ricca

Correlatori: Ing. Luigi Lentini
Ing. Edoardo Goti

A.A. 2024 / 25

Acknowledgments

I would like to express my deepest gratitude to Professor Federico Colombo, whose guidance, expertise, and support were invaluable throughout the development of this work. His insightful advice and encouragement greatly contributed to the successful completion of this thesis.

A special thanks to Ing. Luigi Lentini and Ing. Edoardo Goti, who closely followed this research and provided continuous feedback, technical discussions, and valuable suggestions. Their commitment and willingness to assist at every stage of the project played a crucial role in all the aspects of the development of this work, as well as my development as a professional.

I would also like to extend my appreciation to my colleagues and peers who provided support and shared insightful discussions, helping me navigate challenges along the way. Lastly, I am grateful to my family and friends for their unwavering encouragement and support throughout this journey.

Abstract

Due to their advantageous characteristics, gas-lubricated bearings are increasingly being adopted in various oil-free applications. These bearings utilize a gas lubricant that is directly sourced from the working fluid of the rotating machine. Furthermore, self-acting bearings eliminate the need for an external supply system or compressor, allowing for the development of compact and hermetically sealed systems. The low viscosity of gaseous lubricants also helps minimize frictional losses, thereby enhancing the overall efficiency of rotating machinery. Another key advantage of gaseous lubricants is their stable physical and chemical properties, as they do not undergo vaporization, cavitation, decomposition, or solidification across a broad temperature range.

However, the design of these bearings must be specifically tailored to meet the operational requirements of the system. This thesis presents a study on various types of aerodynamic thrust bearings, aiming to establish performance metrics for the existing bearings, develop accurate numerical models, and propose future improvements to the system.

A previously designed test bench was utilized to experimentally evaluate two types of thrust bearings: logarithmic spiral and tapered. Since no prior data were available on their exact geometry, a complete surface scan was performed to characterize the groove pattern and other relevant parameters, ensuring accurate comparisons with the numerical model. The simulation of the system was conducted using a Finite Difference Method (FDM), employing a central node finite volume mesh and a Forward Euler scheme for temporal evolution. While this approach required an exceptionally small time step (dt), leading to long computational times, it was necessary due to the highly coupled nature of the governing equations.

The bearings were scanned, and the resulting geometries were directly integrated into the numerical models for validation against the experimental measurements. Both steady-state and time-evolution models were developed and utilized to simulate the system's behavior, providing a comprehensive analysis of aerodynamic thrust bearing performance.

Contents

1	Introduction	1
1.1	Functioning principles	2
1.1.1	Step bearing	3
1.1.2	Compound bearing	3
1.2	Studied thrust bearing types	4
1.2.1	Spiral bearing	4
1.2.2	Tapered bearing	6
1.3	State of the art	8
1.3.1	Rimpel and colleagues study	9
1.3.2	Waumans study	12
1.4	Thesis Aim	16
2	Experimental Setup	17
2.1	Ball bearing turbine test bench	17
2.1.1	Turbines	19
2.1.2	Mass flow rate	21
2.2	Thrust bearing test bench	22
2.3	Sensors and repeatability	25
2.4	Measuring procedure	28
2.5	Roundmeter bearing surface scan	30
2.5.1	Scan procedure	32
3	Numerical Model	33
3.1	Reynolds Equation	33
3.2	Finite Differences Method	35
3.2.1	Discretization of equations	35
3.2.2	Meshing	37
3.2.3	Symmetry	39
3.2.4	Spiral bearing mesh generation	41
4	Results	46
4.1	Turbine Measurements	46
4.1.1	Angular Speed	46
4.1.2	Velocity Triangles	48
4.1.3	Optimization	50
4.2	Aerodynamic Thrust Bearings	51
4.2.1	Thrust Bearing Simulations	51
4.2.2	Slider	53
4.2.3	Step	56

4.2.4	Tapered	60
4.2.5	Spiral	71
4.2.6	Comparisons	88
5	Conclusions	92
6	Annex	95

List of Figures

1.1	Diagram of the Slider bearing characteristic geometry	2
1.2	Diagram of the Step bearing characteristic geometry	3
1.3	Diagram of the tapered thrust bearing surfaces	3
1.4	Parameters of an aerodynamic Spiral Grooved thrust bearing	5
1.5	Groove depth notation for aerodynamic thrust bearing	5
1.6	Picture of the studied spiral thrust bearing	6
1.7	Diagram of the tapered thrust bearing surfaces	7
1.8	Picture of the studied tapered thrust bearing	8
1.9	Isometric view of the test bench employed in the study	10
1.10	Cutaway view of the test bench employed in the study	10
1.11	Combined bearing power loss for different speeds and case pressures .	11
1.12	Relative rotor axial position versus speed during low case pressure test, no external thrust load	12
1.13	Identification of internal thrust force at 80 krpm and low case pressure	12
1.14	Exploded view of the test bench employed in the study	13
1.15	Cutaway view and visual description of the data acquisition for the test bench employed in the study	13
1.16	Design parameters and nomenclature of the inward pumping spiral geometry (a) and the herringbone geometry (b).	14
1.17	Investigation of the influence of the design parameters on the load- carrying capacity: effect of groove angle α (left top), groove number N_g (left bottom), depth ratio d_g/h (right top), and width ratio θ_g/θ (right bottom).	14
1.18	Comparison of simulated and experimentally obtained load versus clearance characteristic for the inward spiral geometry at different values of the rotational speed. The correction for the shaft length variation, due to the Poisson effect, is taken into account. The 3σ - error band which reflects the uncertainties on the measurements is also shown	15
1.19	Finite element calculation showing the rotor deformation due to cen- trifugal forces at a rotational speed of 240 000 rpm.	15
2.1	CAD of the test bench used to evaluate the turbine designs	18
2.2	Top view of the used turbine testing test bench	19
2.3	Picture of the used turbine testing test bench	19
2.4	Pelton turbine picture	20
2.5	Pelton turbine CAD Isometric view	20
2.6	Single paddle turbine picture	20
2.7	Single paddle turbine CAD Isometric view	20

2.8	Flat turbine picture	20
2.9	Flat turbine CAD Isometric view	20
2.10	Comparison between the experimental and theoretical values of the mass flow rate	22
2.11	Test bench system diagram	23
2.12	Test bench CAD Isometric view	23
2.13	Picture of the test bench and the experimental setup	24
2.14	Cutaway view of the Test Bench	24
2.15	Sensor picture taken from Monarch's web page	25
2.16	Speed sensor's position in the test bench	26
2.17	Lion Precision CPL190 isometric view	26
2.18	Lion Precision CPL190 front view	27
2.19	Lion Precision C5-0.8-2.0 probe picture	27
2.20	Micro Epsilon capaNC DT 6200 controller picture	28
2.21	Picture of the test bench at minimum inclination	29
2.22	Picture of the test bench at a tested inclination (maximum in this case)	29
2.23	Setup for the surface scan	31
2.24	Graphical results in the roundmeter software	31
3.1	Diagram of a partial Control Volume of the system	33
3.2	Representation of the mass flow through the control volume	35
3.3	Diagram of an element in the FDM mesh	36
3.4	Diagram of the circular mesh	38
3.5	Diagram of the 2D plane mesh	39
3.6	Example of a 30° sector mesh	40
3.7	3D view of the spiral bearing mesh example	40
3.8	Example of the mesh of 1 pad ($\frac{1}{6}$ of the surface)	41
3.9	Function "getGrooves" initialization	42
3.10	Spiral groove curve representation diagram	43
3.11	Spiral bearing characteristic parameters and groove boundary equa- tions definition	43
3.12	Grooved points identification 1 st part	44
3.13	Grooved points identification 2 nd part	44
4.1	Pelton turbine Angular speed vs Experimental Volumetric Flow rate .	47
4.2	Single turbine Angular speed vs Experimental Volumetric Flow rate .	47
4.3	Flat turbine Angular speed vs Experimental Volumetric Flow rate . .	48
4.4	Velocity triangles of a generic Pelton turbine	48
4.5	Pelton turbine Hydraulic efficiency	49
4.6	Single turbine Hydraulic efficiency	50
4.7	Load capacity W as a function of the air gap h at the minimum rotational speed $\omega_{min} = 5 \text{ krpm}$	52
4.8	Slider bearing simulated pressure field in the static simulation	54
4.9	Slider bearing s_H depiction	54
4.10	Slider bearing, Slider depth vs load capacity	55
4.11	Initial generic geometry vs optimized geometry	56
4.12	Step bearing simulated pressure field in the static simulation	57
4.13	Bearing side section depicting s_H and a	57
4.14	Diagram depicting a from the top view	58

4.15	Step bearing, step depth and step sector effects on load capacity, default view	58
4.16	Step bearing, step depth and step sector effects on load capacity, $X - Y$ plane view	59
4.17	Initial generic geometry vs optimized geometry	60
4.18	Roundmeter setup for the measurement of the Tapered bearing	61
4.19	Tilted Bearing Surface raw data	62
4.20	Tapered Bearing Surface flattened	62
4.21	Tapered Bearing Surface scan in Matlab	63
4.22	Tapered Bearing inner radius pad depth	64
4.23	Tapered Bearing middle radius pad depth	65
4.24	Tapered Bearing outer radius pad depth	65
4.25	Tapered Bearing average profile	66
4.26	Tapered Bearing average profile, top view	66
4.27	Tapered Bearing simulated pressure field using the FDM method	67
4.28	Tapered Bearing dynamic simulation with measured air gaps	68
4.29	Tapered Bearing side section depicting s_H and a	69
4.30	Diagram depicting a from the top view	69
4.31	Tapered bearing, maximum groove depth s_h and taper sector a effects on load capacity	69
4.32	Tapered bearing, maximum groove depth s_h and taper sector a effects on load capacity, top view	70
4.33	Tapered bearing load capacity comparison between initial and optimized parameters at $\omega_{min} = 5 \text{ krpm}$	71
4.34	Spiral Bearing Surface scan raw data	72
4.35	Spiral Bearing Surface scan raw data side view	72
4.36	Plane fitting using curve fitter	73
4.37	Flattened geometry top view	74
4.38	Flattened geometry side view	74
4.39	Filtered and Flattened geometry data	75
4.40	Parameters of an aerodynamic Spiral Grooved thrust bearing	76
4.41	Graphical comparison and verification of the parameters of the bearing	77
4.42	Isolated data from the grooves	78
4.43	Isolated data from the non-grooved part of the bearing	78
4.44	30° Sector meshed with average radial depth applied to the mesh	79
4.45	Isometric view of the pressure field of the studied spiral bearing section	80
4.46	Top view of the pressure field of the studied spiral bearing section	81
4.47	Spiral Thrust bearing theoretical load capacity under static conditions	82
4.48	Spiral Thrust bearing theoretical load capacity under static conditions	83
4.49	Spiral bearing optimization for α and γ	84
4.50	Spiral bearing optimization for α and γ , top view	84
4.51	Spiral bearing optimization for δ and Γ	85
4.52	Spiral bearing optimization for δ and Γ , top view	85
4.53	Original geometry	86
4.54	Optimized geometry	87
4.55	Original geometry vs optimized geometry	88
4.56	Bearing type comparison, $h_2 = 10 \mu m$	89
4.57	Bearing type comparison, $h_2 = 12 \mu m$	89

4.58	Bearing type comparison, $h_2 = 14 \mu m$	90
4.59	Bearing type comparison, $h_2 = 16 \mu m$	90
4.60	Bearing type comparison, $h_2 = 18 \mu m$	91
4.61	Bearing type comparison, $h_2 = 20 \mu m$	91

List of Tables

1.1	Spiral bearing parameters	6
2.1	Ball bearing test bench list of components	18
2.2	Test bench part list	25
4.1	Maximum time step Δt for the dynamic model for each geometry . .	52
4.2	Angular tilt of every pad present in the bearing	64
4.3	Measured properties of the grooved spiral bearing	76
4.4	Optimal parameters of the spiral bearing	86

Chapter 1

Introduction

Whenever a rotating system is designed with the intention of having a shaft rotate at extremely high speeds, normal ball bearings have a major drawback, they generate enough friction to get damaged or even fail catastrophically. To combat this issue, gas bearings can be implemented instead of regular contact bearings. This is a staple in applications where a high speed shaft is required, such as high precision machining, surface finishing, manufacturing of components at a microscopic level, among many others.

Gas bearings, particularly aerostatic journal bearings, offer several significant advantages. One of the primary benefits is their ability to operate without physical contact between moving parts, resulting in wearless operation, which enhances their longevity and reduces maintenance requirements. In addition, gas bearings provide exceptional guiding, repeatability, and position accuracy, making them ideal for high-precision applications. The absence of liquids reduces the risk of contamination and ensures environmental cleanliness, making gas bearings suitable for semiconductor manufacturing and aerospace applications. Moreover, they can achieve extremely high rotational speeds and precision due to their minimal friction. However, gas bearings also have drawbacks, including their sensitivity to external contaminants and the need for a continuous supply of clean, dry gas, which can complicate their design and increase operational costs. Their load-carrying capacity is generally lower than that of traditional bearings, which may limit their use in heavy-duty applications. Additionally, the tight manufacturing tolerances required for gas bearings can increase production complexity and costs. Understanding these pros and cons is crucial for selecting the appropriate bearing type for specific engineering applications and optimizing their performance in various operational contexts.

Due to their advantageous characteristics, gas-lubricated bearings are increasingly being adopted in various oil-free applications. These bearings utilize a gas lubricant that is directly derived from the working gas processed by the rotating machine. Furthermore, self-acting bearings eliminate the need for an external supply system or compressor, enabling the development of compact and hermetically sealed systems. The low viscosity of gaseous lubricants also helps minimize frictional losses, thereby enhancing the overall efficiency of rotating machinery. Another key benefit of gaseous lubricants lies in their stable physical and chemical properties, as they do not undergo vaporization, cavitation, decomposition, or solidification across a broad temperature range.

However, the low viscosity of gas lubricants also imposes limitations, particularly in

terms of load capacity and damping. This, combined with cross-coupled effects, can lead to rotordynamic instabilities. Typically, these issues are mitigated by reducing the clearance-to-diameter ratio or incorporating external damping mechanisms. However, accurately predicting the dynamic behavior of such systems remains a challenge due to the complex response of the viscoelastic support materials.

As the demand for lighter, more compact, cost-effective, and environmentally friendly energy conversion systems continues to grow, gas bearings play an increasingly vital role in oil-free turbomachinery. Their advantages have been demonstrated in a range of applications, including turbocompressors, gas turbines, and turbochargers/expanders. The power output of gas-bearing-supported turbomachinery varies widely, spanning from approximately 10 W to 200 kW, while rotor speeds range from 10,000 rpm to beyond 1,000,000 rpm.

The proper operation of an aerodynamic grooved thrust bearing relies on the balance between the fluid pumped toward the bearing's center—known as the pump effect—and the fluid lost due to leakage. Leakage occurs as a result of the pressure generated by the pump effect and is influenced by the depth of the grooves. If the grooves are too deep, leakage becomes excessive, whereas if the grooves are completely absent, the pump effect is eliminated entirely.

1.1 Functioning principles

Unlike aerostatic bearings, which rely on an external pressurized gas supply, aerodynamic bearings generate their own pressure through the relative motion of the surfaces and the presence of a convergence in the direction of the relative velocity between the surfaces. This self-acting mechanism makes them suitable for high-speed, oil-free applications, such as turbomachinery and microturbines. The performance of these bearings is highly dependent on their geometry, which dictates the formation and stability of the gas film.

The first aerodynamic thrust bearing geometry was the *Slider Bearing*. This bearing consisted in a series of angled surfaces which create a converging air gap between the rotating shaft and the stationary bearing. A simple diagram depicting this geometry can be observed in **Figure 1.1**.

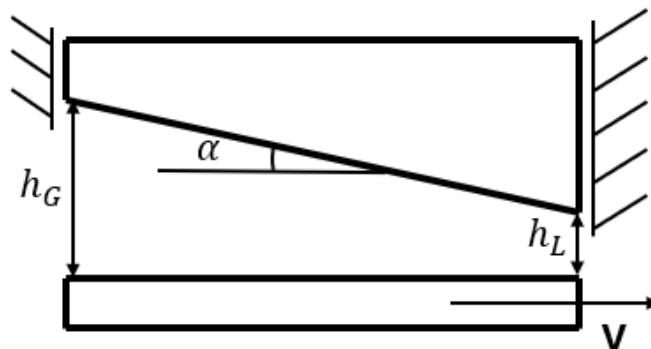


Figure 1.1: Diagram of the Slider bearing characteristic geometry

Several key aerodynamic bearing geometries exist, each designed to optimize the pressure buildup and load-carrying capacity. The figures from the reference document illustrate some of the most widely used configurations. Some of these types are

presented in *Meccanica Applicata* [1] by Raparelli and Ferraresi and will be discussed in the following section.

1.1.1 Step bearing

A flat bearing with a constant film thickness does not generate any load-carrying capacity. However, if the bearing surface is designed with a series of steps, as shown in **Figure 1.2**, the fluid film forms multiple converging regions. This results in a pressure distribution with localized peaks at the discontinuities, enabling the bearing to support significant loads.

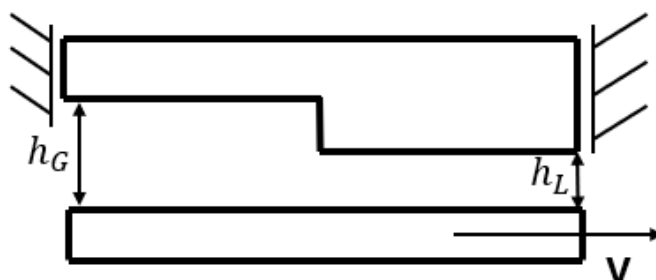


Figure 1.2: Diagram of the Step bearing characteristic geometry

A key advantage of the step bearing is its ability to reduce contact pressures between surfaces during start-up and shutdown phases. This characteristic improves the bearing's durability and performance, particularly in applications where frequent stop-start cycles are expected.

1.1.2 Compound bearing

A compound bearing is constructed by combining two flat bearing surfaces, one with zero inclination and the other with an inclination α . The schematic representation of this bearing is shown in **Figure 1.3**.

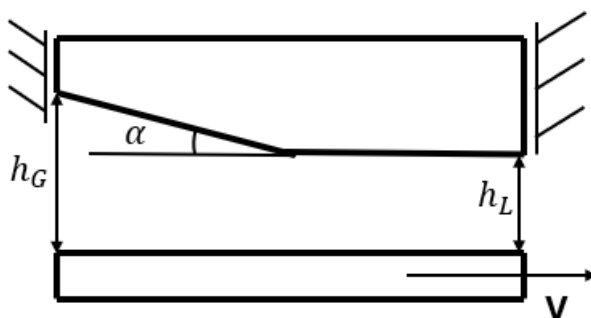


Figure 1.3: Diagram of the tapered thrust bearing surfaces

Compared to a simple wedge-shaped bearing, the compound bearing offers improved performance in terms of reducing contact pressures during start-up and shutdown phases. However, this design also results in higher steady-state friction forces and greater energy dissipation. This is due to the fact that the fluid must travel through a longer section with a reduced film thickness, increasing resistance and energy loss.

1.2 Studied thrust bearing types

1.2.1 Spiral bearing

Aerodynamic spiral thrust bearings are a type of gas-lubricated bearing designed to generate a self-sustaining pressure field through the relative motion between the rotor and the bearing surface with the convergence coming from the fact that the shaft spins in the direction in which the air enters the spirals and creates the pressure field necessary. This forementioned shaft speed is indicated in **Figure 1.4** as ω . The defining geometric feature of this type of bearing is a series of spiral grooves etched into the bearing face, which serve to pump gas toward the center as the rotor spins. This pumping action creates a pressure buildup that supports the applied load and establishes a stable gas film between the bearing and the rotor, preventing direct contact and minimizing friction. The depth, width, and pitch of these grooves are critical design parameters, as they directly influence the bearing's load capacity, stiffness, and overall performance.

Several key parameters govern the behavior of spiral thrust bearings. These are shown in **Figure 1.4** respecting *Muijderman* [5, 4] notation and listed in **Table 1.1**. The groove depth determines the balance between the pump effect and leakage, with excessively deep grooves leading to excessive fluid loss and shallow grooves reducing the pressure generation capability. The groove angle, typically optimized to maximize the pressure buildup, is another crucial factor. This groove angle is responsible for the geometry of the spiral, as it is one the two variables in the definition of the *Logarithmic spiral* present in the bearing, as described in **Equation 1.1**.

$$r = r_2 \cdot e^{\theta \tan(\beta)} \quad (1.1)$$

Additionally, the clearance or air gap between the bearing and rotor affects load capacity and stiffness, with smaller clearances generally providing higher pressure buildup but increasing sensitivity to manufacturing tolerances. Given their oil-free operation and high-speed capabilities, spiral thrust bearings are widely used in turbomachinery, microturbines, and other high-speed rotating applications where low friction and high reliability are essential.

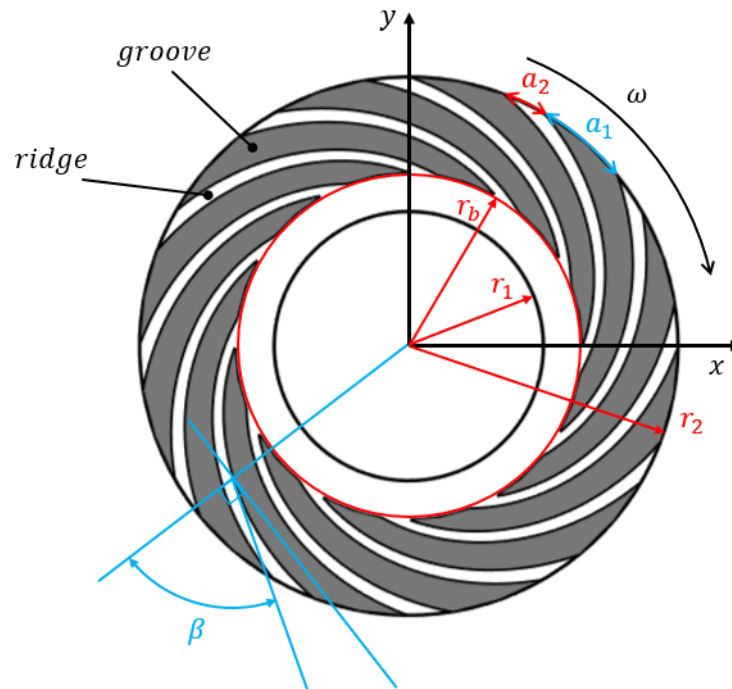


Figure 1.4: Parameters of an aerodynamic Spiral Grooved thrust bearing

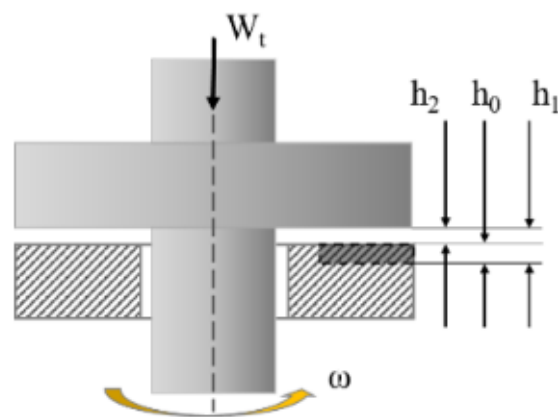


Figure 1.5: Groove depth notation for aerodynamic thrust bearing

r_1	Internal radius
r_b	Groove start radius
r_2	External radius
β	Spiral angle
a_1	Ridge sector
a_2	Groove sector
ω	Shaft rotation direction
h_0	Groove depth
h_1	Groove air gap
h_2	Nominal air gap

Table 1.1: Spiral bearing parameters

A picture of the aerodynamic spiral thrust bearing is provided in **Figure 1.6**



Figure 1.6: Picture of the studied spiral thrust bearing

Some parameters could initially be measured without the need for a complex measuring device. These were mainly the internal and external radii, with values of $r_1 = 16 \text{ mm}$ and $r_2 = 33 \text{ mm}$.

1.2.2 Tapered bearing

Tapered aerodynamic thrust bearings are a type of self-acting gas-lubricated bearing designed to generate lift and support axial loads in high-speed rotating systems. These bearings are characterized by their distinct geometry, which consists of a flat pad followed by a slanted plane that leads into a machined slot. This configuration creates a converging gap that promotes the formation of a pressure field within the gas film, enabling the bearing to generate lift and support the rotor without physical

contact. The slanted section helps establish a pressure gradient, which contributes to improved lift generation and better load distribution.

However, tapered thrust bearings also present certain drawbacks. The manufacturing complexity of the slanted geometry and machined slot increases production costs compared to simpler designs. Additionally, the bearing's performance is highly sensitive to machining tolerances, as deviations in geometry can significantly impact pressure distribution and load capacity. Another limitation is the relatively low damping characteristic of gas-lubricated systems, which can lead to challenges in maintaining stability under varying operational conditions.

Despite these challenges, tapered aerodynamic thrust bearings remain a valuable choice for high-speed, low-friction applications where oil-free operation is required. Their ability to generate lift efficiently and support axial loads makes them an essential component in advanced turbomachinery and other precision-engineered rotating systems.

In **Figure 1.7** a diagram of the air gap present between the bearing surface and the rotor surface is shown. The two marked dimensions are the nominal air gap h_L and the air gap between the lowest point of the bearing and the rotor h_G . These two parameters together with the number of pads and the angular section of the tapered sector will fully define the geometry of the bearing. In the case of this study, the only known parameter before any precise measurement (done in **Chapter 4**) is the number of pads, this being 6 as seen in **Figure 1.8**.

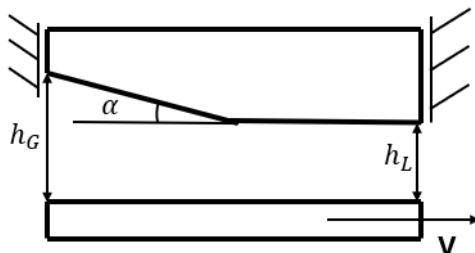


Figure 1.7: Diagram of the tapered thrust bearing surfaces



Figure 1.8: Picture of the studied tapered thrust bearing

Similarly to the spiral bearing, both internal and external radii could be measured before any other operation, and it presents the same values of $r_1 = 16\text{ mm}$ and $r_2 = 33\text{ mm}$.

1.3 State of the art

To investigate the performance of the aerodynamic thrust bearings currently in use—namely, spiral and tapered bearings—the existing test bench was employed as the primary experimental platform. This test bench provides a controlled environment where key operational parameters, such as the bearing load, rotational speed, and air supply conditions, can be systematically varied and analyzed. By utilizing this setup, it was possible to measure critical quantities, including the air gap between the bearing and the rotor, the force exerted on the bearing, and the rotational speed of the shaft. These measurements offer valuable insight into the bearings' behavior and overall system performance.

However, understanding the characteristics of these bearings in isolation is not sufficient; it is also essential to place them within the broader context of existing research. Numerous studies have been conducted on aerodynamic thrust bearings, with various experimental setups designed to test different aspects of their performance. Each of these test benches presents specific advantages and limitations, depending on the objectives of the study. Some focus on achieving high rotational speeds, while others emphasize precision in measuring film thickness and pressure distribution. By analyzing these studies, a clearer picture emerges of the strengths and weaknesses of different approaches, helping to position the present research within the ongoing efforts to refine and optimize gas-lubricated bearing systems.

In this section, a detailed review of state-of-the-art test benches used in similar

research is presented. By comparing different methodologies and their respective findings, it becomes possible to assess the effectiveness of the current setup and identify areas for potential improvement. Furthermore, this review will highlight the key challenges faced in the experimental study of aerodynamic thrust bearings, including issues related to measurement accuracy, repeatability, and system stability.

1.3.1 Rimpel and colleagues study

In their research paper *A rotordynamic, thermal, and thrust load performance gas bearing test rig and test results for tilting pad journal bearings and spiral groove thrust bearings* [7], Aaron M. Rimpel and colleagues, designed a test bench capable of testing Grooved and Tilting-Pad thrust bearings. The researchers developed a test rig, as illustrated in **Figures 1.9-1.10**, for the current test program. The test section, housing both the test shaft and bearings, was designed symmetrically from the drive end (DE) to the nondrive end (NDE), with the thrust bearing at the center and radial bearings on either side. High-speed rotor systems often face stability issues when running speeds exceed the first natural frequency. To address this, titanium was chosen for the shaft material instead of conventional steels, resulting in a rigid shaft with low inertia. This reduced the ratio of running speed to the first natural frequency and increased rigid body mode natural frequencies.

Hollow shaft designs were considered but dismissed due to significant centrifugal growth. A solid titanium shaft was preferred, as it offered a sufficient speed separation margin and lower thermal expansion, enhancing bearing stability. Aluminum dummy disks were attached to the test shaft's ends to simulate the masses of impellers on the actual machine. These disks had tapped holes for balance correction weights during high-speed balancing. The shaft assembly was initially balanced to the ISO G3.5 specification.

An air turbine, modified from an automotive turbocharger, drove the test shaft through a quill shaft coupling. The coupling adapter, replacing the turbocharger compressor, had an integral balance piston to balance turbine thrust across various speeds. The turbocharger driver frame, supported on linear ball bearings, ensured that net thrust forces were not communicated to the test section's thrust bearing.

A pneumatic thrust loader on the NDE of the shaft applied thrust force to the spinning rotor. The loader housing was attached to the test section frame, with a labyrinth seal at the outer diameter of the NDE dummy disk. Pressurization of the outboard cavity produced a thrust force toward the DE. Leakages discharged through a passage between the thrust loader and test section housings, preventing external thrust on the test section housing due to back-pressure.

The test section housing was supported on hydrostatic air bearings acting as gimbals, providing frictionless radial support while allowing axial and circumferential movement. These motions were constrained by spherical-jointed links with load cells, facilitating measurement of reaction forces on the test bearings. The thrust load measurement was more accurate than the torque measurement, mainly due to the relatively small torque produced by the bearings.

Load cells also detected the influence of plumbing lines and instrumentation wires attached to the test section housing, as well as any unbalanced internal thrust. Flexible lines and perpendicular connections to the housing minimized structural effects. Calibration of the load cell responses to known axial forces and torques

compensated for these effects. Despite the intentional symmetry of the test rig design, small levels of internal thrust were encountered during testing and were compensated for accordingly.

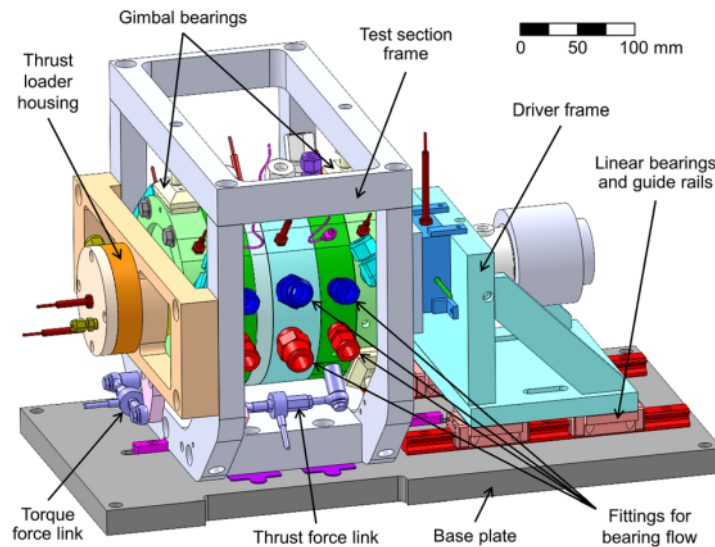


Figure 1.9: Isometric view of the test bench employed in the study

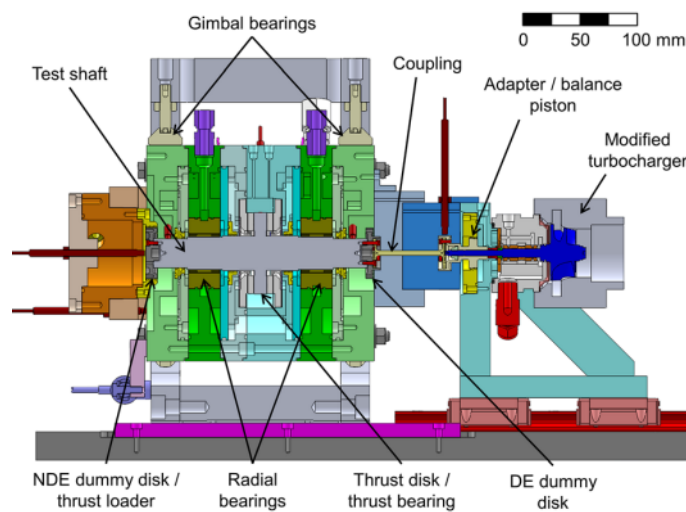


Figure 1.10: Cutaway view of the test bench employed in the study

The test rig validated rotordynamic performance and stability, quantified steady-state power loss, assessed bearing cooling performance, and tested thrust bearing load capacity. Data were sampled at 2 Hz for process data and 10 kHz for rotordynamic data.

For power loss and thermal performance, tests without externally applied thrust load were conducted at varying case pressures. The combined bearing power loss was calculated, with the thrust bearing accounting for 93% of the total power loss. The data correlated well as a cubic function of speed, with an expected increase in power loss with rising case pressure. Radial bearing power loss, observed as heat

generation, was indicated by the temperature gradient between the leading and trailing edge of the pads.

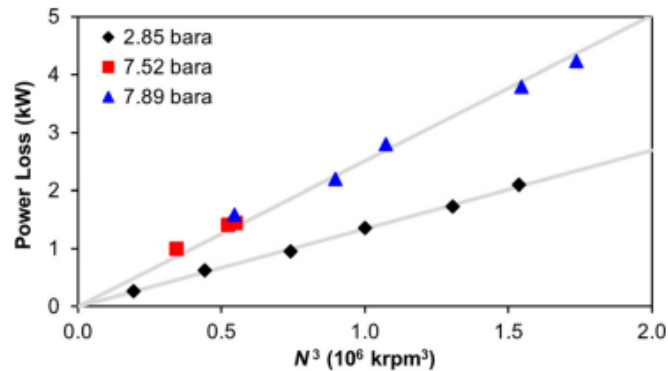


Figure 1.11: Combined bearing power loss for different speeds and case pressures

Steady-state pad temperatures for radial and thrust bearings were measured, with results showing slightly higher temperatures for high-pressure cases compared to low-pressure ones. Thrust bearing data exhibited a pronounced temperature difference due to case pressure.

During thrust capacity testing, an unintended thrust load varying with case pressure and speed was observed without any intentional load applied. Thrust bearing pad temperatures indicated that the NDE bearing experienced higher temperatures than the DE bearing, suggesting more load on the NDE with increasing speed. Rotor deflection towards the NDE increased with speed, especially above 90 krpm, despite thermal effects causing scatter in the data.

Internal thrust generated within the test section housing could not be directly measured, but was quantified by other means. The thrust loader counteracted the internal thrust, pushing the rotor towards the DE. The transition from internal thrust dominance to proportional tracking of thrust loader pressure force marked the null thrust condition, with internal thrust approximately 3% of capacity at 80 krpm.

At 80 krpm, the thrust bearing supported a maximum load of less than 35 N before rotor rub occurred. Steady vibrations indicated stable lateral and axial vibrations up to the rub. An increase in thrust force led to higher thrust bearing pad temperatures due to reduced gas film thickness, with film thickness closing more at the bearing ID than the OD, suggesting bearing pad deformation. Advanced modeling would be required to better understand and address temperature-induced deformation effects.

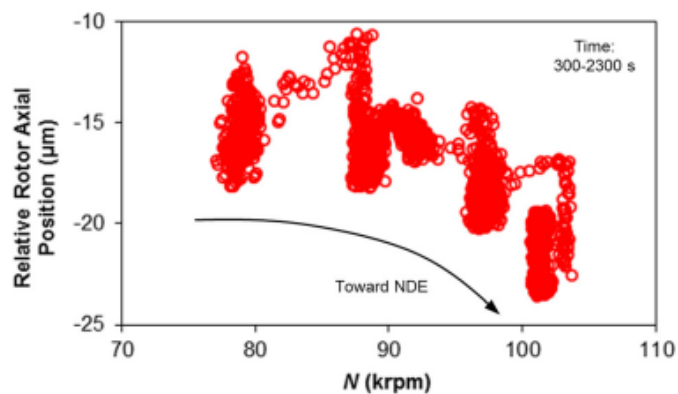


Figure 1.12: Relative rotor axial position versus speed during low case pressure test, no external thrust load

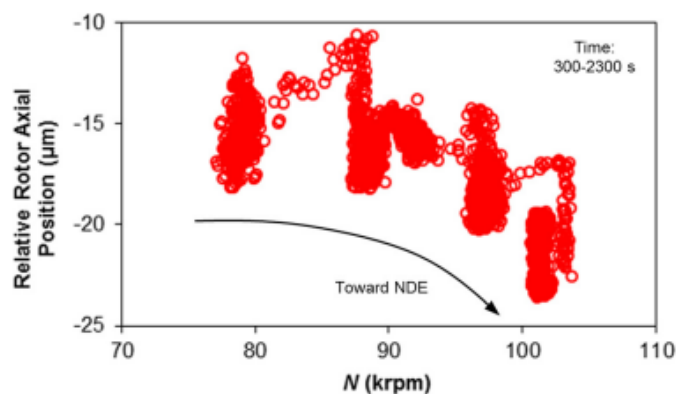


Figure 1.13: Identification of internal thrust force at 80 krpm and low case pressure

1.3.2 Waumans study

For his thesis in 2009, Tobias Waumans studied high speed air bearings, as the title of this thesis suggests [9]. The test setup included a rotor consisting of a steel shaft with a 6 mm diameter and a single shrink-fitted rotor disc made from high-strength titanium alloy (Ti6Al4V Grade 5) to limit stress. The plain aerostatic journal bearing supported the rotor at both ends, with radial clearance at $7.5 \mu\text{m}$ and feedhole radius at $75 \mu\text{m}$. A Pelton impulse turbine drove the rotor to the required speed, designed for testing up to 300,000 rpm.

The aerodynamic thrust bearing, tested on the inner side of the grooved geometry, was machined by micro-milling and fitted with an interchangeable bronze part. The rotor-bearing unit, contained within a housing, allowed precise alignment and easy access for instrumentation probes. One end of the housing was closed by a cover, while the other end had a pressure chamber that created axial load by pressurizing the rotor disc.

Careful alignment of all components was crucial for obtaining accurate test data. This setup adhered to stringent manufacturing tolerances to minimize air gap height effects.

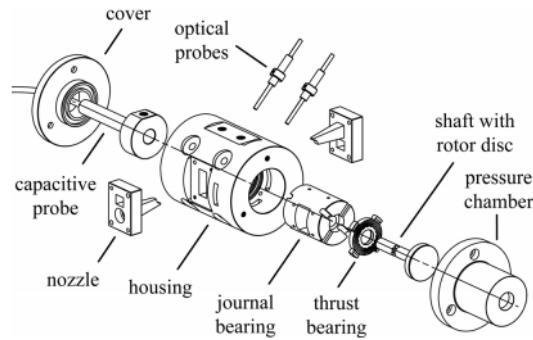


Figure 1.14: Exploded view of the test bench employed in the study

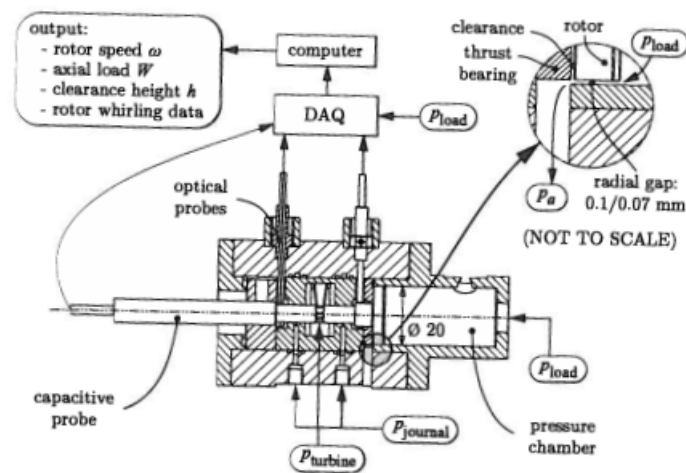


Figure 1.15: Cutaway view and visual description of the data acquisition for the test bench employed in the study

To derive design guidelines for obtaining maximal load-carrying capacity, a brief parametric study was conducted. This study focused on the load characteristics of grooved thrust bearing geometries, excluding other static film characteristics like frictional losses. The study did not incorporate the effect of groove geometry on dynamic behavior and stability, directing the reader to another section for that information.

Two typical grooved thrust bearing geometries were examined: inward pumping spiral type and herringbone type. The design parameters for these geometries were defined using logarithmic spirals, with the grooves expressed mathematically.

The parametric study evaluated how design parameters, such as groove angle α , groove depth ratio d_g/h , groove width ratio θ_g/θ , and groove number N_g , influenced load-carrying performance. The study observed that the maximal bearing load occurred when α was 17.5 degrees, d_g/h was 2.67, and θ_g/θ was 1, while N_g had a minor effect. This observation aligned with design rules found in literature for both incompressible and compressible films.

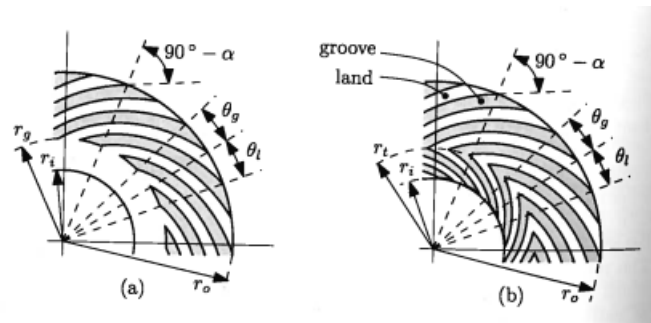


Figure 1.16: Design parameters and nomenclature of the inward pumping spiral geometry (a) and the herringbone geometry (b).

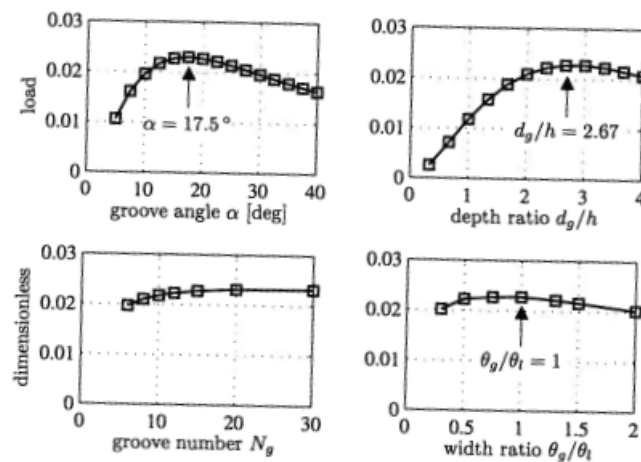


Figure 1.17: Investigation of the influence of the design parameters on the load-carrying capacity: effect of groove angle α (left top), groove number N_g (left bottom), depth ratio d_g/h (right top), and width ratio θ_g/θ (right bottom).

The performance of the test bearings was experimentally determined by recording the clearance height h against the axial load W while maintaining a constant rotational speed ω . For increased load application, pressure adjustments prevented rotor deceleration. Care was necessary during pressure adjustments to avoid abrupt rotor speed changes, which could lead to bearing seizure.

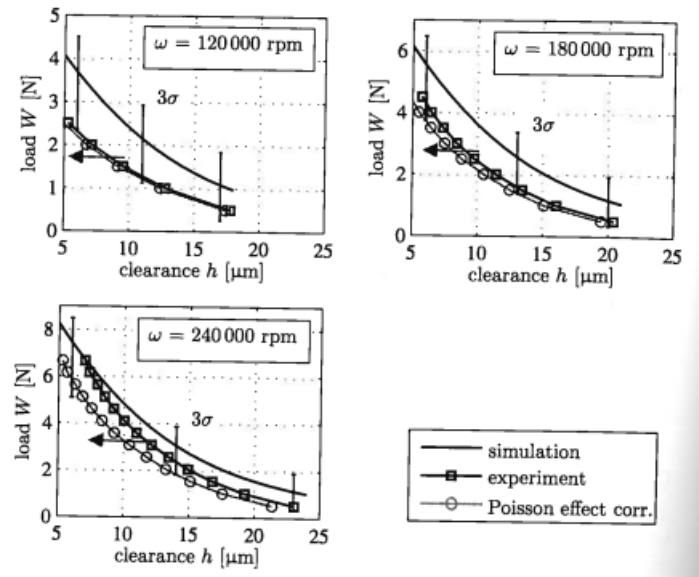


Figure 1.18: Comparison of simulated and experimentally obtained load versus clearance characteristic for the inward spiral geometry at different values of the rotational speed. The correction for the shaft length variation, due to the Poisson effect, is taken into account. The 3σ -error band which reflects the uncertainties on the measurements is also shown

Figure **Figure 1.18** shows simulated and experimental load versus clearance characteristics for inward spiral geometry at rotational speeds of 120,000 rpm, 180,000 rpm, and 240,000 rpm. The inner side of the rotor disc and the test bearing surface came into contact at high speeds, indicating rotor shaft seizure on the rightmost journal bearing. These results confirmed that the predicted load-carrying capacity exceeded the measured values by approximately 1 to 1.5 N after correcting for the Poisson effect (Figure 5.15). Qualitative agreement was observed in all experiments.

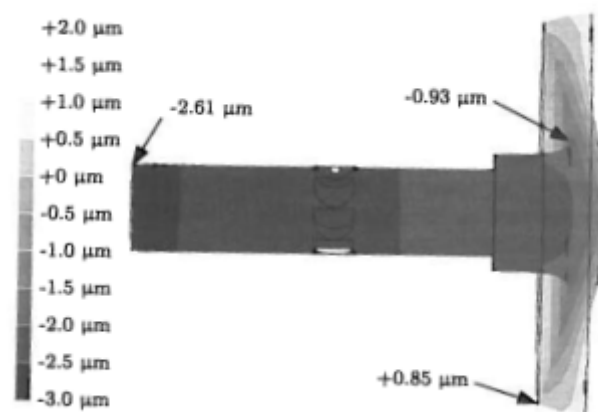


Figure 1.19: Finite element calculation showing the rotor deformation due to centrifugal forces at a rotational speed of 240 000 rpm.

Experiments with bearings having a different groove geometry did not produce reliable data, as the rotor could not support a load higher than 2 N, leading to frequent seizure.

Misalignment of the thrust bearing components likely caused faulty and unreliable measurements, making it challenging to compare load-carrying performance across different groove geometries.

The following factors contributed to the observed discrepancies:

- **Alignment Imperfections:** Non-uniform clearance height resulted from these imperfections.
- **Rotor Disc Deformation:** Centrifugal forces at high rotational speeds caused deformation, as shown in the finite element calculation (**Figure 1.19**).
- **Shaft Length Variation:** The Poisson effect induced variations, which were also illustrated in **Figure 1.19**.
- **Disturbances from Working Conditions:** Axial disturbance forces from the driving turbine, not aligned with the rotor center, added to the measurement uncertainties.

In conclusion, these effects and the corresponding error analysis, as elaborated, were critical for assessing the measurement uncertainties and aligning the experimental outcomes with predictions.

1.4 Thesis Aim

One of the primary goals is the identification of the thrust bearings currently in use, as their geometry and properties are not explicitly documented. This involves performing surface scans and measurements to accurately determine their dimensions and characteristics. Once identified, the bearings will be tested and characterized under various operating conditions to evaluate their performance, including parameters such as load capacity, stiffness, and stability.

Another key objective is to assess the functionality and accuracy of the existing test bench. This includes verifying the repeatability of measurements and ensuring that the experimental setup provides reliable data. The results obtained from these tests will be validated against a numerical model based on the Finite Difference Method (FDM), allowing for a deeper understanding of the system's behavior and enhancing the reliability of the experimental findings. Additionally, different turbine designs will be tested to evaluate their impact on the overall system efficiency. The insights gained from these experiments will contribute to future optimization efforts and improvements to the test bench, ensuring its suitability for further research and development in the field of gas-lubricated bearing systems.

Chapter 2

Experimental Setup

2.1 Ball bearing turbine test bench

The ball bearing test bench is designed to analyze the performance of various turbine configurations in a controlled environment. It consists of a rotating shaft supported by two ball bearings, each housed within its respective casing to ensure stability and reduce friction. At one end of the shaft, a magnet is housed to interact with a Hall effect sensor, which is used to measure the rotational speed of the system. On the opposite end, the turbines under investigation are mounted onto the shaft using a tight clearance fit, ensuring a secure connection while allowing for easy interchangeability.

A key component of this test bench is the air distributor, which directs airflow toward the turbine blades to drive rotation. To maintain consistency in testing conditions, the distributor is positioned precisely around the turbine using a 3D-printed alignment fixture. This fixture ensures that the distributor remains centered relative to the shaft, minimizing misalignment errors that could impact performance measurements.

The primary objective of this test bench is to evaluate the efficiency and operational characteristics of three different turbine designs, which will be detailed in the following section. The insights gained from these tests will serve as a foundation for the future development of an improved test bench specifically designed for aerodynamic thrust bearings. By optimizing turbine performance, this research aims to enhance the effectiveness of the next-generation test bench, ultimately leading to more accurate and reliable testing of aerodynamic thrust bearing systems.

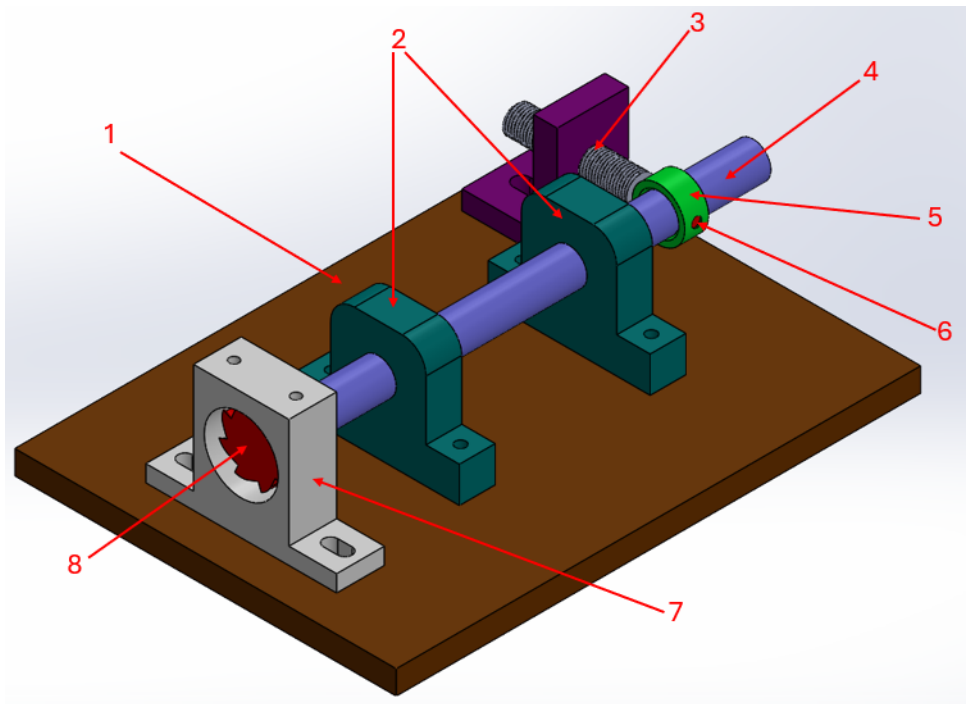


Figure 2.1: CAD of the test bench used to evaluate the turbine designs

1	Test bench base
2	Ball bearing housings
3	Hall effect sensor and sensor housing
4	Rotating shaft
5	Magnet housing
6	Magnet
7	Turbine air distributor
8	Turbine

Table 2.1: Ball bearing test bench list of components



Figure 2.2: Top view of the used turbine testing test bench

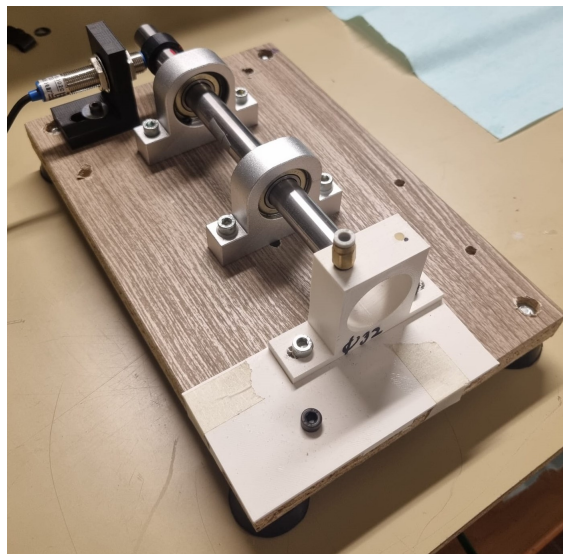


Figure 2.3: Picture of the used turbine testing test bench

2.1.1 Turbines

The design of the turbine for the aerostatic radial bearing system is equally critical, particularly in applications where rotational speed and efficiency are paramount. Various turbine designs have been explored to optimize performance, with significant contributions from studies conducted by A. Schneider^[8]. The focus of these studies has often been on impulse turbines, which are designed to convert the kinetic energy of a high-velocity jet of gas into rotational motion. Schneider's research has examined multiple blade geometries, including flat, simple curve, and double curved profiles, each offering distinct advantages in terms of airflow management and rotational efficiency. When designing a turbine for 3D printing, it is essential

to incorporate features that can be reliably produced using additive manufacturing techniques. This includes considering the layer resolution of the 3D printer and the mechanical properties of the printed material.

The experimental setup for the evaluation of the turbine performance included three designs: a flat-bladed turbine, a Pelton-style turbine with two paddles per blade, and a single-paddle turbine. Each turbine featured an external diameter of 30 mm and consisted of eight blades. These designs were chosen to analyze the impact of blade geometry on system performance. Figures showing both the CAD version and the realized version of the turbines are provided in **Figures 2.4-2.9**.



Figure 2.4: Pelton turbine picture

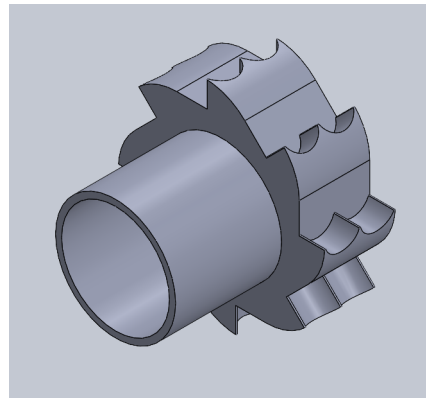


Figure 2.5: Pelton turbine CAD
Isometric view



Figure 2.6: Single paddle turbine
picture

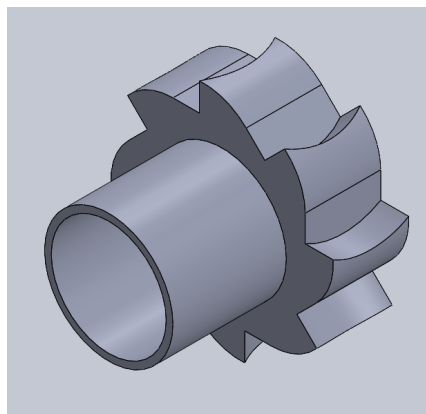


Figure 2.7: Single paddle turbine CAD
Isometric view

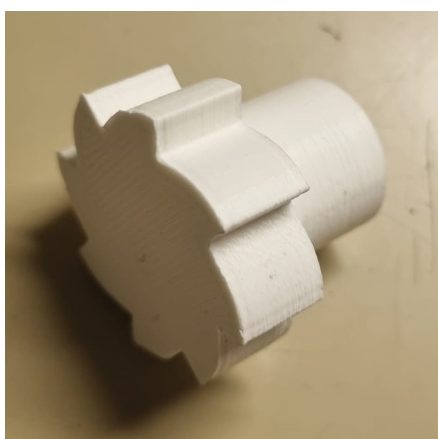


Figure 2.8: Flat turbine picture

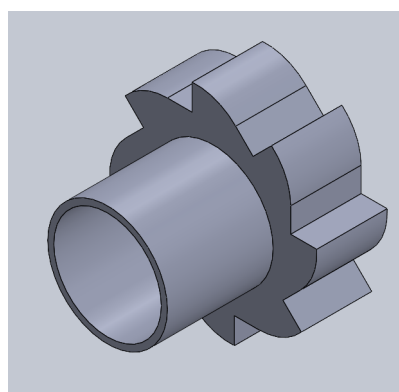


Figure 2.9: Flat turbine CAD Isometric
view

To supply air to the turbines, a distributor was 3D-printed in two configurations, with diameters of 33 mm and 32 mm, to investigate how variations in distributor geometry influence the system. The distributor design was integrated into the setup using a placeholder mechanism, ensuring consistent alignment and placement relative to the shaft and turbine through precise physical measurements.

2.1.2 Mass flow rate

The journal bearings test bench was designed to facilitate the measurement of key parameters essential for characterizing the system's performance. The measurements were done 3 separate times in order to obtain more accurate result when analyzing the system and doing calculations with the data. The measurement of the mass flow rate was compared to the theoretical mass flow rate corresponding to a given pressure. The theoretical flow rate can be calculated as a function of the pressure, using the formulas of **Equation 2.1**, taken from ISO 6358.

$$Q_{in} = c_d A p_s \frac{0.6855}{\sqrt{R_g T}} \begin{cases} \sqrt{1 - \left(\frac{p_c - b_c}{p_s \frac{1-b_c}{1-b_c}} \right)^2} & \text{if } \frac{p_c}{p_s} > b_c \\ 1 & \text{if } \frac{p_c}{p_s} \leq b_c \end{cases} \quad (2.1)$$

where $b_c = \left(\frac{2}{\kappa+1} \right)^{\frac{\kappa}{\kappa+1}}$ is the critical relation for pressure, equal to 0.528 for air, A is the area of the restrictor, which in this case is the area of the hole of the distributor. The coefficient of discharge, c_d , has a handful of ways of being calculated, however in this case, the approach proposed by M. Neves and colleagues[6] is used, as seen in **Equation 2.2**.

$$c_d = \begin{cases} 0.9093 - 0.0751 \frac{p_c}{p_s} & \text{if } \frac{p_c}{p_s} > b_c \\ 0.88 & \text{if } \frac{p_c}{p_s} \leq b_c \end{cases} \quad (2.2)$$

The discharge coefficient will be a function of the supply pressure p_s and the atmospheric pressure $p_c = 101325 Pa$. However, for this case, a constant discharge coefficient of $c_d = 0.9$ was taken. The comparison between the theoretical and the experimental values of the mass flow rate for the measured pressures can be seen in **Figure 2.10**. In this figure, it is clear to see how the experimental flow rate is systematically smaller than the theoretical one. This could be due to constant losses in the system that would lead to this discrepancy. It is also worth noting the fact that the experimental values do not go beneath 1.8 bar. This was due to the fact that at lower supply pressures the shaft would not spin and thus all the measurements were carried out starting from this point.

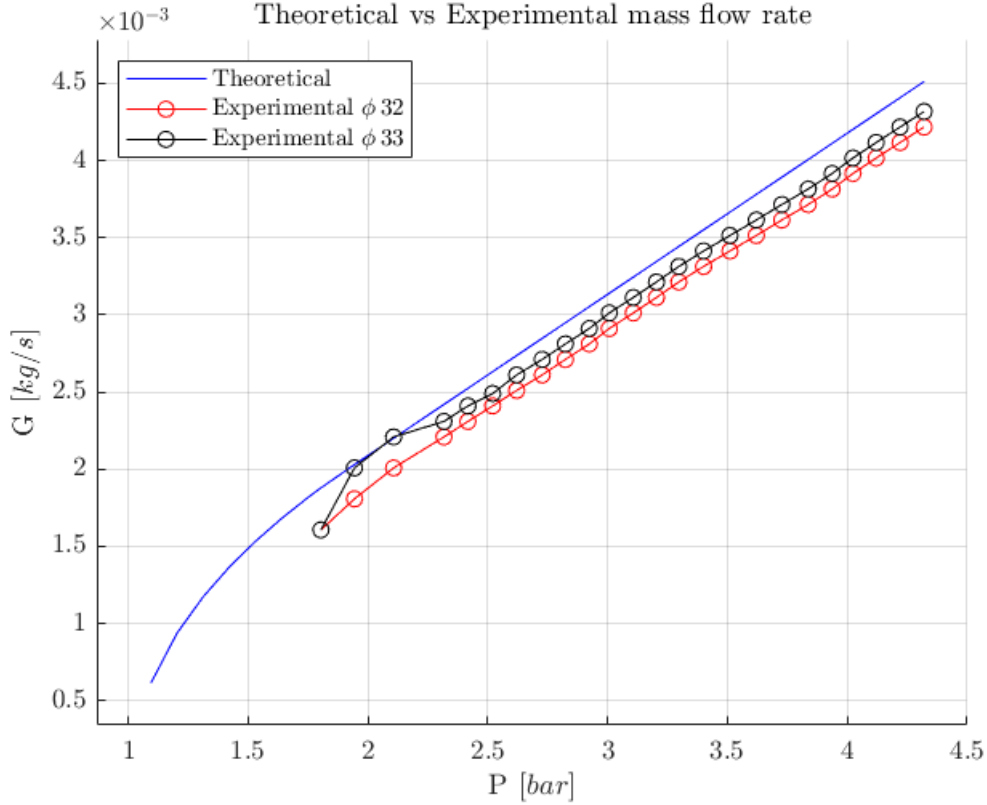


Figure 2.10: Comparison between the experimental and theoretical values of the mass flow rate

2.2 Thrust bearing test bench

For the thrust bearings, a pre-assembled test bench was utilized, which included instrumentation to measure the angular velocity of the shaft, the turbine inlet pressure, the force exerted on the thrust bearing, and the air gap between the thrust bearing and the shaft. **Figure 2.11** shows a diagram of the system. In order to function properly, pressurized air must be fed into the aerostatic journal bearings, marked as $P_{S_{jb}}$ in the forementioned figure. This configuration allows the shaft to rotate without restriction. Subsequently, to achieve high rotational speeds, the nozzle supplies pressurized air (P_{S_n} in the diagram) to the turbine. Depending on the mass flow rate delivered to the turbine, rotational speeds of up to $110krpm$ can be attained. The speed of the turbine is then measured with an optical speed sensor. The rotation of the turbine, combined with the applied load F , induces the formation of an air gap h between the shaft and the bearing. With the use of capacitive sensors, both the radial displacement and mainly the air gap were measured. Moreover, the applied force on the shaft was measured with a load cell for maximum accuracy and precision. This load cell was placed between the thrust bearing and the sensor side cap. The use of a load cell was a modification to the original test bench. This decision was taken due to the unreliability of the previous force measuring method. This previous method measured the pressure of the air load at the inlet of the load side nozzle and then via a relation between the surface area of the shaft at that end, the load force was calculated. This resulted in major discrepancies between the

calculated force value and the real value which was measured with the load cell.

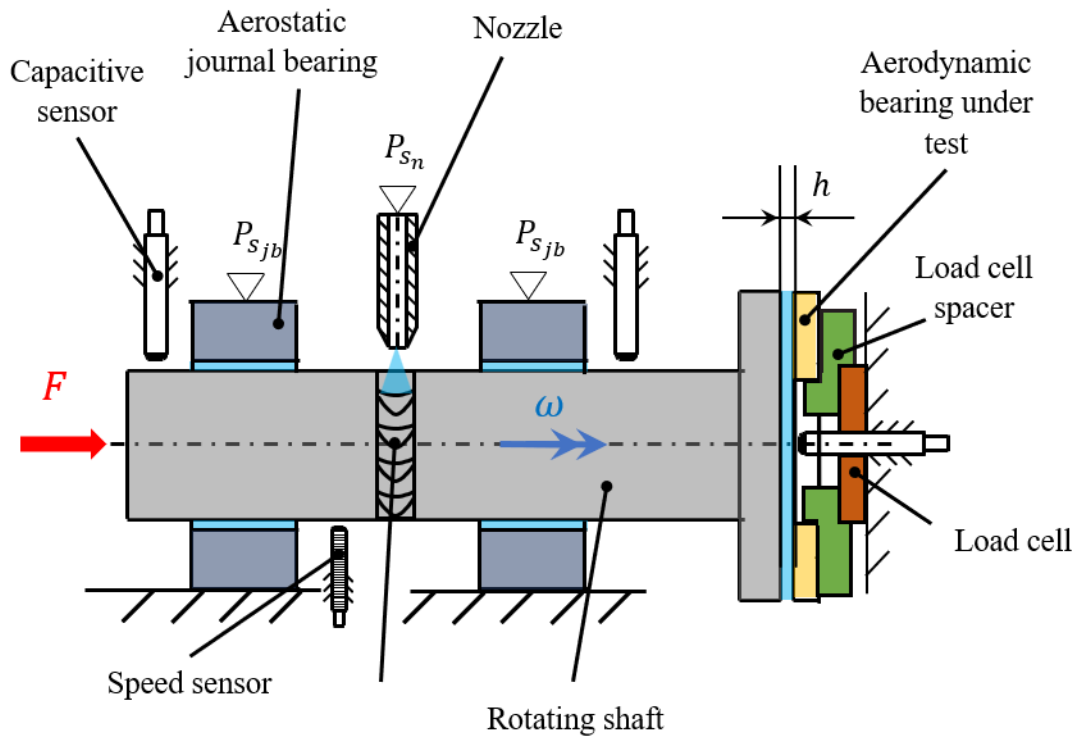


Figure 2.11: Test bench system diagram

A CAD model of the test bench and a photograph of the actual system are provided for reference in **Figures 2.12-2.13**. Moreover, the cutaway CAD view seen in **Figure 2.14** shows the components of the test bench which are listed in accordance with this figure in **Table 2.2**.

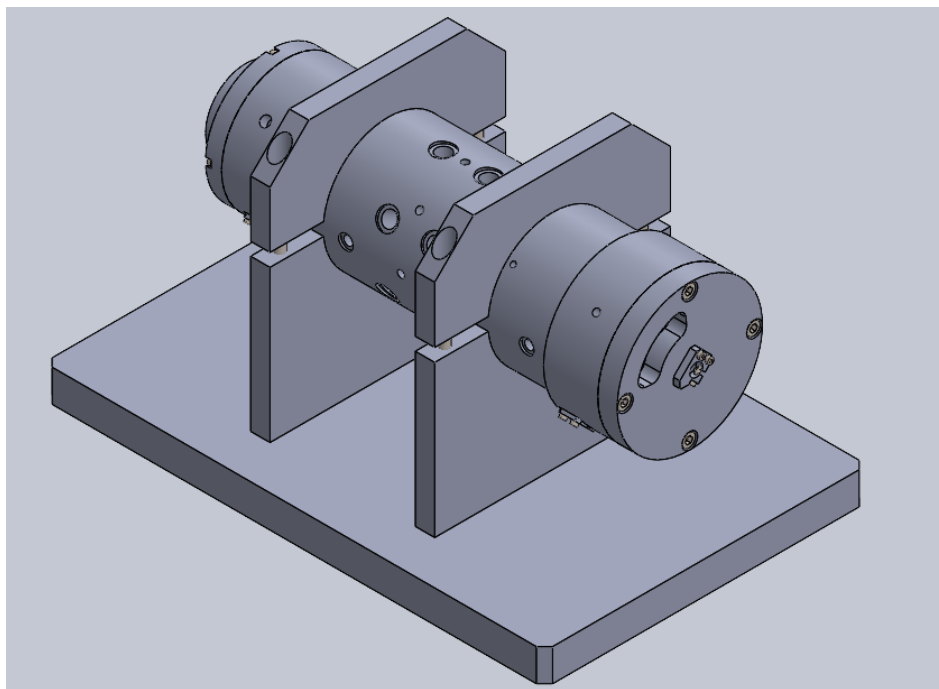


Figure 2.12: Test bench CAD Isometric view



Figure 2.13: Picture of the test bench and the experimental setup

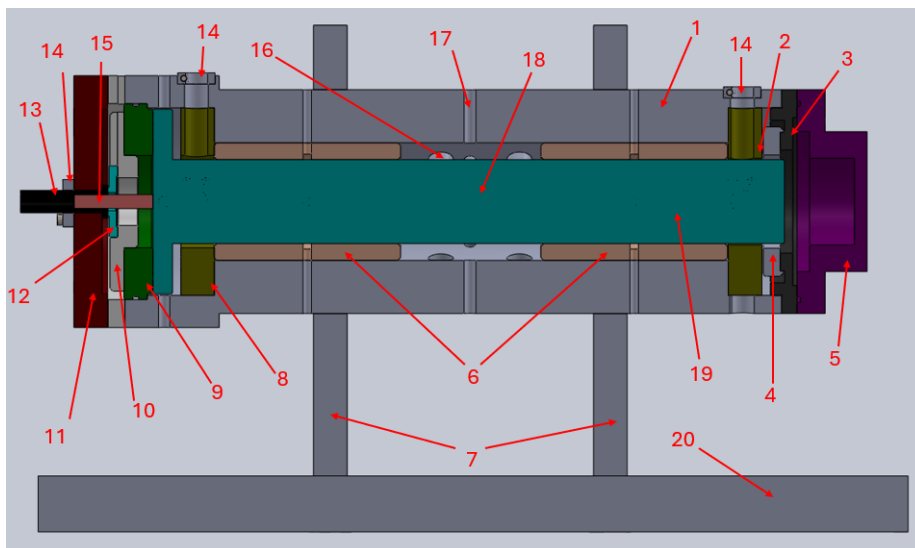


Figure 2.14: Cutaway view of the Test Bench

Item number	Part Name
1	Main Housing
2	Load side shaft cap
3	Support for AEGIS ring
4	AEGIS <i>SGR28.1_3MFH</i> ring
5	Load side housing cap
6	Aerostatic Journal Bearing
7	Housing supports/clamps
8	Bearing side shaft cap
9	Aerodynamic Thrust Bearing
10	Load cell spacer
11	Bearing side Housing cap with sensor housing
12	Load Cell
13	Sensor adaptor
14	Sensor clamp
15	Capacitive Sensor
16	Silencer
17	Air distributor in main housing
18	Shaft turbines
19	Shaft
20	Steel Base

Table 2.2: Test bench part list

2.3 Sensors and repeatability

The system was instrumented with sensors to measure key performance parameters. An ROSM - Modulated Remote Optical LED Sensor (PN:6180-902) was employed to measure the angular velocity of the shaft, detecting changes in reflectivity using reflective tape attached to the shaft's surface. This sensor has a threaded housing, which made it such that it could be attached directly into the main housing for measurements. **Figures 2.15-2.16** show the sensor by itself and the way it was introduced to the test bench respectively.



Figure 2.15: Sensor picture taken from Monarch's web page

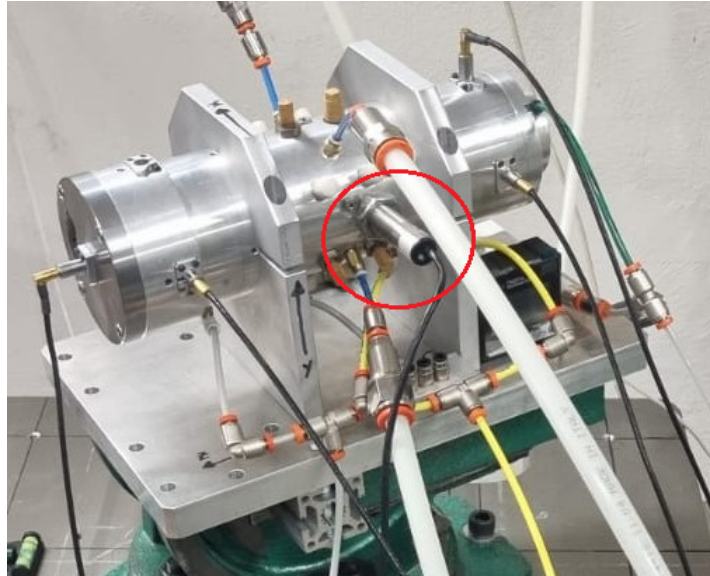


Figure 2.16: Speed sensor's position in the test bench

Among the various sensors utilized, capacitive displacement sensors played a crucial role in determining the air gap between the rotating and stationary components. These sensors operate based on variations in capacitance caused by changes in distance between the probe and the measured surface, providing highly precise, non-contact measurements.

To measure the air gap between the thrust bearing and the shaft, a Lion Precision capacitive sensor, model C5-0.8-2.0, was used. This sensor, which features a 5 mm diameter, was connected to a Lion Precision CPL190 driver. The sensor has a measurement range of up to 100 μm , allowing for precise monitoring of the thin gas film separating the thrust bearing from the shaft. Images taken from Lion Precision's data sheets are provided in **Figures 2.17-2.19**.



Figure 2.17: Lion Precision CPL190 isometric view



Figure 2.18: Lion Precision CPL190 front view



Figure 2.19: Lion Precision C5-0.8-2.0 probe picture

For the aerostatic journal bearings, the air gap was measured using a Micro-Epsilon capacitive sensor, model CSE05. This sensor was paired with the capaNCDT 6200 controller, also from Micro-Epsilon. Unlike the sensor used for the thrust bearing, the CSE05 model offers a larger measurement range of 500 μm , making it suitable for capturing variations in the air gap within the journal bearing system. A picture of the controller present in the lab is shown in **Figure 2.20**.



Figure 2.20: Micro Epsilon capaNCdT 6200 controller picture

These capacitive sensors provided high-resolution measurements critical for analyzing the behavior of the bearings under different operating conditions. Their non-contact nature ensured minimal interference with the system while maintaining precise and repeatable data acquisition.

Air supply pressure was recorded using a digital barometer, and the mass flow rate of the air was measured with a digital volumetric flow rate meter. This combination of sensors ensured accurate and reliable data acquisition.

2.4 Measuring procedure

A specific procedure was implemented to address a systematic error that affected the air gap measurements. This error manifested as a relative displacement in every recorded air gap value, meaning that each measurement included a virtual air gap that did not exist physically. This occurred because, at the start of the test, the shaft was initially in contact with the bearing, yet the sensor still registered a nonzero distance. To account for this error, the following correction method was applied.

First, the journal bearings were supplied with pressurized air at 6 bar to lift the shaft, allowing it to rotate freely. At this moment, the initial air gap $h_{initial}$ was defined as the distance measured by the sensor. This value served as the reference point for all subsequent measurements. Next, the turbine mounted on the shaft was provided with air, while the test bench was maintained at its minimum inclination, as seen in **Figure 2.21**, to prevent any contact between the shaft and the housing. Once the

shaft reached a rotational speed of at least 15 krpm, the inclination was adjusted to achieve the desired load condition. An example of the maximum inclination used can be seen in **Figure 2.22**. With the system in this state, the test was performed by measuring the air gap at different rotational speeds, progressively increasing ω until the maximum speed was reached.

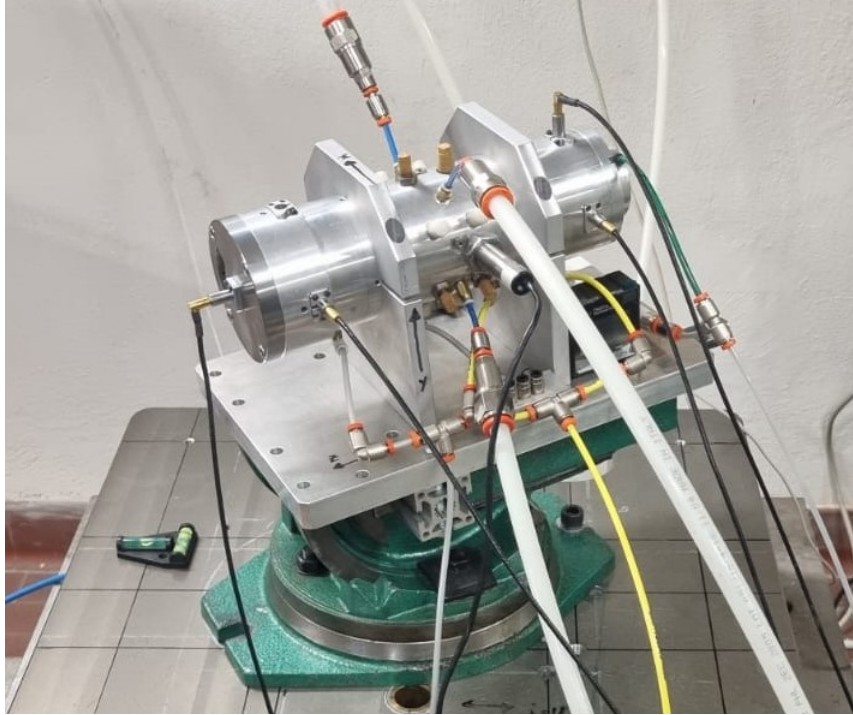


Figure 2.21: Picture of the test bench at minimum inclination



Figure 2.22: Picture of the test bench at a tested inclination (maximum in this case)

After completing the test, the test bench was returned to its initial conditions, and the air gap h was re-evaluated and compared to the initial air gap $h_{initial}$. If these values were equal, the results were considered valid, and a new test could proceed. Once all tests were completed, the final air gap h_{final} was measured and subtracted from all recorded values to ensure coherent and corrected results.

It is important to note that h_{final} was often negative, indicating a slight displacement of the bearing throughout the tests. This issue persisted and must be addressed in future iterations of the test bench. The observed displacement is likely due to the bearing being supported only by a housing cap, with its fit relying on machining tolerances. While this micro-displacement is negligible in standard applications, it becomes significant when measuring air gaps in the micrometer range, leading to measurable deviations in the results. Future improvements to the test bench should focus on ensuring a more rigid and stable support structure to eliminate this source of error.

2.5 Roundmeter bearing surface scan

Since the bearings used in the experimental part of this paper were already manufactured, but without data on their actual geometry, a surface scan was performed to ensure accurate simulations and a proper approximation of the system. The surface scan of each thrust bearing was performed using the Roundtest R100 from SM Instruments. The use of this device was essential because the grooves in the thrust bearings were of the order of $10\ \mu m$, and the Roundtest R100 offered a precision of $0.1\ \mu m$. As this machine is typically used to test high precision manufacturing tolerances, it was capable of capturing groove patterns with exceptional accuracy. The bearings were measured using the *Flatness* measurement option, which takes measurements of concentric circles across the surface of the desired part from a given starting radius to a final given radius. A photograph of the setup is provided in **Figure 2.23** and the graphical results as seen directly from the roundmeter software in **Figure 2.24**.

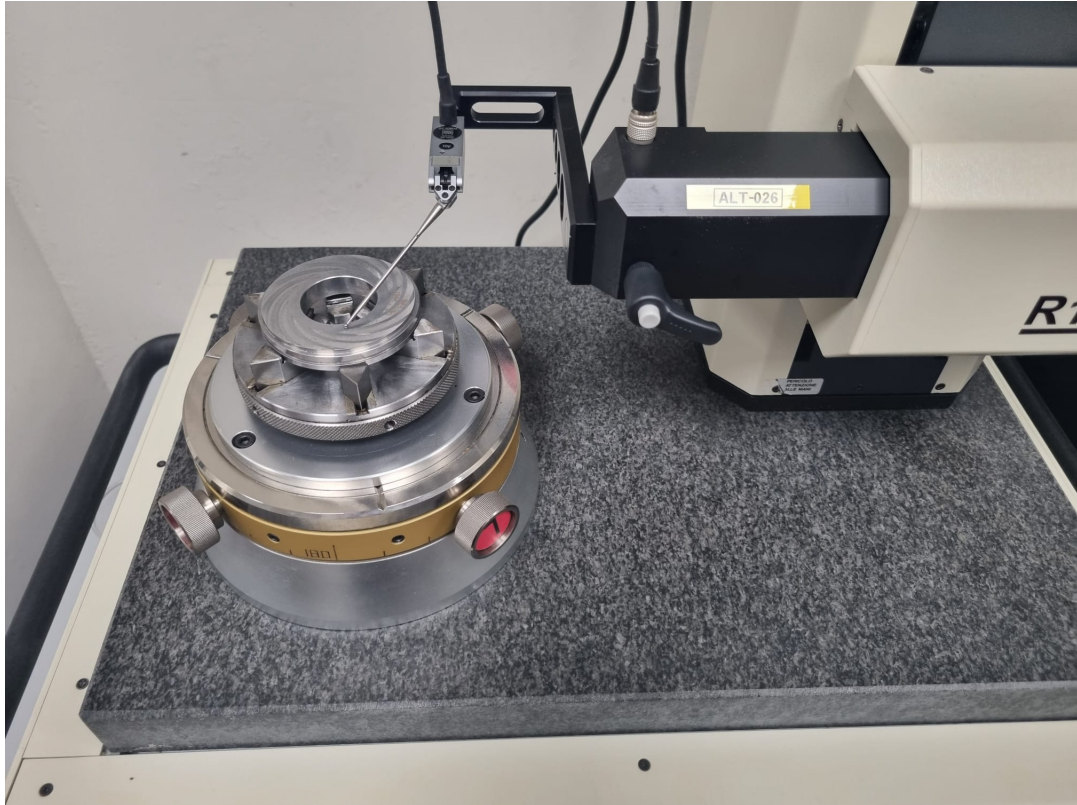


Figure 2.23: Setup for the surface scan

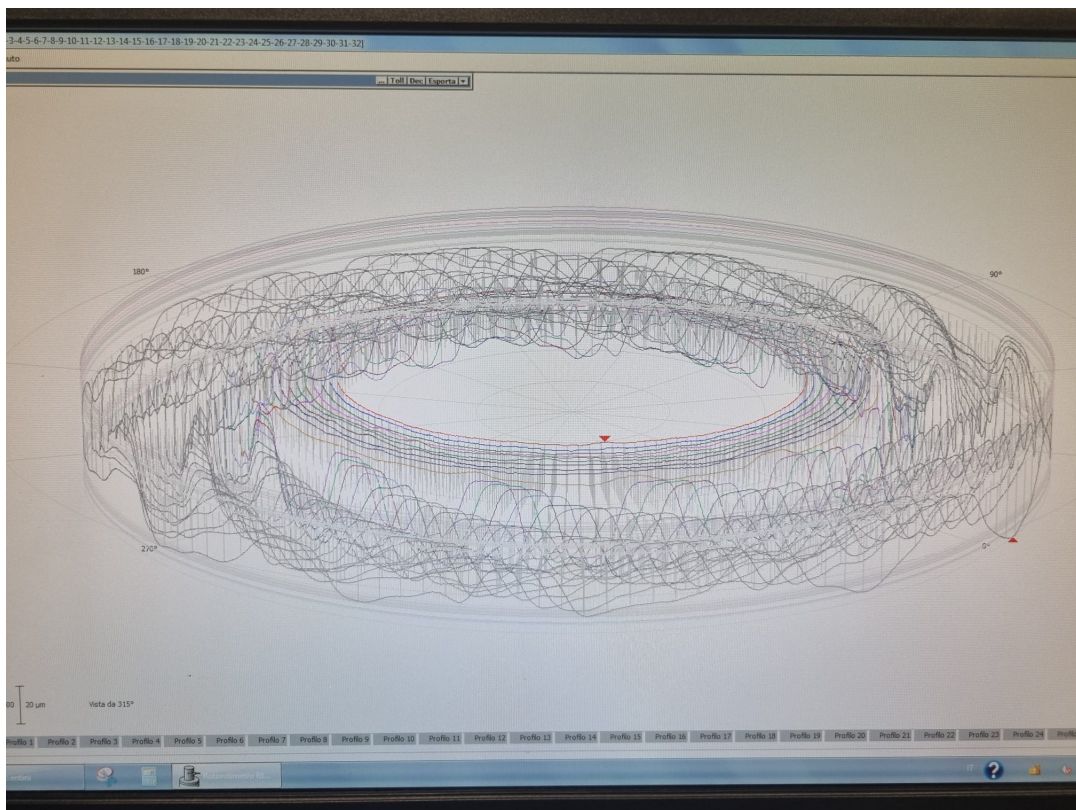


Figure 2.24: Graphical results in the roundmeter software

2.5.1 Scan procedure

To assess the flatness and surface characteristics of the aerodynamic thrust bearings, a surface scan was conducted using a roundmeter. This process involved a precise measurement procedure to ensure that any surface deviations or imperfections were accurately captured.

The procedure began with the careful positioning of the bearing within the clamping system of the roundmeter. The bearing was placed as flatly as possible within the clamp to minimize initial misalignment. Once positioned, the bearing was firmly secured using the roundmeter's built-in clamping system to prevent movement during measurement.

Following the securing process, a leveling procedure was performed to eliminate any tilt in the mounted piece. The measuring tool was positioned on the surface of the bearing, and the machine conducted a full 360-degree rotation to detect any tilt deviations. Although these deviations are often imperceptible to the naked eye, they typically exist within a range of less than 0.1 mm. Based on the data collected, the software provided real-time feedback, instructing the user on which dials to adjust to achieve a level contact between the bearing and the clamp. Once the leveling adjustments were completed, the system was ready to proceed with the measurement process.

The selected measurement procedure for this analysis was the "flatness" scan, which evaluates the surface profile by measuring at increasingly larger concentric circles. Before initiating the scan, several parameters had to be configured, including the starting radius, the finishing radius, and the number of measurement circles. The roundmeter allows for a minimum of one and a maximum of 32 circles for measurement.

For this specific measurement, the starting radius was set at 15.5 mm, while the finishing radius was set at 31.5 mm, with an interval of 0.5 mm between each concentric measurement circle. Once these parameters were confirmed, the measurement procedure began. The machine performed a full 360-degree rotation at each radius, collecting data at intervals of 0.1 degrees. This high-resolution scanning process resulted in 3600 data points per complete turn. After completing the first measurement circle, the machine advanced to the next radius and repeated the process until the final radius was reached.

Upon completion of the scanning procedure, the results were displayed on the software interface as shown in **Figure 2.24**. The collected data could be analyzed directly on the system or exported as a text file for further processing and detailed analysis. This precise surface scanning procedure ensured that the aerodynamic thrust bearings' flatness and overall surface characteristics were thoroughly evaluated, providing essential data for further research and optimization.

Chapter 3

Numerical Model

3.1 Reynolds Equation

To accurately model the system, several simplifications were made based on its characteristics and inherent approximations based on Reynolds equations. One key simplification arose from the disparity in characteristic dimensions within the system. Specifically, the air gap h between the thrust bearing and the shaft was on the order of micrometers (μm), whereas the radius r of the bearing was on the order of millimeters (mm). This significant difference in scale allowed the problem to be simplified by assuming that the pressure profile primarily depended on the radial distance r and the angular position of the control volume relative to the origin.

$$\begin{aligned} R \gg h \\ u, v \gg w \end{aligned} \Rightarrow \begin{aligned} p = p(r, \theta) \\ \mu = const \end{aligned} \quad (3.1)$$

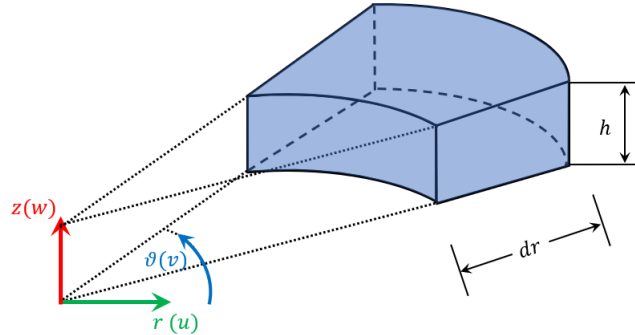


Figure 3.1: Diagram of a partial Control Volume of the system

After the initial simplifications were established, the next step involved deriving the equilibrium equations for the stress tensor within the control volume. This was achieved by grouping the components of the stress tensor by their respective relation to the direction of the pressure field with respect to the control volume, resulting in a separate equilibrium equation for each direction. Specifically, expressions were obtained for equilibrium with the pressure field in the radial direction $r(u)$, the angular direction $\theta(v)$, and the vertical direction $z(w)$. The resulting equilibrium equations are as follows.

$$\begin{aligned}
\frac{\partial \tau_{rz}}{\partial r} + \frac{\partial \tau_{rz}}{\partial \theta} = 0 & \quad \frac{\partial}{\partial r} \left(\mu \frac{\partial u}{\partial z} \right) + \frac{1}{r} \frac{\partial}{\partial \theta} \left(\mu \frac{\partial v}{\partial z} \right) = 0 & \quad \frac{\partial^2 u}{\partial r \partial z} + \frac{1}{r} \frac{\partial^2 v}{\partial \theta \partial z} \\
\frac{\partial \tau_{z\theta}}{\partial z} r d\theta dr dz = \frac{\partial p}{\partial \theta} d\theta dr dz & \quad \frac{\partial}{\partial z} \left(\mu \frac{\partial v}{\partial z} \right) = \frac{1}{r} \frac{\partial p}{\partial \theta} & \quad \mu \frac{\partial^2 v}{\partial z^2} = \frac{1}{r} \frac{\partial p}{\partial \theta} \\
\frac{\partial \tau_{zr}}{\partial z} = \frac{\partial p}{\partial r} & \quad \frac{\partial}{\partial z} \left(\mu \frac{\partial u}{\partial z} \right) = \frac{\partial p}{\partial r} & \quad \mu \frac{\partial^2 u}{\partial z^2} = \frac{\partial p}{\partial r}
\end{aligned} \tag{3.2}$$

For a more detailed and comprehensive explanation of the derivation of these equations, refer to the annex, where each case is thoroughly described and clearly presented.

Using the equations provided in 3.2, expressions for the velocity profiles u and v were obtained by integrating with respect to z . The results of these integrations are shown in **Equations 3.3** and **3.4**.

$$\mu \frac{\partial^2 u}{\partial z^2} = \frac{\partial p}{\partial r} \rightarrow \frac{\partial u}{\partial z} = \frac{z}{\mu} \frac{\partial p}{\partial r} + C_1 \rightarrow u = \frac{z^2}{2\mu} \frac{\partial p}{\partial r} + C_1 z + C_2 \tag{3.3}$$

$$\mu \frac{\partial^2 v}{\partial z^2} = \frac{1}{r} \frac{\partial p}{\partial \theta} \rightarrow \frac{\partial v}{\partial z} = \frac{z}{\mu r} \frac{\partial p}{\partial \theta} + C_3 \rightarrow v = \frac{z^2}{2r\mu} \frac{\partial p}{\partial \theta} + C_3 z + C_4 \tag{3.4}$$

Following the derivation of these expressions, boundary conditions were applied to define the integration constants. Specifically, the no-slip conditions for the fluid relative to the system's walls, the shaft, and the thrust bearing were used.

Boundary conditions u :

$$\begin{aligned}
u(0) = 0 & \Rightarrow C_2 = 0 \\
u(h) = 0 & \Rightarrow C_1 = -\frac{h}{2\mu} \frac{\partial p}{\partial r}
\end{aligned} \tag{3.5}$$

Boundary conditions v :

$$\begin{aligned}
v(0) = 0 & \Rightarrow C_4 = 0 \\
v(h) = 0 & \Rightarrow C_3 = \frac{\omega r}{h} - \frac{h}{2r\mu} \frac{\partial p}{\partial \theta}
\end{aligned} \tag{3.6}$$

With these integration constants defined, the velocity profiles as well as both the volumetric and mass flow rate expressions can be obtained.

Velocity Profiles

Volumetric flow rate per unit depth

$$\begin{aligned}
u &= \frac{z^2}{2\mu} \frac{\partial p}{\partial r} - \frac{zh}{2\mu} \frac{\partial p}{\partial r} & q_r &= \int_0^h u dz = -\frac{h^3}{12\mu} \frac{\partial p}{\partial r} \\
v &= \frac{z^2}{2r\mu} \frac{\partial p}{\partial \theta} - \frac{zh}{2r\mu} \frac{\partial p}{\partial \theta} + \omega r \frac{z}{h} & q_\theta &= \int_0^h v dz = \frac{\omega r h}{2} - \frac{h^3}{12\mu r} \frac{\partial p}{\partial \theta}
\end{aligned}$$

Mass flow rate per unit depth

$$\begin{aligned}
g_r &= \int_0^h \rho u dz = -\frac{\rho h^3}{12\mu} \frac{\partial p}{\partial r} \\
g_\theta &= \int_0^h \rho v dz = \frac{\rho \omega r h}{2} - \frac{\rho h^3}{12\mu r} \frac{\partial p}{\partial \theta}
\end{aligned}$$

With these last expressions for the mass flow rate per unit depth, it was possible to apply the mass conservation of the control volume. In order to achieve this, the sum of all mass flow through every face of the control volume (excluding the once related to the depth due to dimensions of this quantity with respect to the others)

should equal the total mass flow rate of the control volume. Which can be written using the nomenclature used in **Figure 3.2**.

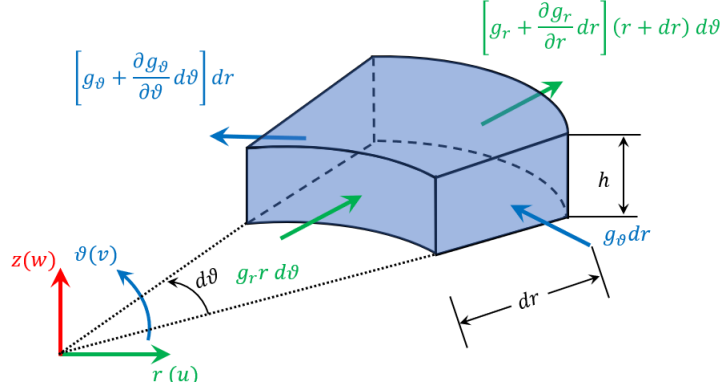


Figure 3.2: Representation of the mass flow through the control volume

$$\begin{aligned}
 & - \left(g_\theta + \frac{\partial g_\theta}{\partial \theta} d\theta \right) dr - \left(g_r + \frac{\partial g_r}{\partial r} dr \right) (r + dr) d\theta + g_r d\theta + g_\theta dr = \\
 & = \left(h \frac{\partial \rho}{\partial t} + \rho \frac{\partial h}{\partial t} \right) r d\theta dr = \frac{dm}{dt}
 \end{aligned} \tag{3.7}$$

Equation 3.7 can be further simplified into the following formulation.

$$\begin{aligned}
 & - \frac{\partial}{\partial \theta} \left(\frac{\rho \omega r h}{2} - \frac{\rho h^3}{12 \mu r} \frac{\partial p}{\partial \theta} \right) d\theta dr - \frac{\partial}{\partial r} \left(- \frac{\rho h^3}{12 \mu} \frac{\partial p}{\partial r} \right) (r + dr) d\theta dr = \\
 & = \left(h \frac{\partial \rho}{\partial t} + \rho \frac{\partial h}{\partial t} \right) r d\theta dr
 \end{aligned} \tag{3.8}$$

What is more, by assuming the air in the system to be a perfect gas, it is possible to write **Equation 3.8** as follows.

$$\begin{aligned}
 & \frac{\partial}{\partial \theta} \left(\frac{p h^3}{12 \mu R_g T r} \frac{\partial p}{\partial \theta} - \frac{p \omega r h}{2 R_g T} \right) d\theta dr + \frac{\partial}{\partial r} \left(p \frac{h^3}{12 \mu R_g T} \frac{\partial p}{\partial r} \right) (r + dr) d\theta dr = \\
 & = \left(\frac{h}{R_g T} \frac{\partial p}{\partial t} + \frac{p}{R_g T} \frac{\partial h}{\partial t} \right) r d\theta dr
 \end{aligned} \tag{3.9}$$

Equation 3.9 represents the final expression defining the mass equilibrium for the control volume of the system. This equation will be utilized in the following section to apply the Finite Difference Method for numerically approximating and accurately modeling the system.

3.2 Finite Differences Method

3.2.1 Discretization of equations

The discretized equations for the solution were formulated by approximating the derivatives in the radial and angular directions using finite difference approximations. Temporal evolution was managed through the Forward Euler scheme, enabling a stepwise progression toward the solution. This process was achieved by discretizing the mass flow rates used in the derivation of **Equation 3.9**. **Figure**

3.3 illustrates a generic element within the mesh, providing a visual representation of how the equation was discretized.

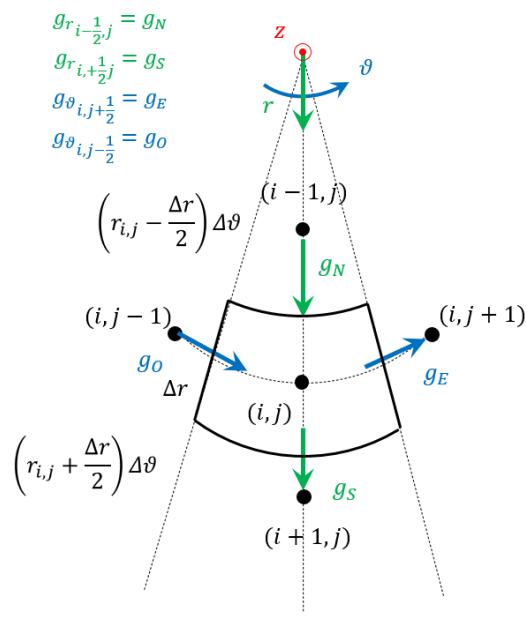


Figure 3.3: Diagram of an element in the FDM mesh

The specific equations used in this numerical approach are provided below:

$$g_N r_{i-\frac{1}{2},j} \Delta\vartheta - g_S r_{i+\frac{1}{2},j} \Delta\vartheta + (g_O - g_E) \Delta r = \left(\frac{h_{i,j}^t}{R_g T} \frac{p_{i,j}^{t+1} - p_{i,j}^t}{\Delta t} + \frac{p_{i,j}^t}{R_g T} h_{i,j}^t \right) r_{i,j} \Delta\vartheta \Delta r \quad (3.10)$$

$$G_N = - \frac{p_{i-\frac{1}{2},j} h_{i-\frac{1}{2},j}^3}{12 \mu R_g T} \left. \frac{\partial p}{\partial r} \right|_{i-\frac{1}{2},j} \Delta\vartheta = - \frac{(p_{i-1,j} h_{i-1,j}^3 r_{i-1,j} + p_{i,j} h_{i,j}^3 r_{i,j}) (p_{i,j} - p_{i-1,j})}{24 \mu R_g T \Delta r}$$

$$G_S = - \frac{p_{i+\frac{1}{2},j} h_{i+\frac{1}{2},j}^3}{12 \mu R_g T} \left. \frac{\partial p}{\partial r} \right|_{i+\frac{1}{2},j} \Delta\vartheta = - \frac{(p_{i,j} h_{i,j}^3 r_{i,j} + p_{i+1,j} h_{i+1,j}^3 r_{i+1,j}) (p_{i+1,j} - p_{i,j})}{24 \mu R_g T \Delta r}$$

$$\begin{aligned} g_O &= - \frac{p_{i,j-\frac{1}{2}} h_{i,j-\frac{1}{2}}^3}{12 \mu R_g T r_{i,j-\frac{1}{2}}} \left. \frac{\partial p}{\partial \vartheta} \right|_{i,j-\frac{1}{2}} + \frac{p_{i,j-\frac{1}{2}} r_{i,j-\frac{1}{2}} h_{i,j-\frac{1}{2}} \omega}{2 R_g T} \\ &= - \frac{(p_{i,j-1} h_{i,j-1}^3 + p_{i,j} h_{i,j}^3) (p_{i,j} - p_{i,j-1})}{12 \mu R_g T (r_{i,j-1} + r_{i,j}) \Delta\vartheta} + \omega \frac{(p_{i,j-1} h_{i,j-1} r_{i,j-1} + p_{i,j} h_{i,j} r_{i,j})}{4 R_g T} \end{aligned}$$

$$\begin{aligned} g_E &= - \frac{p_{i,j+\frac{1}{2}} h_{i,j+\frac{1}{2}}^3}{12 \mu R_g T r_{i,j+\frac{1}{2}}} \left. \frac{\partial p}{\partial \vartheta} \right|_{i,j+\frac{1}{2}} + \frac{p_{i,j+\frac{1}{2}} r_{i,j+\frac{1}{2}} h_{i,j+\frac{1}{2}} \omega}{2 R_g T} \\ &= - \frac{(p_{i,j} h_{i,j}^3 + p_{i,j+1} h_{i,j+1}^3) (p_{i,j+1} - p_{i,j})}{12 \mu R_g T (r_{i,j} + r_{i,j+1}) \Delta\vartheta} + \omega \frac{(p_{i,j} h_{i,j} r_{i,j} + p_{i,j+1} h_{i,j+1} r_{i,j+1})}{4 R_g T} \end{aligned}$$

These equations, applied at each grid point in the $N \times M$ mesh, enabled the numerical approximation of the system's behavior over time, as the only unknown in **Equation 3.10** is the pressure of node i, j at time $t + 1$.

3.2.2 Meshing

The bearings were modelled by means of a two dimensional mesh, as the system could be represented by a 2D model in polar coordinates. The mesh consisted of an $M \times N$ grid, where M represented the number of elements along the radial coordinate (r), and N represented the number of elements along the angular coordinate (θ). This is shown in the representative diagram in **Figure 3.5**. In this diagram, the index i varies radially, while the index j varies angularly.

Since the thrust bearings possess a circular geometry, structuring the mesh in polar coordinates ensures that the discretization of the domain aligns with the natural curvature of the problem. This approach improves both computational efficiency and accuracy by reducing numerical errors associated with approximating a circular system in a Cartesian framework.

Each finite volume in the grid is centered around a central node, which serves as the reference point for numerical computations. These central nodes are connected to their nearest neighbors, ensuring a structured arrangement that facilitates the finite difference method (FDM) implementation. The central node approach is particularly significant, as it dictates how the governing equations will be discretized. The finite volume method ensures that mass conservation is enforced across each control volume, making the meshing process crucial for accurately capturing the behavior of the fluid film within the bearing gap.

By structuring the mesh in polar coordinates and aligning it with the physics of the problem, the numerical model effectively approximates the pressure distribution and flow characteristics within the bearing gap. This structured meshing technique enables a more accurate and stable simulation of the aerodynamic thrust bearing performance.

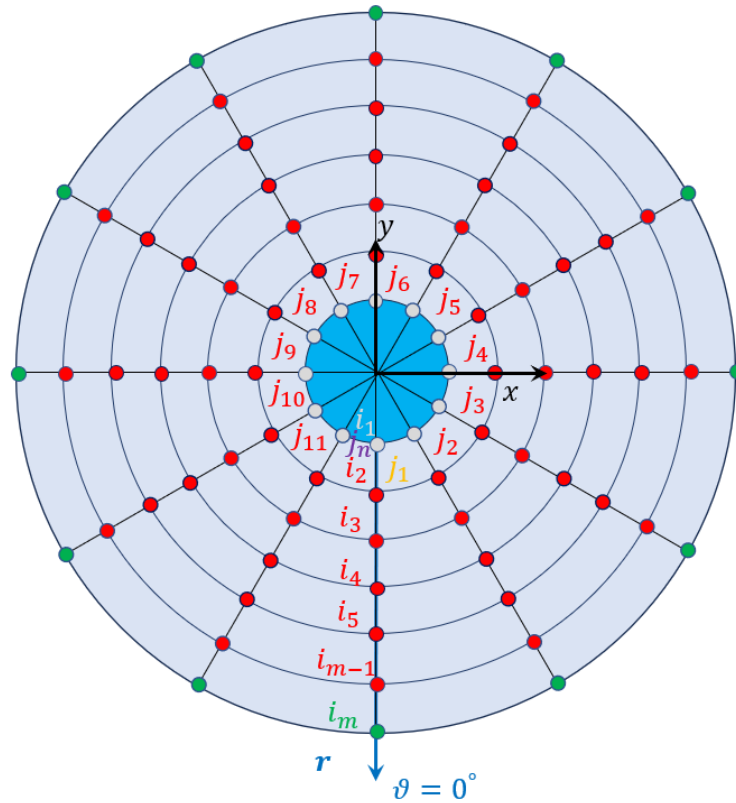


Figure 3.4: Diagram of the circular mesh

This mesh can be represented in the 2D plane in which one axis is the angular variable and the other axis is the radial variable. This representation is the same as the matrix form of the system, and thus its importance. Moreover, since the geometry of the model is a circular one, a periodic boundary condition needs to be implemented for the validity of the model. This was achieved by setting Neumann boundary conditions in for the borders of the control volume that where an axis of symmetry is located. All of these is shown in **Figure 3.5**.

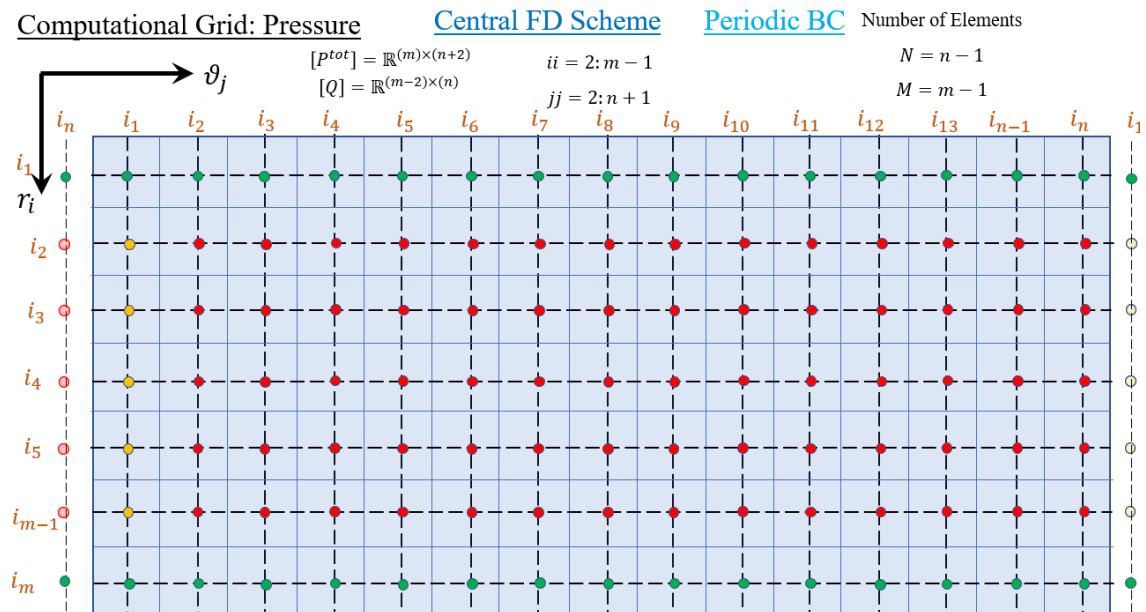


Figure 3.5: Diagram of the 2D plane mesh

3.2.3 Symmetry

A key factor for the numerical modeling of this problem, and any problem for that matter, is the presence of symmetry in the model. In the case of this project, symmetry is present in both of the studied bearings. For the spiral bearing, there are multiple symmetries, but most notably a small sector of just 30° can be simulated in order to obtain the full behavior of the system. This is due to the fact that there are 12 spirals which means that a 12^{th} of the total geometry will give a 12^{th} of the loading capacity of the bearing for a given air gap and rotational speed. An example of this symmetry is shown in **Figure 3.6**, which shows visually the concept of the symmetry present in the system in a meshed domain.

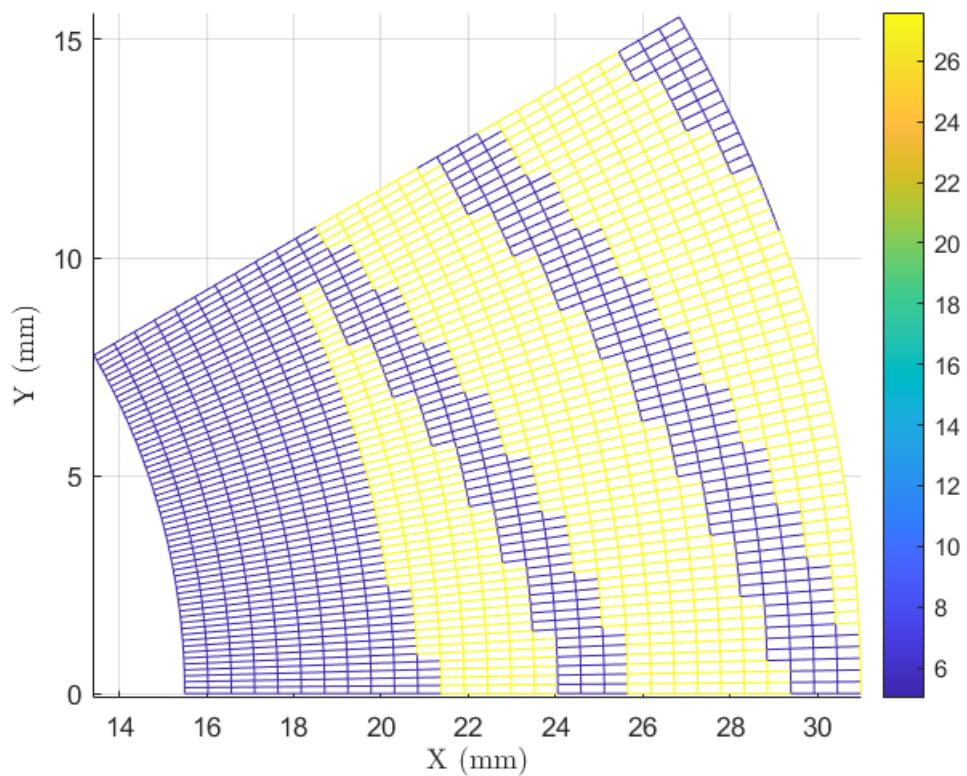


Figure 3.6: Example of a 30° sector mesh

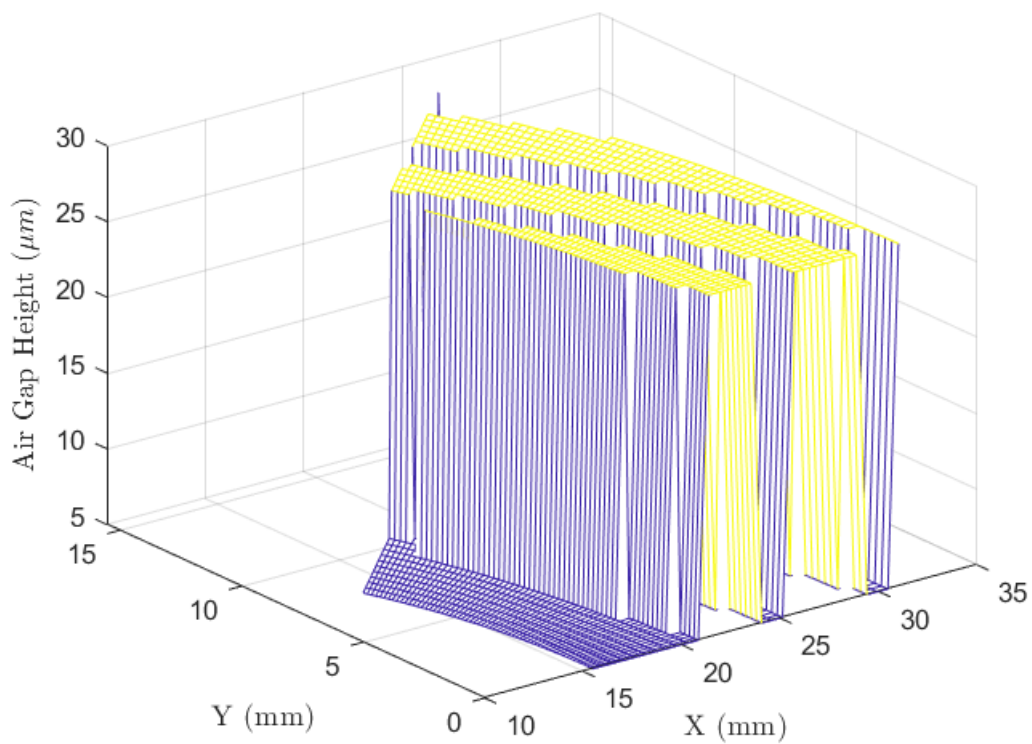


Figure 3.7: 3D view of the spiral bearing mesh example

As for the tapered bearing, the symmetry is much more straight forward, since the bearing itself is a circular pattern of repeating flat pads followed by a slanted plane into a slot. This pattern is repeated 6 times in the studied bearing, which means that the domain to be meshed was just one of these pads, which accounted for one sixth of the load capacity. **Figure 3.8** shows the mesh of the pad in question.

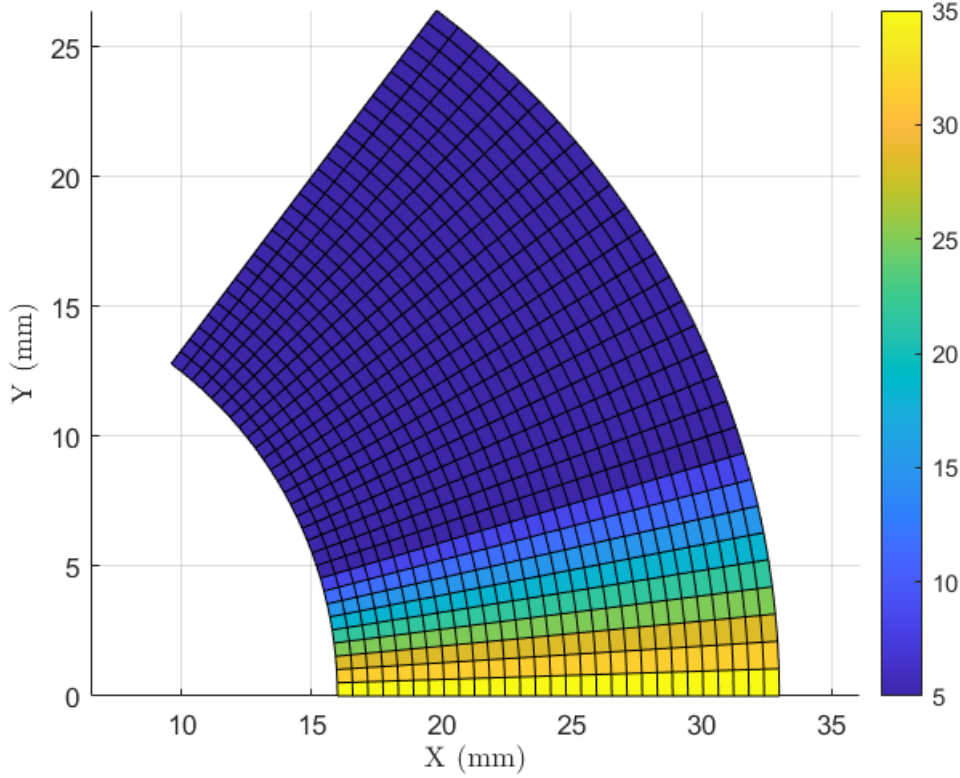


Figure 3.8: Example of the mesh of 1 pad ($\frac{1}{6}$ of the surface)

These meshes were utilized to solve **Equation 3.9** using the Finite Difference Method in conjunction with the Forward Euler Method. It is important to note that the Forward Euler Method has the significant drawback of requiring a minimal time step for the system to converge to a result. However, due to the highly coupled nature of the equations, employing an implicit method that does not rely on small time steps was discarded because of the substantial complexities involved in its implementation. As a result, this approach led to considerable simulation times.

3.2.4 Spiral bearing mesh generation

The mesh creation for the spiral thrust bearing needed a specific code in order to be generated. The grooves present in the bearing are mathematically described in polar coordinates by **Equation 1.1** as introduced in **Chapter 1**.

$$r = r_2 \cdot e^{\theta \tan(\beta)}$$

This equation defines a single logarithmic spiral curve, meaning that the groove regions of the bearing are confined between two such curves at any given angular

position. To implement this pattern in MATLAB, a logical array was created to distinguish between grooved and non-grooved regions. This array, of dimensions equal to the mesh size ($M \times N$), was structured such that positions corresponding to groove locations were assigned a value of 1, while the non-grooved (land) regions were assigned a value of 0. **Figure 3.9** shows the initialization of the function *getGrooves* implemented, where the main outbound logical array *isGroove* is created with the same size as the mesh.

```

1 function [ang,ang1,isGroove] = GetGrooves(r1,r2,x_spiral,y_spiral,n_grooves,beta,delta_beta,R,Theta)
2 % FUNCTION TO IDENTIFY THE LOCATIONS OF LOGARITHMIC SPIRAL GROOVES IN A 2D CIRCULAR MESH
3 %
4 % Inputs:
5 % GEOMETRY DEFINED ACCORDING TO MUIJDERMAN NOTATION:
6 % r1 [m] - Innermost radius of the bearing
7 % r2 [m] - Outer radius of the bearing
8 % x_spiral [adim] - Ratio of groove widths (a1/a2)
9 % y_spiral [adim] - Normalized groove position, defined as (r2-rb)/(r2-r1)
10 % n_grooves - Number of spiral grooves
11 % beta [°] - Base angle of the logarithmic spiral
12 % delta_beta [°] - Phase shift of the spiral with respect to the 0° reference line
13 % R [m] - Array of radial coordinates (MxN)
14 % Theta [°] - Array of angular coordinates (MxN)
15
16 % Outputs:
17 % ang - Array containing the angular position of the logarithmic spiral groove at different radii
18 % ang1 - Array containing the angular position of the second boundary of the groove
19 % isGroove - Logical array of the same size as the input mesh, where 'true'
20 % (1) indicates a groove region and 'false' (0) indicates a land region
21
22 isGroove = false(size(R)); % Initialize logical array for groove locations
23 Theta = Theta - pi; % Shift the angular domain to be within [-pi, pi] for consistency

```

Figure 3.9: Function "getGrooves" initialization

A scheme was implemented that defines a single groove at a time. The method involved defining the equations for the two boundary lines of a groove, as shown in **Figure 3.10**, by first writing the equation for one logarithmic spiral and then adding a phase delay ($\Delta\theta$ in the diagram) to the angle that defines the second boundary of the groove. The equation describing the logarithmic spiral was reformulated to express it in terms of the angular coordinate θ for a given radial value r , as seen in **Equation 3.11**:

$$\theta = -\tan(\beta) \cdot \ln\left(\frac{r}{r_b}\right) \quad (3.11)$$

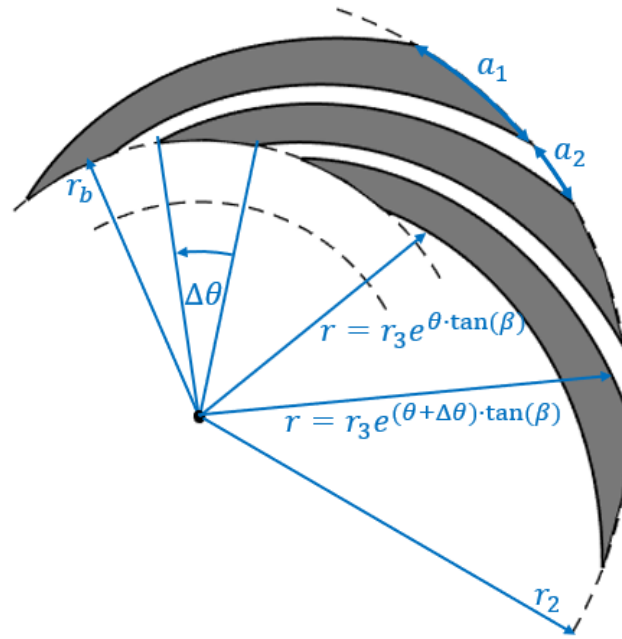


Figure 3.10: Spiral groove curve representation diagram

In the code shown in **Figure 3.11** two variables were created to define these boundaries, *angle* and *angle1*. The former is defined following **Equation 3.11** which means that it will have the angular coordinates of the logarithmic curve for the given radial values (*r* in the code). The latter is the same curve but displaced by $\Delta\theta$, which can be calculated as $\Delta\theta = \frac{a_1}{r_2}$, with a_1 being the sector in *m* of the base of the groove and r_2 being the external radius.

```

25 %% LOGARITHMIC GROOVE GEOMETRY
26 passo = 2.*pi.*r2./n_grooves; % Circumferential pitch (spacing) of grooves
27 delta_theta = passo./r2; % Angular separation between grooves
28 a2 = passo./(1+x_spiral); % Groove width (a2) based on given ratio
29 a1 = passo-a2; % Complementary land width (a1)
30 b = y_spiral.*(r2-r1); % Radial position of the base of the groove
31 rb = r2-b; % Base radius of the grooves (starting point of the spiral)
32 beta = beta/180*pi; % Convert beta from degrees to radians
33
34 % Generate logarithmic spiral curves for the groove boundaries
35 r = linspace(rb,r2,100); % Radial discretization for the spiral
36 angle = -tan(beta).*log(r./r2) - delta_beta; % Logarithmic spiral equation for first boundary
37 angle1 = angle + a1./r2; % Second boundary of the groove (phase-shifted)

```

Figure 3.11: Spiral bearing characteristic parameters and groove boundary equations definition

Once these two boundary-defining equations were established, the next step was to determine which points within the mesh lay inside the groove. This was achieved by comparing the angular coordinate θ of each point at a given radius r to the two boundary curves. Specifically, for each point in the domain, a check was performed to determine whether its angular value was greater than the lower boundary and smaller than the upper boundary at its corresponding radius. If this condition was met, the local logical array for the groove being processed at that moment was set

to true, indicating that the point was inside the groove. This procedure is shown in **Figures 3.12-3.13**.

```

47 %% GROOVE IDENTIFICATION
48 % Initialize arrays to store angular values for each groove
49 ang = zeros(length(angle),n_grooves);
50 ang1 = zeros(length(angle1),n_grooves);
51
52 % Adjust boundary angles for each groove iteration
53 angle_logic = angle_logic - delta_theta;
54 angle1_logic = angle1_logic - delta_theta;
55
56 for i = 1:n_grooves
57 % Define angular positions for the current groove
58 ang(:,i) = angle + (i-1) * delta_theta;
59 ang1(:,i) = angle1 + (i-1) * delta_theta;
60 angle_logic = angle_logic + delta_theta;
61 angle1_logic = angle1_logic + delta_theta;
62
63 % Ensure angular values remain within the [-pi, pi] domain
64 angle_logic(angle_logic>pi) = angle_logic(angle_logic>pi) - 2*pi;
65 angle1_logic(angle1_logic>pi) = angle1_logic(angle1_logic>pi) - 2*pi;
66
67 % Identify cases where the groove transitions across the -pi to pi boundary
68 pos_log = angle_logic > 0 & angle1_logic < 0;

```

Figure 3.12: Grooved points identification 1st part

```

69 if ~isempty(find(pos_log, 1))
70 % If a groove crosses the angular boundary, handle it separately
71 pos_log = find(pos_log);
72 Theta_log = [false(size(Theta,1),pos-1), ...
73             Theta(:,pos:end) > angle_logic & Theta(:,pos:end) < angle1_logic];
74
75 Theta_log = Theta_log | [false(size(Theta,1),pos+pos_log(1)-2), ...
76                        Theta(:,pos_log) > angle_logic(pos_log) | Theta(:,pos_log) < angle1_logic(pos_log), ...
77                        false(size(Theta,1),size(Theta,2)-pos_log(end)-pos+1)];
78
79 else
80 % Standard case where groove does not cross the angular boundary
81 Theta_log = [false(size(Theta,1),pos-1), ...
82             Theta(:,pos:end) > angle_logic & Theta(:,pos:end) < angle1_logic];
83
84 end
85
86 % Update the global logical array, ensuring that only regions inside the groove are marked
87 isGroove = isGroove | Theta_log;
88 isGroove = isGroove & (R >= rb);
89
90 end

```

Figure 3.13: Grooved points identification 2nd part

This procedure was repeated for all 12 grooves. Each time a groove was analyzed, the global logical array, named *isGroove*, was updated to ensure that all grooves were correctly mapped. Once all grooves had been processed, this logical array was used to apply the groove depth to the computational mesh, ensuring an accurate representation of the spiral thrust bearing’s geometry. This approach allowed for an efficient application of the groove depth pattern onto the circular mesh of the bearing. Refer to the **Annex** for all the pictures of the utilized code.

Once the logical array was established, the air gap distribution across the mesh could be readily defined. Specifically, for the non-grooved regions (land), the air gap height was set to h , whereas in the grooved regions, the air gap height was set to $h_1 = h_0 + h_2$, in accordance with the notation stated in **Chapter 1**. The logical array facilitated this assignment by evaluating the mesh coordinates against the groove pattern and applying the corresponding depth values.

By utilizing this method, the spiral thrust bearing geometry was successfully embedded within the computational model, ensuring an accurate representation of the groove structure. This structured meshing approach was essential for correctly capturing the aerodynamic effects induced by the logarithmic spiral grooves, thereby enabling a more reliable numerical analysis of the bearing's performance.

Chapter 4

Results

4.1 Turbine Measurements

4.1.1 Angular Speed

In the **Figures 4.1-4.3** the relation between the angular speed and the volumetric flow rate for every turbine can be seen. These figures also depict the difference in angular speed between the different distributors. It is clear to see how the use of a smaller distributor has a considerable impact in the angular speed of the shaft. This is due to the fact that a smaller diameter means that the walls of the distributor are closer to the turbine, making the air have less room to escape from feeding the turbine, resulting in higher speeds, and thus higher efficiency as will be seen in the following section. It is also important to note that in **Figures 4.1-4.2** the measured rotational speeds are much lower than the theoretical one. This theoretical speed was calculated using the data from the distributor, as seen in the following equation.

$$\begin{aligned}u_{th} &= \frac{G_{th}}{\rho_s A} \quad \& \quad \frac{P_a}{\rho_a^\gamma} = \frac{P_s}{\rho_s^\gamma} \\ \Rightarrow u_{th} &= \frac{G_{th}}{\rho_a A} \left(\frac{P_a}{P_s} \right)^{1/\gamma} \\ \Rightarrow \omega_{th} &= \frac{u_{th}}{r_m}\end{aligned}\tag{4.1}$$

Where u_{th} , G_{th} and ω_{th} are the theoretical runner velocity, mass flow rate through the distributor feed hole, and rotational speed respectively. Subindex s for the pressure and the density imply supply (before the feed hole) and a is for ambient. The theoretical rotational speed is calculated at **maximum theoretical efficiency** for the given mass flow rate G . The theoretical mass flow rate was calculated with a discharge coefficient of $c_d = 0.9$, which means that no other loss of efficiency is taken into account for the calculation of ω_{th} . This thus means that theoretical efficiencies will not be shown in **Figures 4.5-4.6** since η_h would be of a constant 100%.

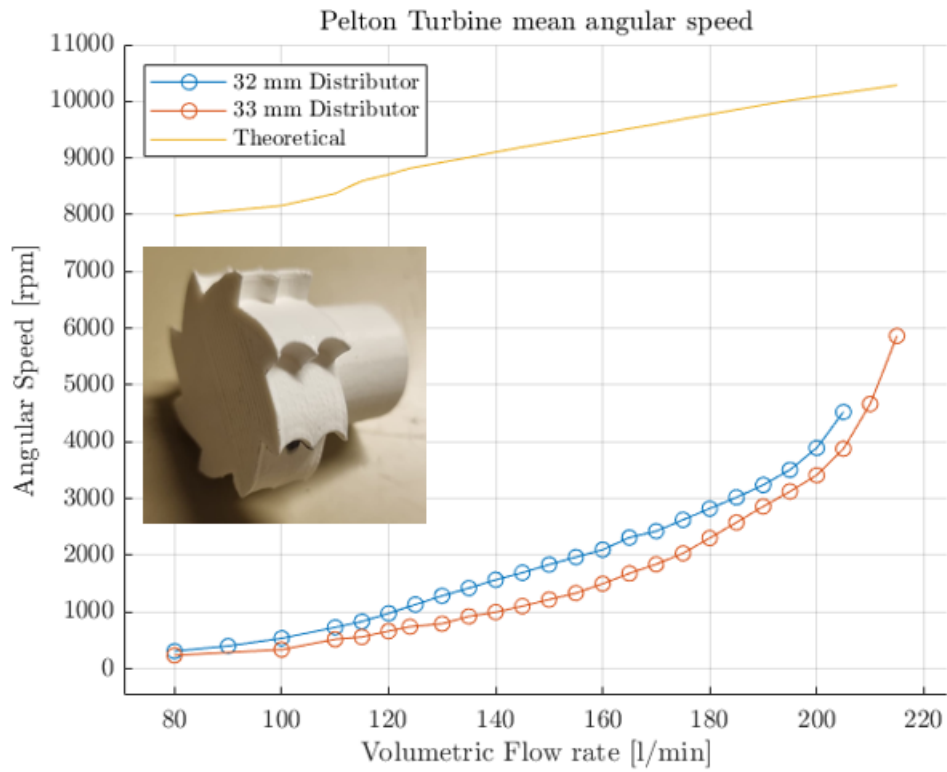


Figure 4.1: Pelton turbine Angular speed vs Experimental Volumetric Flow rate

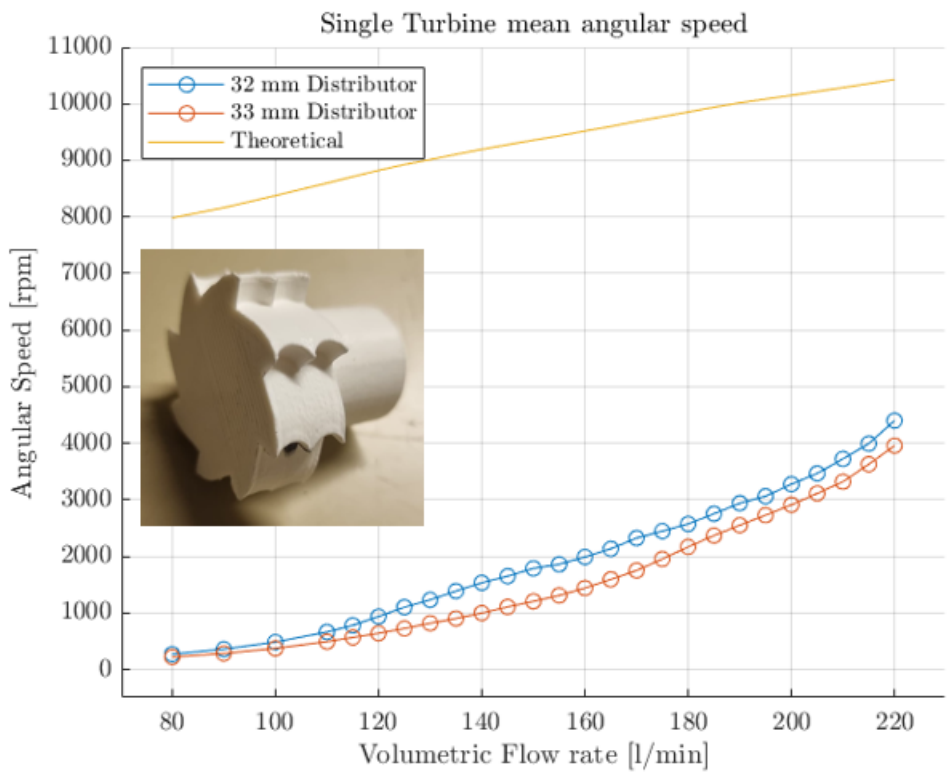


Figure 4.2: Single turbine Angular speed vs Experimental Volumetric Flow rate

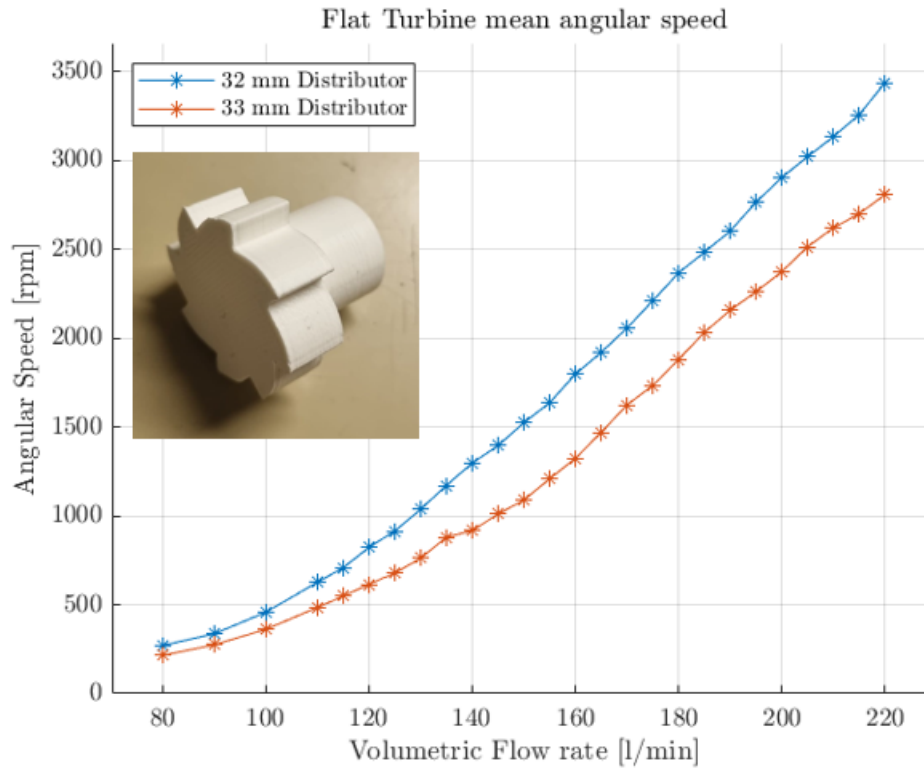


Figure 4.3: Flat turbine Angular speed vs Experimental Volumetric Flow rate

4.1.2 Velocity Triangles

The velocity triangles for a Pelton turbine are sketched in **Figure 4.4**. These were used to calculate the Hydraulic Efficiency η_h of the turbine.

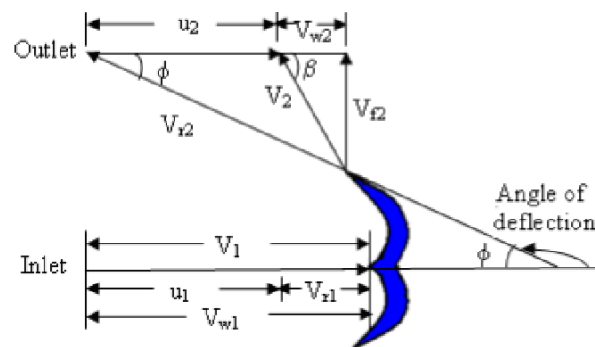


Figure 4.4: Velocity triangles of a generic Pelton turbine

Since the dimensions of the turbine are known, and the angular speed was measured during the experiment, the vane speed can be easily calculated by $u = \omega \cdot r_{mean}$. Moreover, the absolute velocity of the inlet jet can also be easily calculated as shown in **Equation 4.2**.

$$V_1 = G \cdot A \quad (4.2)$$

With these two values and the deflection angle of the turbine, it is possible to calculate the hydraulic efficiency of the system with **Equation 4.3**. These deflection

angles are $\phi_{pelton} = 30.68^\circ$ and $\phi_{single} = 60^\circ$

$$\eta_h = \frac{2(V_1 - u)(1 + \cos(\phi))u}{V_1^2} \quad (4.3)$$

The values for the hydraulic efficiency of the turbine can be seen in **Figures 4.5-4.6**. As was the case for the angular speed, the use of a distributor with a smaller diameter results in overall higher efficiency. What is more, it is clear to see how with the same volumetric flow rate, the hydraulic efficiency of the Pelton turbine is considerable higher than the single paddle design.

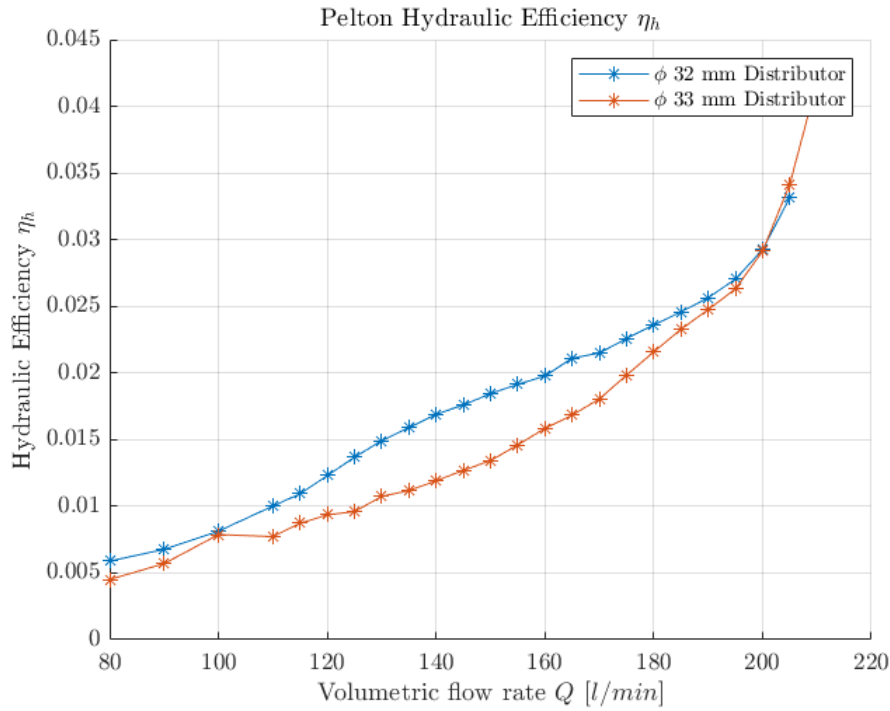


Figure 4.5: Pelton turbine Hydraulic efficiency

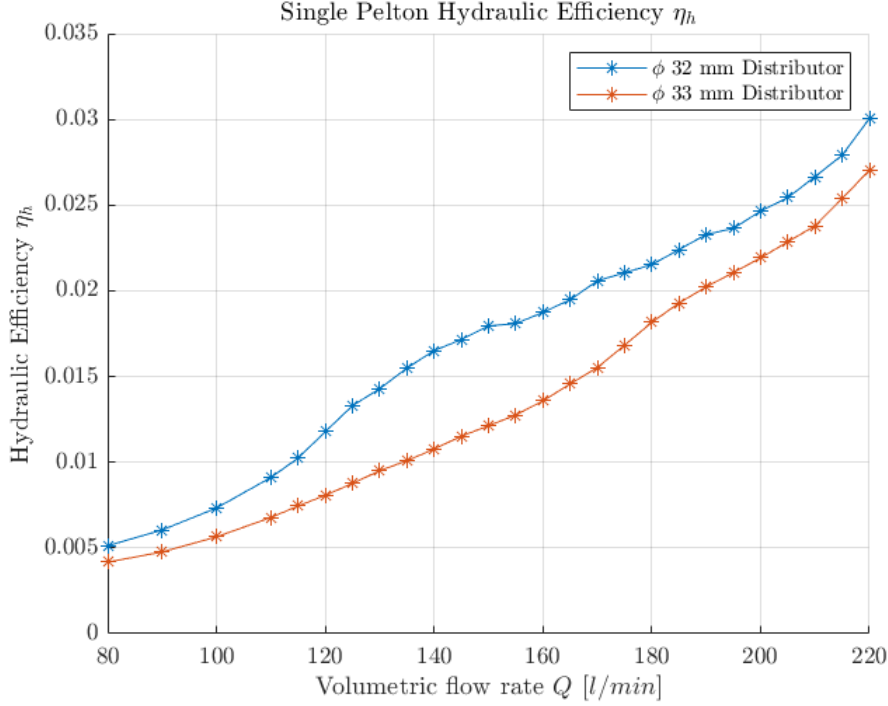


Figure 4.6: Single turbine Hydraulic efficiency

4.1.3 Optimization

In order to get the highest hydraulic efficiency possible, **Equation 4.3** can be differentiated with respect to u to find the maximum efficiency point.

$$\frac{\partial}{\partial u}(\eta_h) = 0$$

$$\frac{\partial}{\partial u} \left(\frac{2(V_1 - u)(1 - \cos(\phi))u}{V_1^2} \right) = 0$$

$$\frac{(1 + \cos(\phi))}{V_1^2} \frac{\partial}{\partial u} [2(V_1 - u)u] = 0$$

$$\frac{\partial}{\partial u} [2V_1u - 2u^2] = 0$$

$$2V_1 - 4u = 0$$

$$u = \frac{V_1}{2}$$

This means that when $u = \frac{V_1}{2}$, the hydraulic efficiency will be maximum, and thus:

$$\eta_{h,max} = \frac{2(V_1 - \frac{V_1}{2})(1 + \cos(\phi))(\frac{V_1}{2})}{V_1^2} \quad (4.4)$$

$$\eta_{h,max} = \frac{1 + \cos(\phi)}{2}$$

Equation 4.4 shows how the maximum efficiency of the turbine will be determined by only a geometrical parameter, namely the angle of deflection ϕ . With this fact it is clear to see how a lower angle will give the turbine a higher hydraulic efficiency, and more specifically the maximum theoretical hydraulic efficiency is reached when

$\phi = 0$. Moreover, another method of discovering the highest efficiency point can be used to check this result. For this, the original hydraulic efficiency equation, **Equation 4.3** can be differentiated with respect to ϕ in order to get the highest efficiency value.

$$\begin{aligned}\frac{\partial}{\partial \phi}(\eta_h) &= 0 \\ \frac{\partial}{\partial \phi} \left(\frac{2(V_1-u)(1-\cos(\phi))u}{V_1^2} \right) &= 0 \\ \frac{\partial}{\partial \phi} \left(\frac{2u((V_1-u)+\cos(\phi)(V_1-u))}{V_1^2} \right) &= 0 \\ \frac{\partial}{\partial \phi} \left(\frac{2u \cos(\phi)(V_1-u)}{V_1^2} \right) &= 0 \\ \frac{-2u \sin(\phi)(V_1-u)}{V_1^2} &= 0 \Leftrightarrow \sin(\phi) = 0\end{aligned}$$

This procedure clearly shows how a lower angle of deflection will result in a higher efficiency, as the maximum point of efficiency is once again located in $\phi = 0$ point.

4.2 Aerodynamic Thrust Bearings

4.2.1 Thrust Bearing Simulations

Two numerical models were developed and implemented in this study: a static model and a dynamic model. Each serves a distinct purpose in analyzing the behavior of aerodynamic thrust bearings under different operating conditions.

The static model is designed to simulate the system under steady-state conditions. A given bearing geometry is provided as input, from which the computational mesh is generated. The model is then configured with an imposed air gap and rotational speed to compute the resulting pressure distribution and load capacity. While both the air gap and rotational speed are key parameters, only one of these can be varied per simulation, ensuring better numerical stability, improved convergence, and reduced computational time.

In contrast, the dynamic model is time-dependent, allowing for the study of the system's transient response until equilibrium is reached. Like the static model, the bearing geometry is predefined, but instead of setting a fixed air gap, the model applies a constant external force and a given rotational speed. The air gap is then iteratively adjusted based on the equilibrium between the external force and the bearing's load capacity.

This model was used for speeds ranging from 5 *krpm* to 100 *krpm*, with increments of 5 *krpm*. The initial conditions included the bearing geometry, the minimum rotational speed, and an initial air gap. The dynamic model is particularly relevant since the test bench operates under similar conditions—applying a constant external force to the shaft, with the air gap adjusting based on the generated bearing force at a given rotational speed.

To ensure computational efficiency, the maximum feasible time step was first determined by running the dynamic model with a randomly selected initial air gap that was physically reasonable. This step was crucial because the time step ranged

from $10^{-7}s$ to $10^{-9}s$, and using a larger time step significantly reduced the overall simulation time needed to reach convergence. The maximum times steps Δt_{max} for each case for the used mesh are informed in **Table 4.1**.

Bearing	Δt_{max} [s]	Mesh size [$M \times N$]
Tapered	7×10^{-8}	30×30
Slider	4×10^{-8}	30×30
Step	2×10^{-8}	30×30
Spiral	5×10^{-9}	30×45

Table 4.1: Maximum time step Δt for the dynamic model for each geometry

Once the optimal time step was identified, the static model was used to simulate the load capacity of the bearing at the minimum rotational speed of 5 krpm , as seen in **Figure 4.7**. This step was essential because it allowed for an efficient initialization of the dynamic model. By using the static model to determine the air gap at which the bearing force equals the external force at the lowest speed, the first step of the dynamic model could be precomputed. This approach reduced simulation time while ensuring that the air gap was consistent with the system's equilibrium conditions.

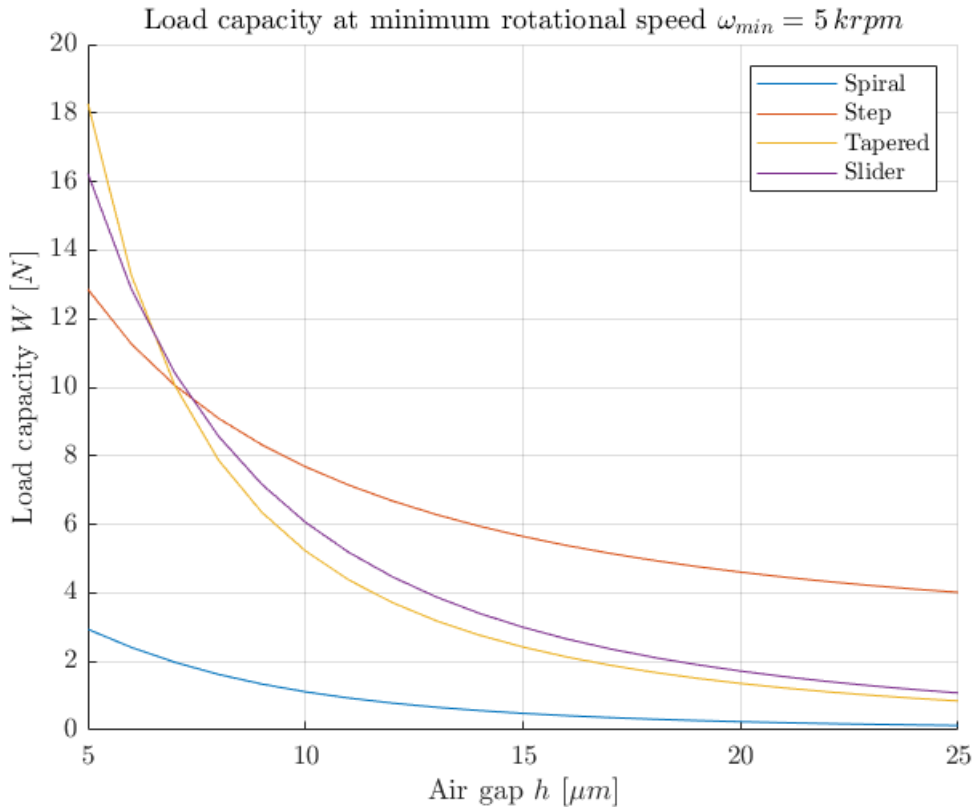


Figure 4.7: Load capacity W as a function of the air gap h at the minimum rotational speed $\omega_{min} = 5 \text{ krpm}$

The geometric parameters for each bearing used for the simulations present in **Figure 4.7** were the following. The slider bearing used $s_h = 30 \mu\text{m}$, the step bearing used $s_h = 30 \mu\text{m}$ and $a = 15^\circ$, the tapered bearing used $s_h = 25 \mu\text{m}$ and $a = 16.5^\circ$

and the spiral bearing used the parameters of the real bearing informed in **Table 4.3**.

4.2.2 Slider

Simulations

A crucial step in each simulation is the verification of the obtained results by inspecting the pressure field at each simulated step. The primary criterion for determining the validity of the results is whether the pressure distribution aligns with the bearing geometry and exhibits no inconsistencies or disruptions.

Disruptions in the pressure field refer to sharp peaks or discontinuities that break the expected smooth distribution. These anomalies are typically caused by numerical instabilities, often resulting from a time step larger than the minimum required for accurate computations. Ensuring the correct time step selection is essential to maintaining the stability and reliability of the simulation.

For each bearing type, a representative pressure field is provided in a corresponding figure to illustrate the expected distribution, serving as a reference for assessing the correctness of the results.

Figure 4.27 presents the pressure field for the slider bearing. It is evident from this figure that the compressive action of the geometry rapidly increases, leading to a pressure peak at the region of maximum compression. Additionally, after reaching this peak, the pressure experiences a noticeable drop. This suggests the potential for an optimized geometry that could further capitalize on this pressure loss, ultimately enhancing the overall performance of the bearing. Moreover, it can be observed that a geometry featuring a gradual ramp leading into a flat surface could sustain the highly compressive region over a significantly longer distance within the bearing surface. This design characteristic defines the Tapered bearing, which represents an evolution of the Slider bearing. The transition from the Slider to the Tapered geometry demonstrates how a refined design enhances performance by extending the compression effect, thereby improving the overall load-carrying capacity of the bearing.

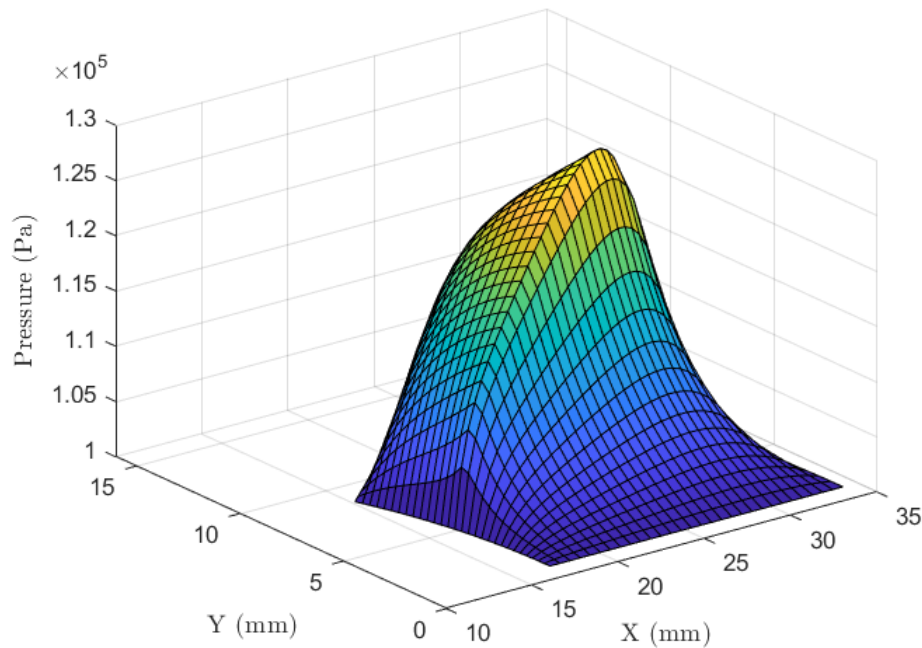


Figure 4.8: Slider bearing simulated pressure field in the static simulation

Optimization

The Slider bearing, being the first type invented and one of the simplest, has only one parameter that needs optimization, the angle of inclination. This angle α is however, minuscule, thus using it directly as a parameter can mean working with angles in the order of 10^{-3} degrees, which does not depict the parameter greatly. The way in which the inclination was decided to be shown is in the maximum groove depth s_h , measured in μm . This value can be seen in the illustration present in **Figure 4.9**.

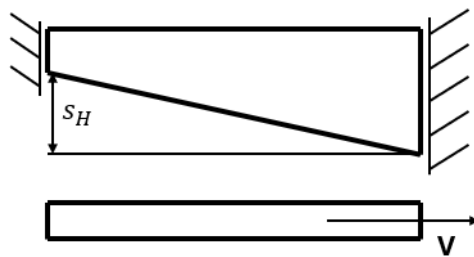


Figure 4.9: Slider bearing s_H depiction

With this said the geometry was analyzed sweeping through the range of values of s_h of $5 \mu m$ to $30 \mu m$. For each value of s_h the mesh was updated, and the corresponding plane going from the selected air gap between the bearing and the shaft $h = 5 \mu m$ to $s_h + h$. Then for each case the bearing load capacity with the previously stated parameters, $\omega = 70 \text{ krpm}$ and a total of 6 pads, was calculated and the results are shown in **Figure 4.10**. It is important to note that the maximum rotational speed that could be reached with the test bench was used to optimize the geometry of

this **and at the other geometries** since this would be the point with the highest power input and where the system would be subjected to the highest load.

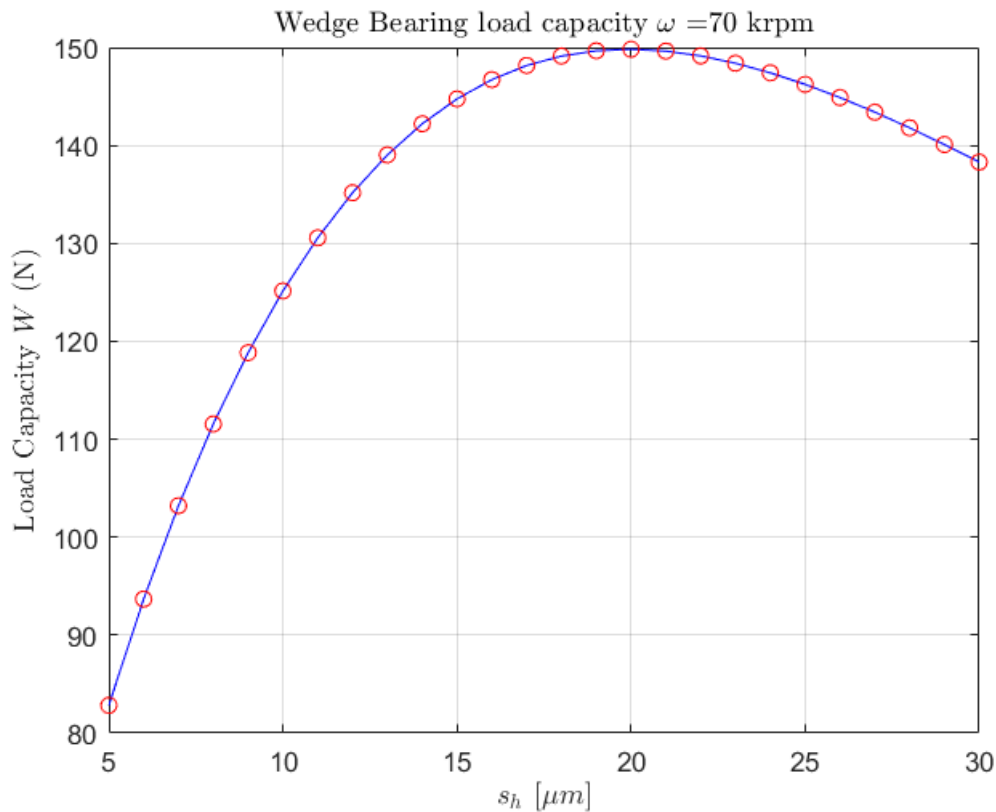


Figure 4.10: Slider bearing, Slider depth vs load capacity

A clear maximum is located at $s_h = 20 \mu m$. The system was then simulated using the static model between the speeds of $\omega = 5$ krpm and $\omega = 70$ krpm with 5 air gap values, these being $h = 10 \mu m$ and $h = 20 \mu m$ with a step of $2 \mu m$. The results are shown in **Figure 4.11**.

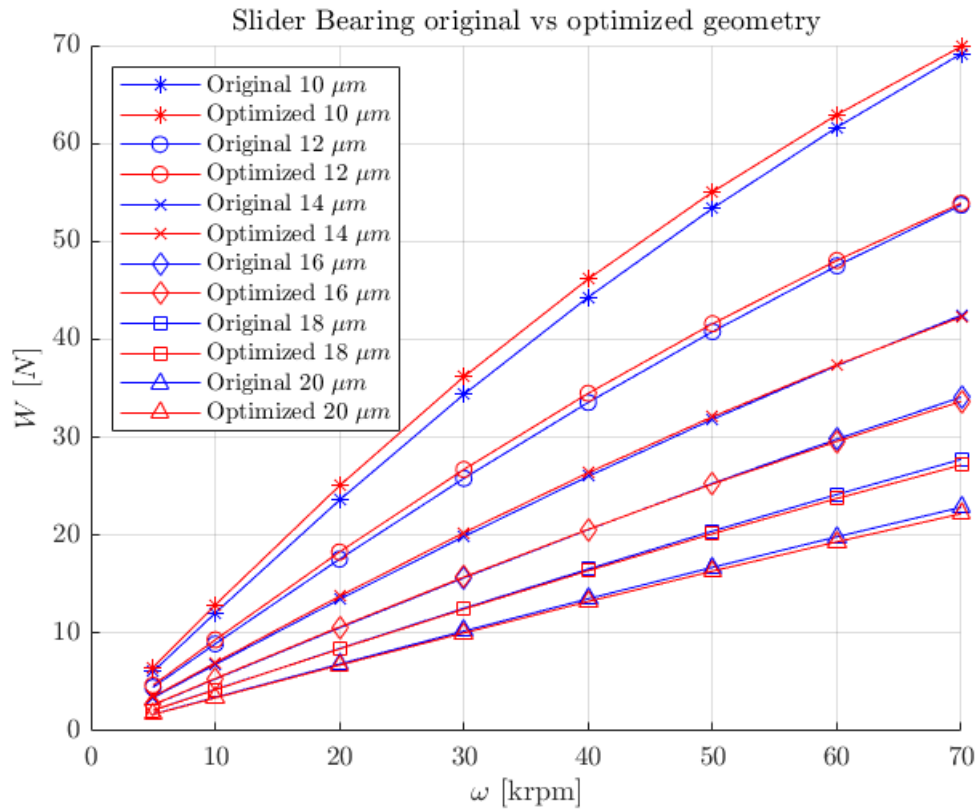


Figure 4.11: Initial generic geometry vs optimized geometry

It is evident that the optimized geometry exhibits improved performance at lower air gap values, while showing a slight reduction in performance at higher air gaps. This can be attributed to the fact that the initial generic geometry already possessed characteristic values similar to those of the optimized design, particularly in terms of maximum groove depth, which was $s_h = 25 \mu\text{m}$ compared to $20 \mu\text{m}$ in the optimized configuration. Furthermore, the decline in performance near and beyond the point of maximum load capacity remains minimal, as observed in Figure 4.11, further emphasizing the similarity in performance between the two geometries.

4.2.3 Step

Simulations

The step bearing presents a pressure field with a rapid increase in pressure as the air reaches the step itself as seen in **Figure 4.12**. After the step a slower decrease in pressure relative to the slider bearing can be observed, suggesting an increase in load capacity due to a greater area with a high pressure.

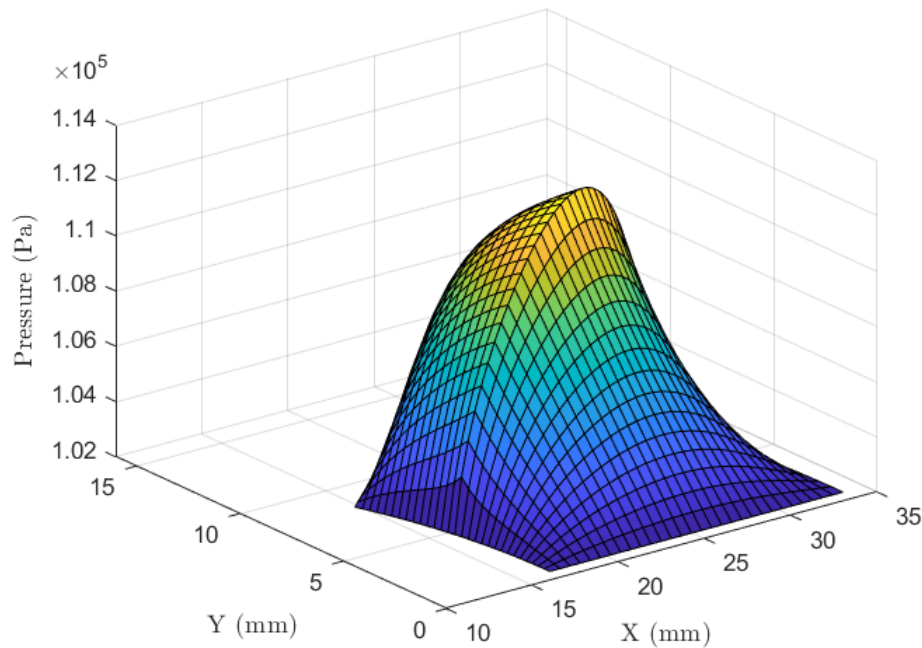


Figure 4.12: Step bearing simulated pressure field in the static simulation

Optimization

The step bearing presents two parameters that can be optimized, other than the number of pads. These parameters are the distance from the groove start to the step x_{step} and the step depth s_h . Since the bearings are of circular geometry, distance x_{step} can also be expressed as an angular sector of the pad a , which would also eliminate the need to select a radius for which to determine the measuring reference. The angular sector was thus the parameter adopted for the optimization of the bearing geometry. **Figures 4.13-4.14** show diagrams that illustrate the parameters present in the bearing and that were optimized.

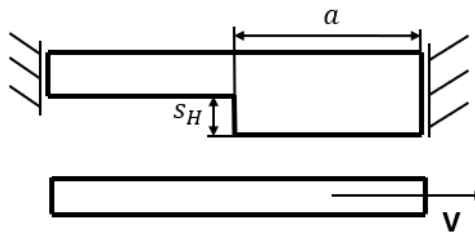


Figure 4.13: Bearing side section depicting s_H and a

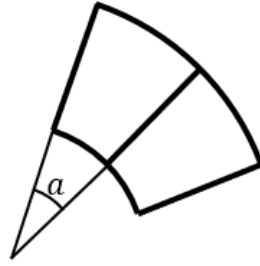


Figure 4.14: Diagram depicting a from the top view

Since there are two parameters to be optimized, a sweep of both was done with the use of a double *for* command and the results are shown in **Figures 4.15-4.16**.

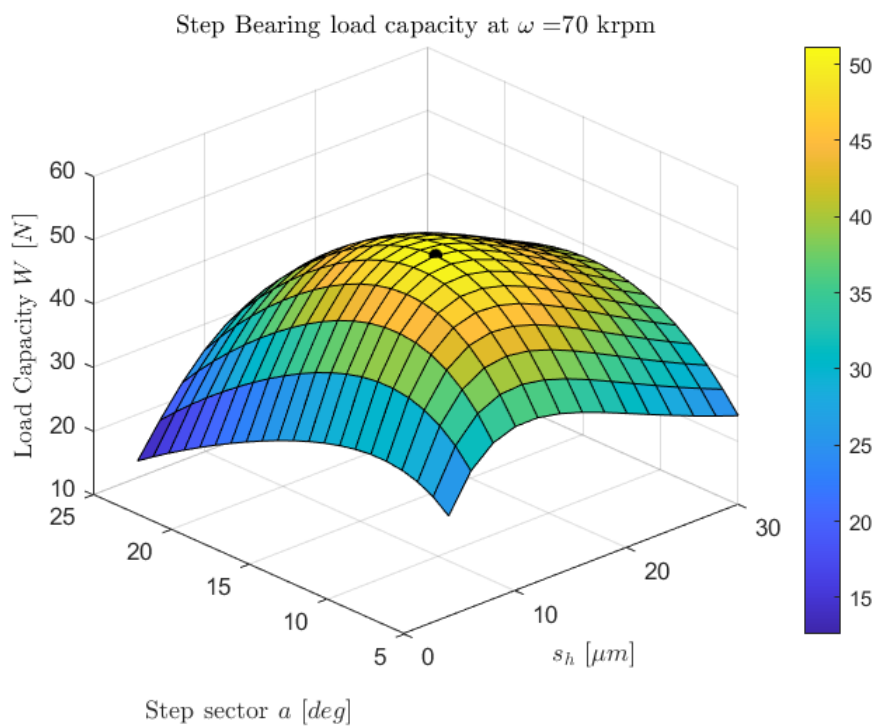


Figure 4.15: Step bearing, step depth and step sector effects on load capacity, default view

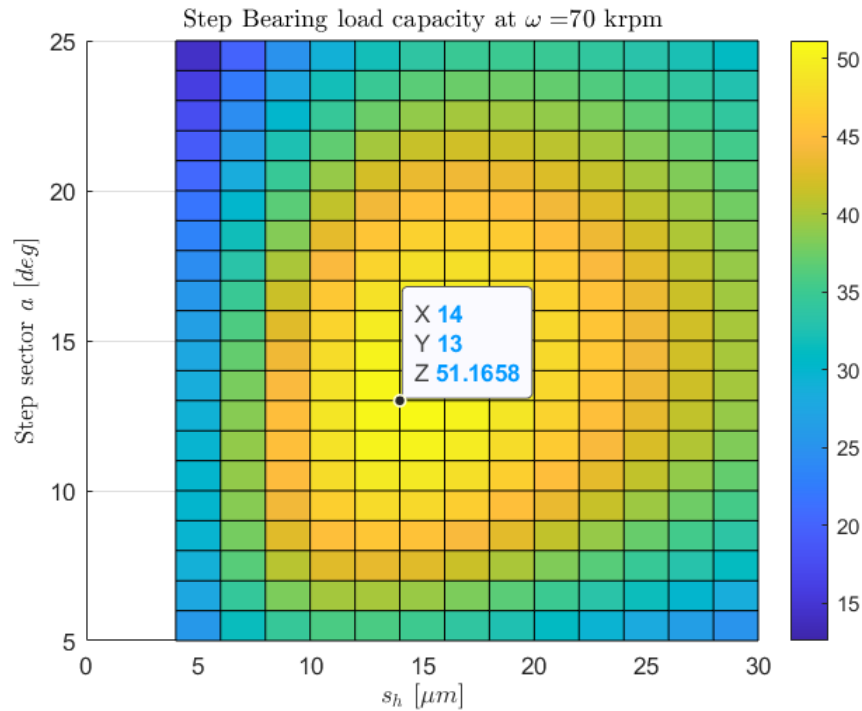


Figure 4.16: Step bearing, step depth and step sector effects on load capacity, $X - Y$ plane view

A geometry with $s_h = 14 \mu m$ and an angular step of $a = 13^\circ$ demonstrates the highest load capacity for this bearing type. Figure 4.17 presents a comparison between the optimized geometry and an initial generic design, which featured $s_h = 20 \mu m$ and an angular step of $a = 15^\circ$. The results clearly indicate that the optimized geometry significantly outperforms the generic one, particularly at lower air gap values. This highlights the sensitivity of this bearing type to geometric parameter variations, as even a relatively small refinement in design leads to a substantial increase in load capacity.

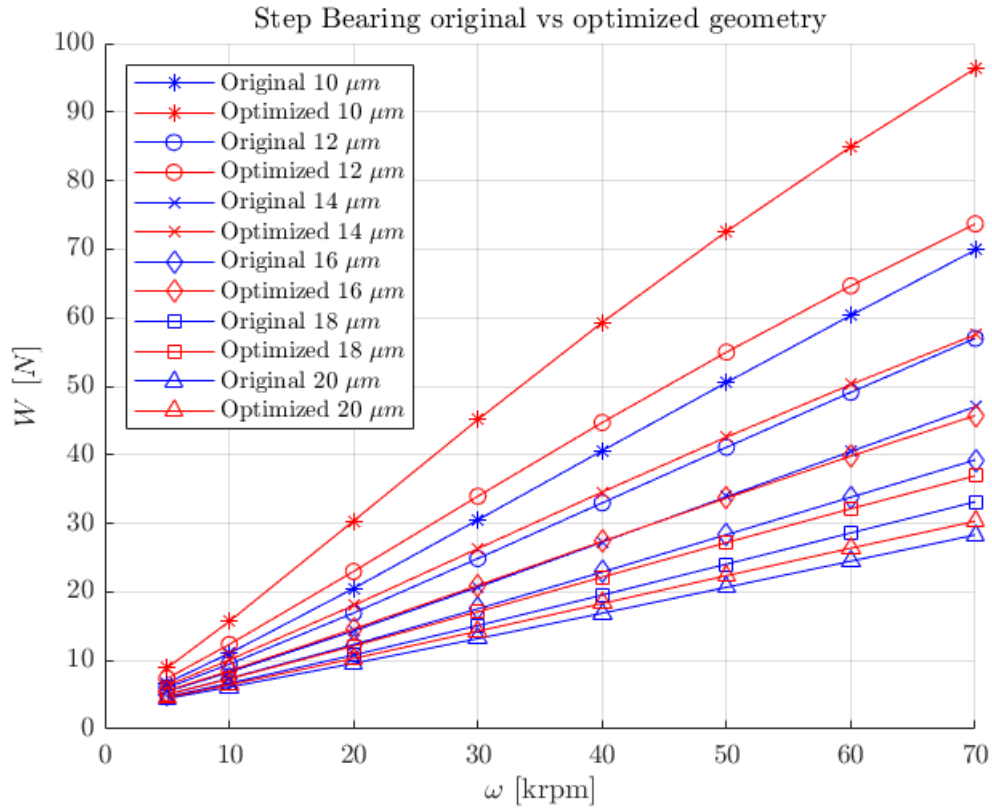


Figure 4.17: Initial generic geometry vs optimized geometry

4.2.4 Tapered

Surface Scan

A similar procedure for the Tapered bearing was carried out. However, this bearing presented a particular challenge. Since the geometry of the bearing has a slope that ends in a slot, the roundmeter went into overflow since the tip of the instrument would descend sharply and cause the error. In order to combat this problem, small bars that fitted into the slots had to be 3D printed. This made it, so there was a surface over which the roundmeter could measure, which then had to be cut from the date to not skew the measurements. A picture of the experimental setup can be seen in **Figure 4.18**.

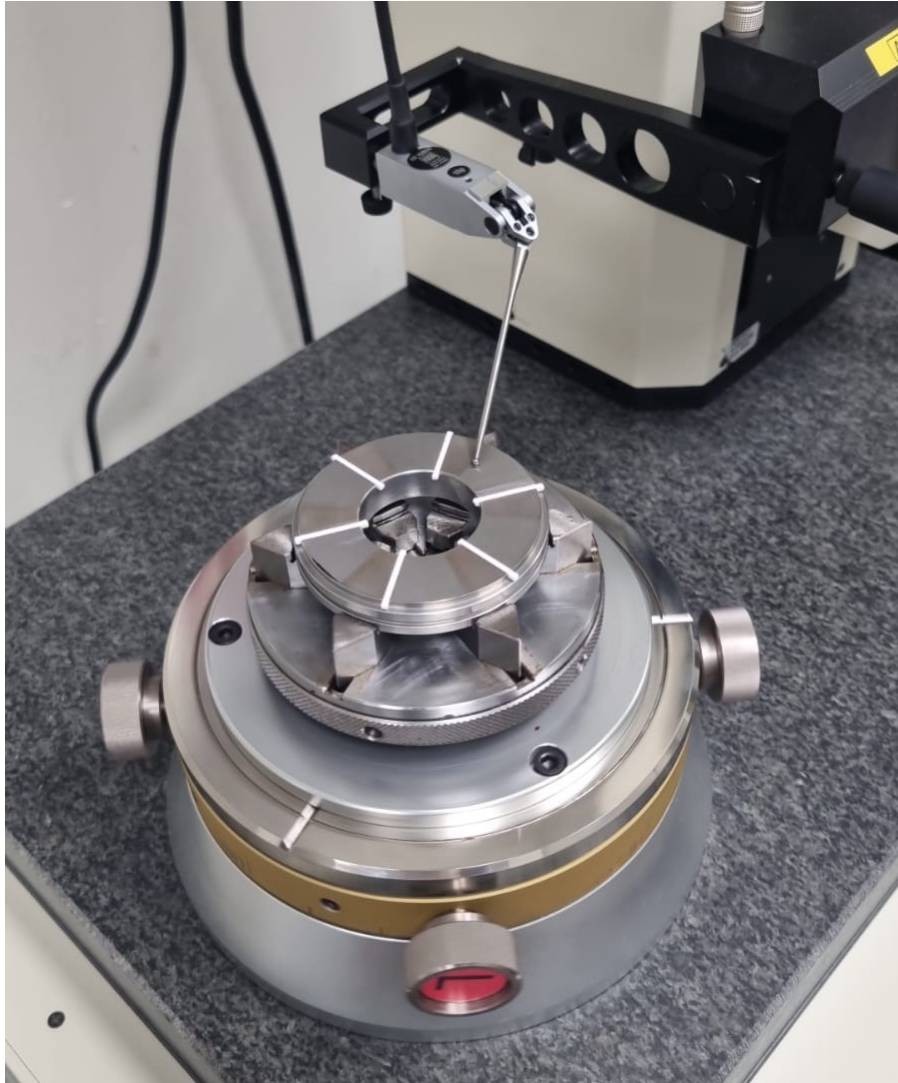


Figure 4.18: Roundmeter setup for the measurement of the Tapered bearing

The measured raw data was then plotted with the use of Matlab, as shown in **Figure 4.19**. It can be clearly seen that like the spiral grooved bearing, the Tapered bearing data presents an inclined profile that had to be corrected in the post-processing of the data. Following a similar procedure to the spiral grooved bearing, a plane was fitted into the data in order to achieve a level surface. Once the plane parameters were found, the data was translated to be level. Once this procedure was done, the results obtained are shown in **Figure 4.20**

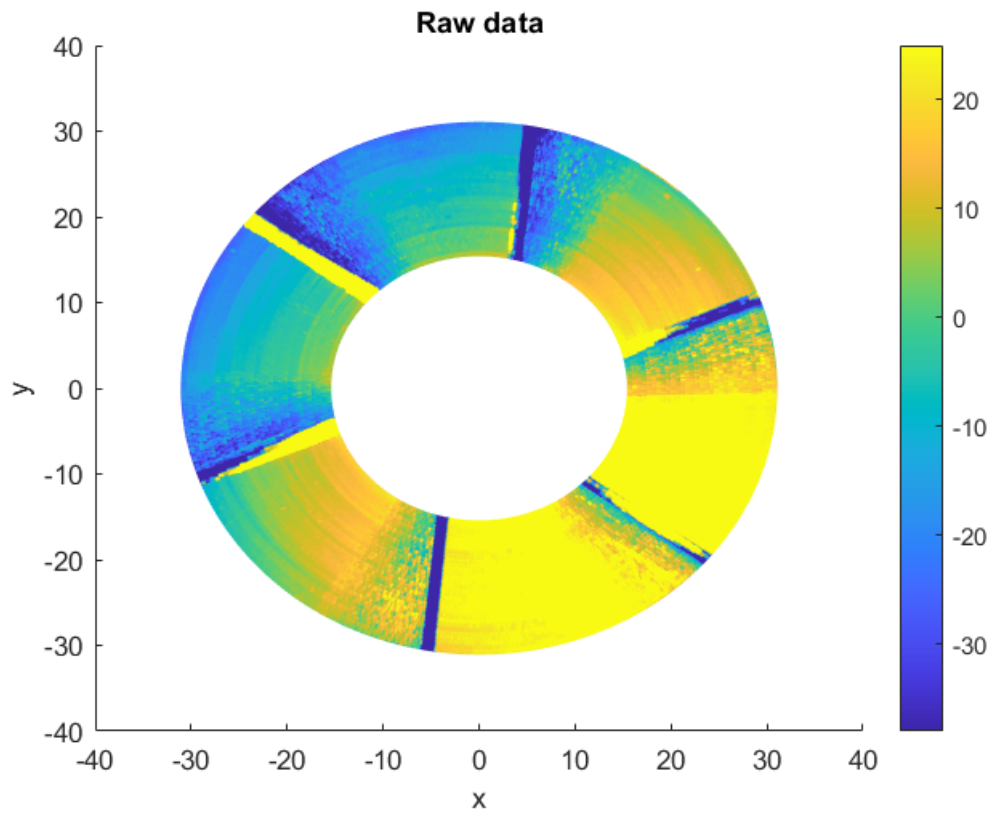


Figure 4.19: Tilted Bearing Surface raw data

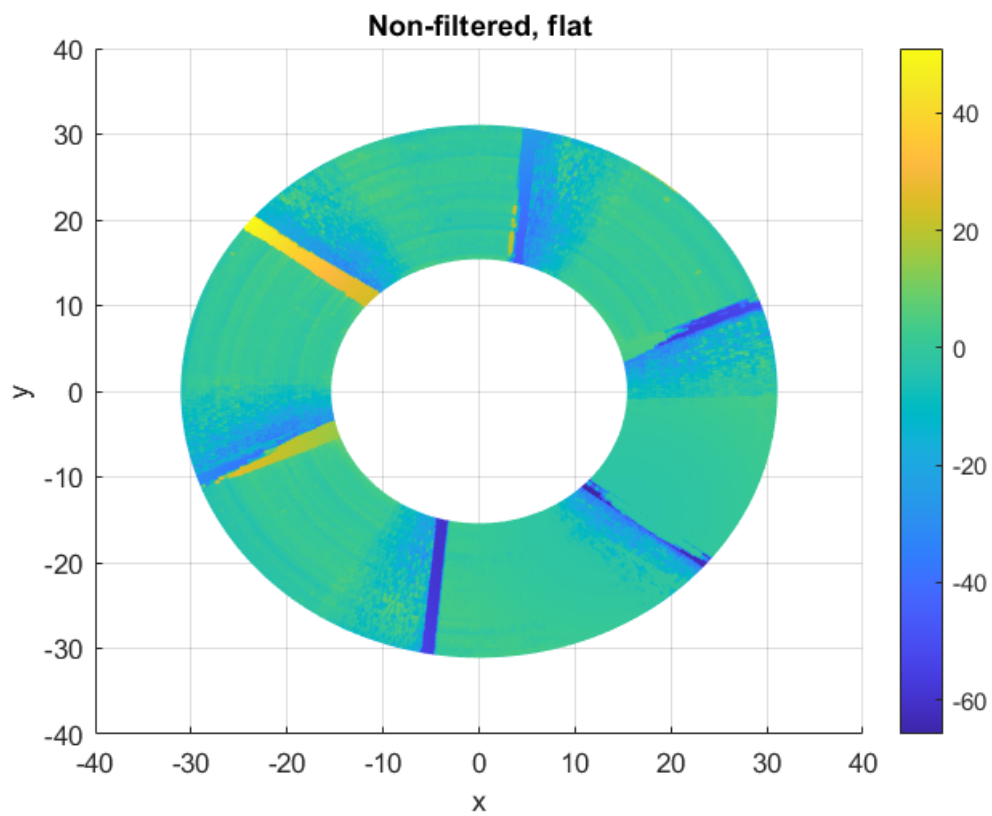


Figure 4.20: Tapered Bearing Surface flattened

The main difference in the post-processing between the Tapered bearing and the spiral grooved bearing is that the former has the 3D printed bars that need to be taken into account. The start and ending of each of the bars was identified, and that data was discarded by setting the value of the height of the surface in those points to NaN . Moreover, the same filtering process that was used for the spiral grooved bearing was used for the tiled pad bearing. Both of these procedures were implemented and can be seen in **Figure 4.21**.

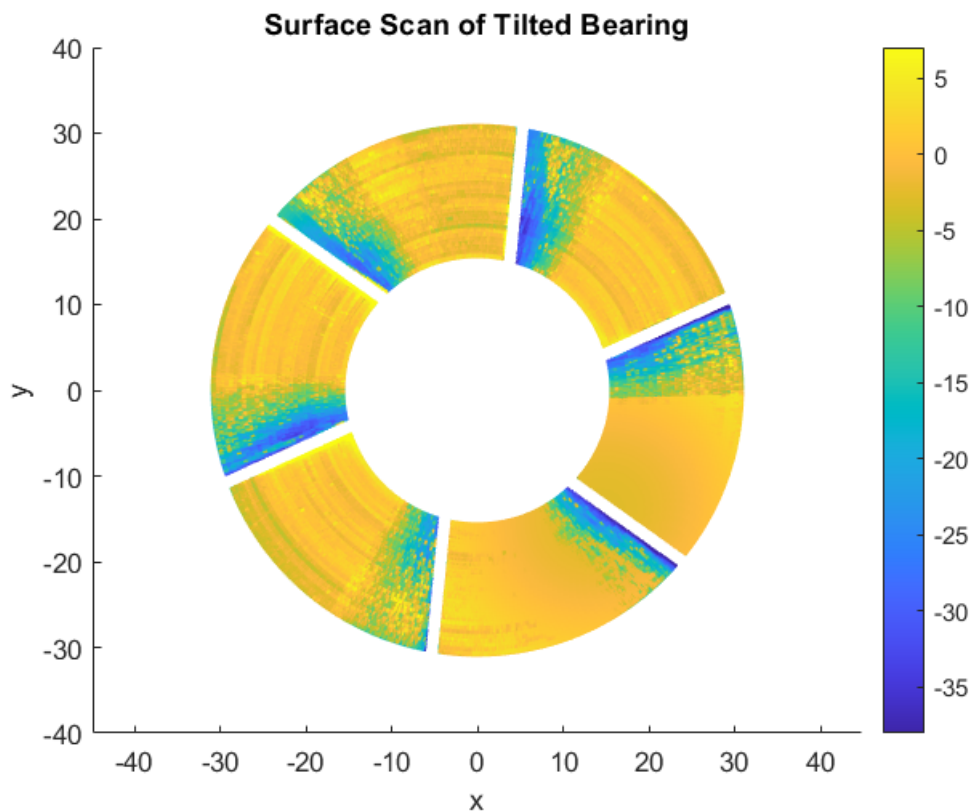


Figure 4.21: Tapered Bearing Surface scan in Matlab

With all of these procedures applied to the data, it was then possible to measure the tilt of each pad in order to evaluate the FDM model with the same parameters. The tilt was measured by fitting a plane to the tilted surface, once again using Matlab's *Curve Fitter* application, and calculating its inclination with relation to the flat surface of the bearing. These tilt angles are informed in **Table 4.2**. Moreover, in order to get accurately calculate the tilt angle of each pad, the pads themselves had to be identified since the bearing consists of a flat surface that then descends with these pads. The angular extension of the pads was calculated to be $\alpha_{pad} = 16.5^\circ$.

Pad number	Tilt [<i>deg</i>]
Pad 1	4.85
Pad 2	4.07
Pad 3	6.06
Pad 4	3.48
Pad 5	6.16
Pad 6	5.00
Mean Pad Tilt	4.94

Table 4.2: Angular tilt of every pad present in the bearing

Finally, to fully describe the bearing's geometry, the extent of the descent of the pads had to be obtained. Meaning that a mean value of maximum depth of the pads had to be calculated. In order to do this, the height of each pad was plotted at the inner, middle and outer radius. These measurements are shown in **Figures 4.22-4.24**. With these graphs it was possible to state that the pads have a slope that starts level with the flat faces of the bearing and then descends to $30\ \mu\text{m}$

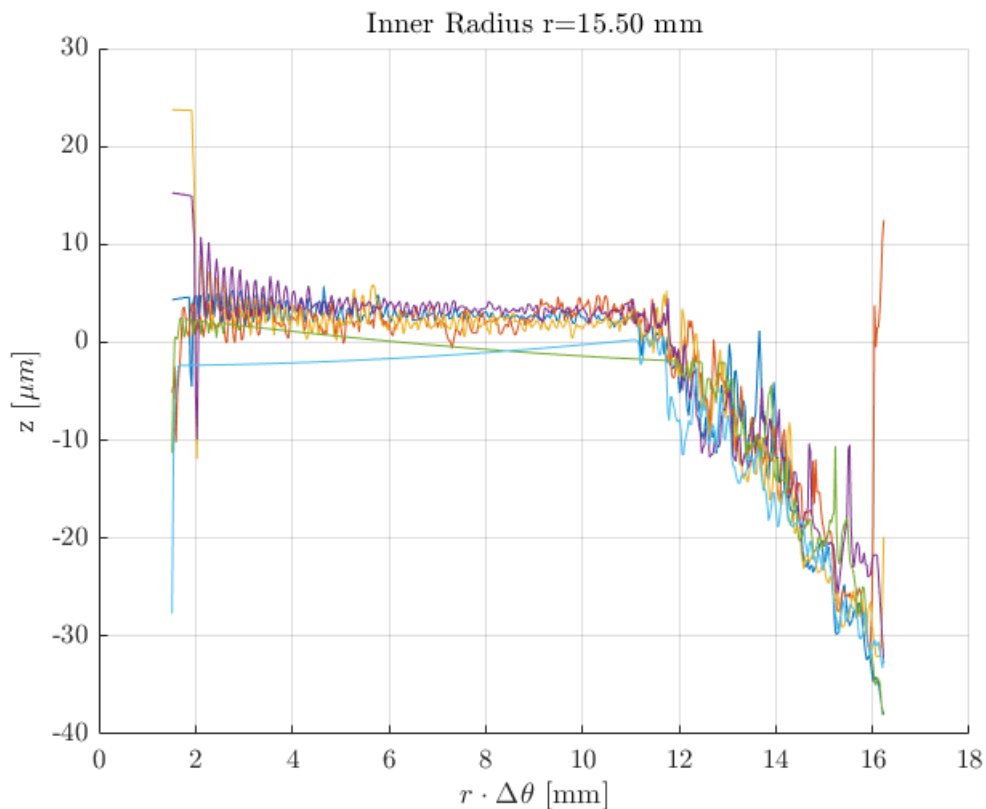


Figure 4.22: Tapered Bearing inner radius pad depth

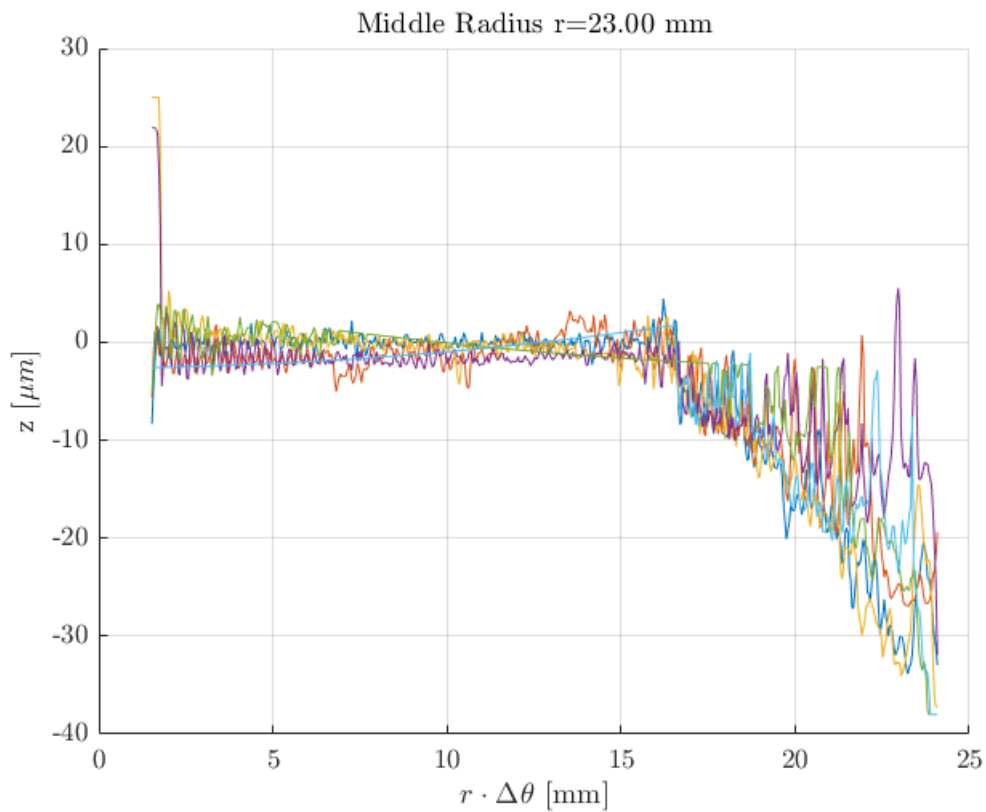


Figure 4.23: Tapered Bearing middle radius pad depth

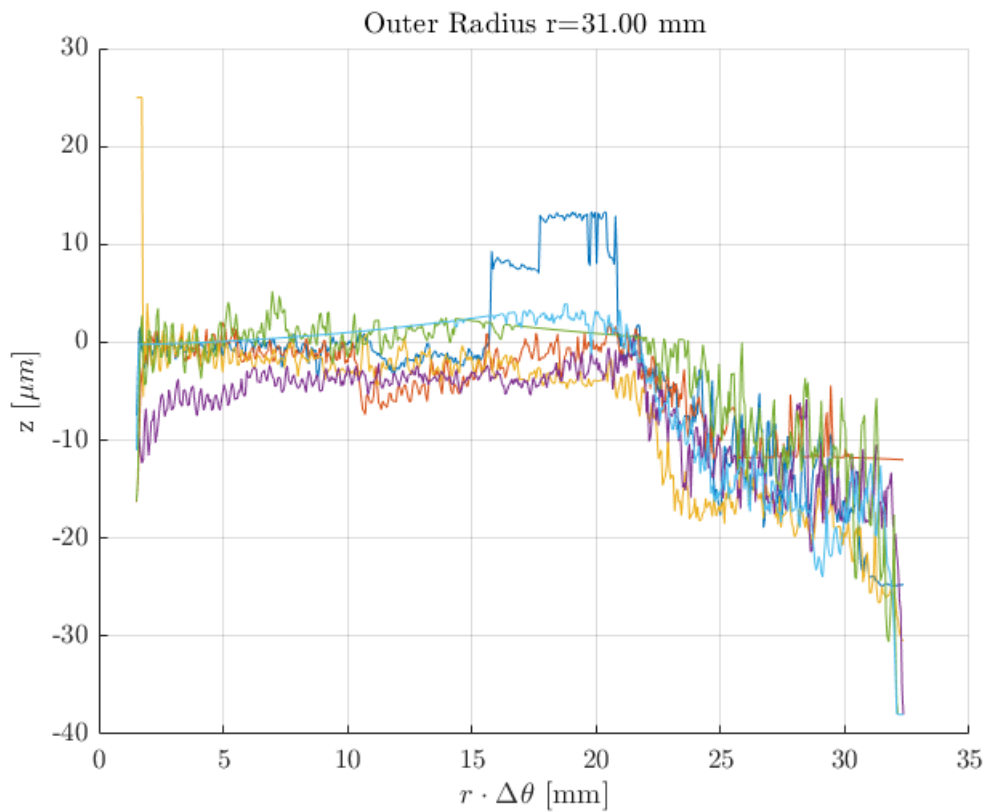


Figure 4.24: Tapered Bearing outer radius pad depth

Similarly to the spiral bearing, the average pad profile was calculated for the tapered bearing. This was done by getting the profile height at each point of each pad and averaging the height value at individual point. The result of this procedure can be seen in **Figures 4.25-4.26**.

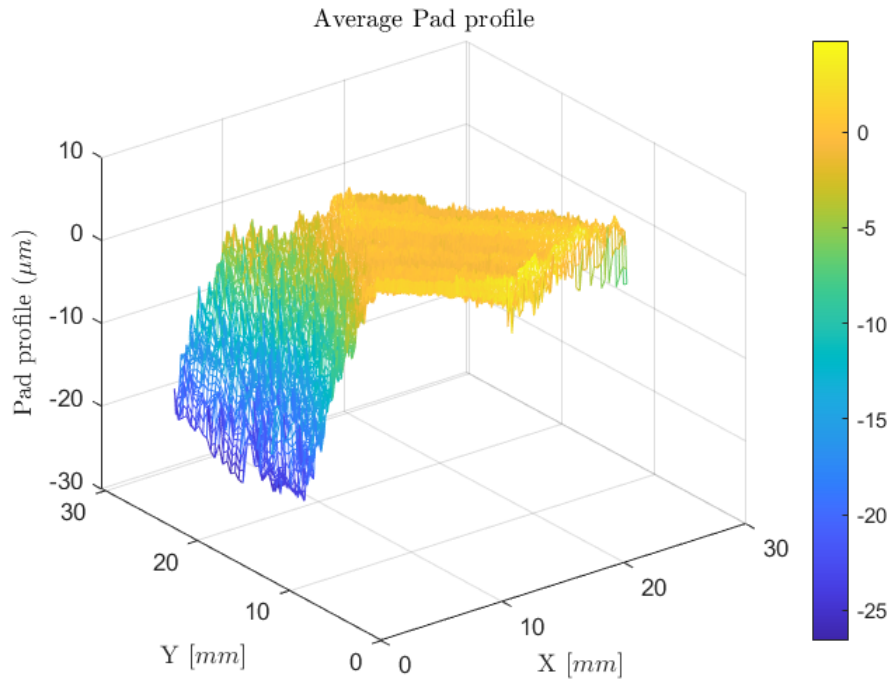


Figure 4.25: Tapered Bearing average profile

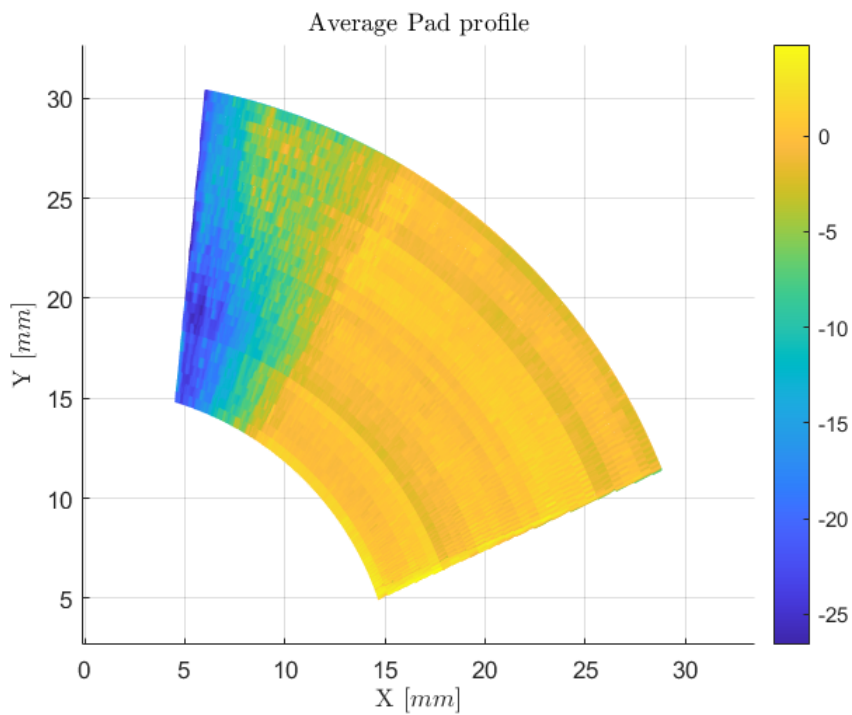


Figure 4.26: Tapered Bearing average profile, top view

Simulations

As previously discussed in the section on the Slider bearing, the Tapered bearing generates a high-pressure peak, as seen in **Figure 4.27**, due to its converging section. Unlike the Slider bearing, however, the Tapered bearing maintains this elevated pressure over a larger portion of the geometry. This is achieved through the presence of a flat ridge, which neither compresses nor decompresses the fluid further, allowing the bearing to sustain a high load capacity over an extended area.

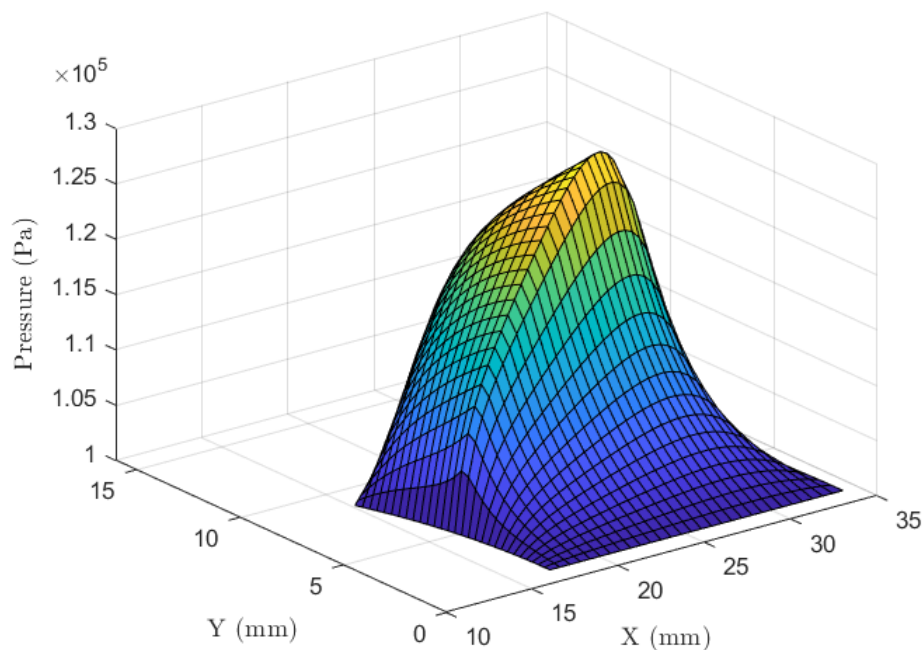


Figure 4.27: Tapered Bearing simulated pressure field using the FDM method

Dynamic Simulation

Measurements were performed under three loading conditions characterized by the inclination of the test bench. These were $\alpha = 15^\circ = 3.5 N$ (in red), $\alpha = 30^\circ = 6.5 N$ (in black) and $\alpha = 53.3^\circ = 10.5 N$ (in blue), as seen in **Figure 4.28**. As expected, the values of the air gap for every case are lower than the ones of the simulations. This could be due to the fact that since the system is real, lower performance is to be expected, and thus a much lower air gap was needed for the bearing to achieve the same load capacity than the simulation.

The experimental results for the measured air gap at different load cases showed a significant deviation from the values predicted by the numerical model. This discrepancy can be attributed to several real-world factors that were not accounted for in the simulation.

One of the primary sources of error is surface degradation of the bearing over multiple test cycles. As the tests progressed, minor wear or damage to the bearing surface could have altered the actual air gap, introducing variations that were not reflected in the idealized numerical model. Additionally, misalignment between the bearing and the shaft may have led to inconsistent air gap measurements, further contributing

to the observed differences. Another factor influencing the results was the bearing's support mechanism, which relied on tolerances in the housing cap. As discussed previously, this type of support can introduce micro-displacements, affecting the overall stability and accuracy of the measured air gap.

Even after applying the systematic error correction procedure described in **Chapter 2**, the translated experimental data remained significantly different from the simulated results. To compensate for this discrepancy and better compare the trends between experimental and simulated curves, the simulated results were uniformly shifted by $9\ \mu\text{m}$. This adjustment allowed for a more meaningful analysis of the model's predictive capabilities despite the inherent limitations of the experimental setup.

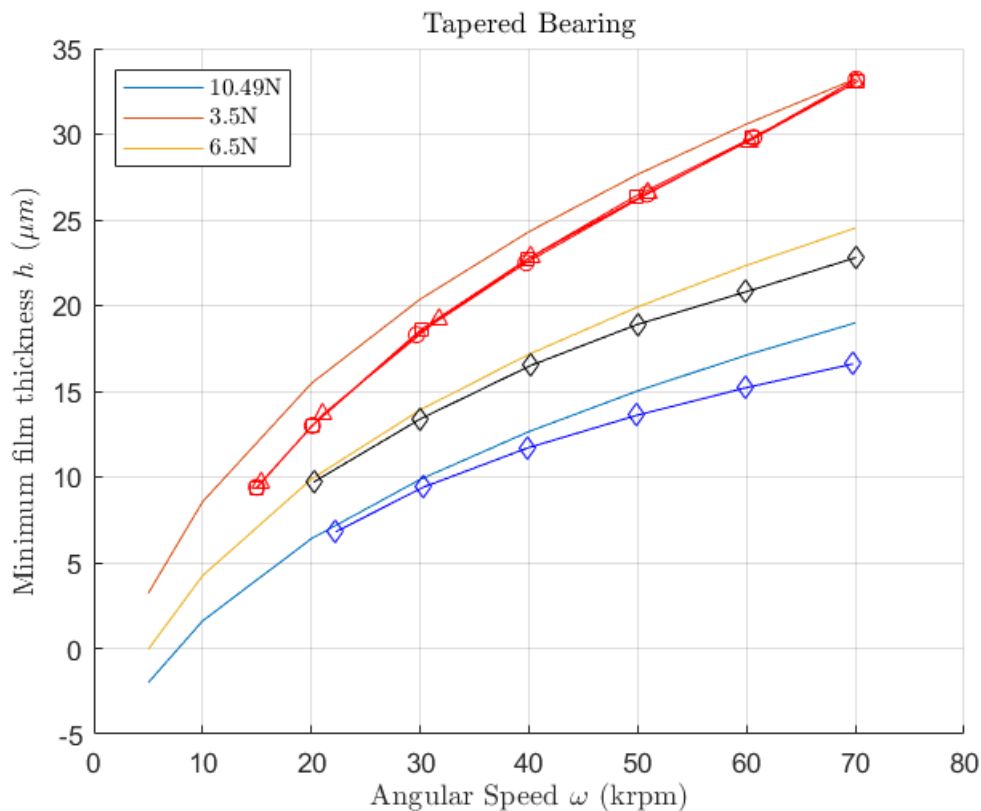


Figure 4.28: Tapered Bearing dynamic simulation with measured air gaps

Optimization

Similarly to the step bearing, the parameters to be optimized are the maximum groove depth s_h and the angular ridge sector a , as shown in **Figures 4.29-4.30**.

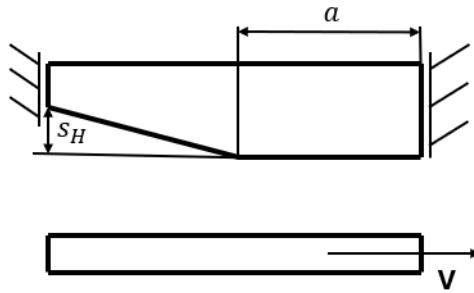


Figure 4.29: Tapered Bearing side section depicting s_H and a

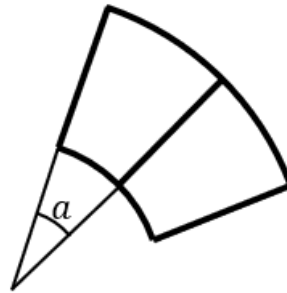


Figure 4.30: Diagram depicting a from the top view

A sweeping analysis of the combination of these two was carried out using an angular speed of $\omega = 70 \text{ krpm}$ and a constant air gap of $h_2 = 15 \mu\text{m}$. The results of this sweep are shown in **Figures 4.31-4.32**.

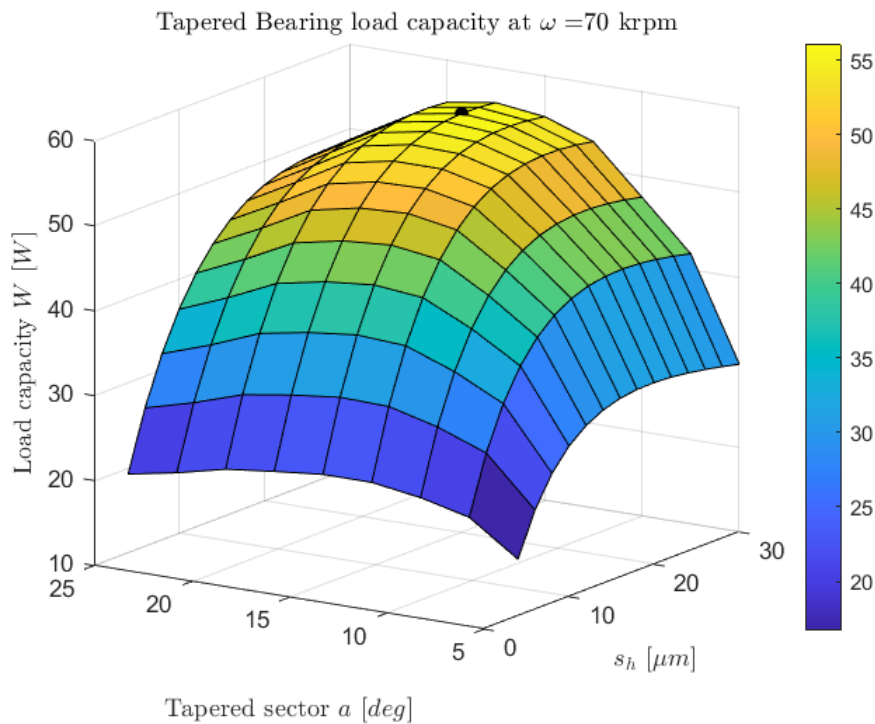


Figure 4.31: Tapered bearing, maximum groove depth s_h and taper sector a effects on load capacity

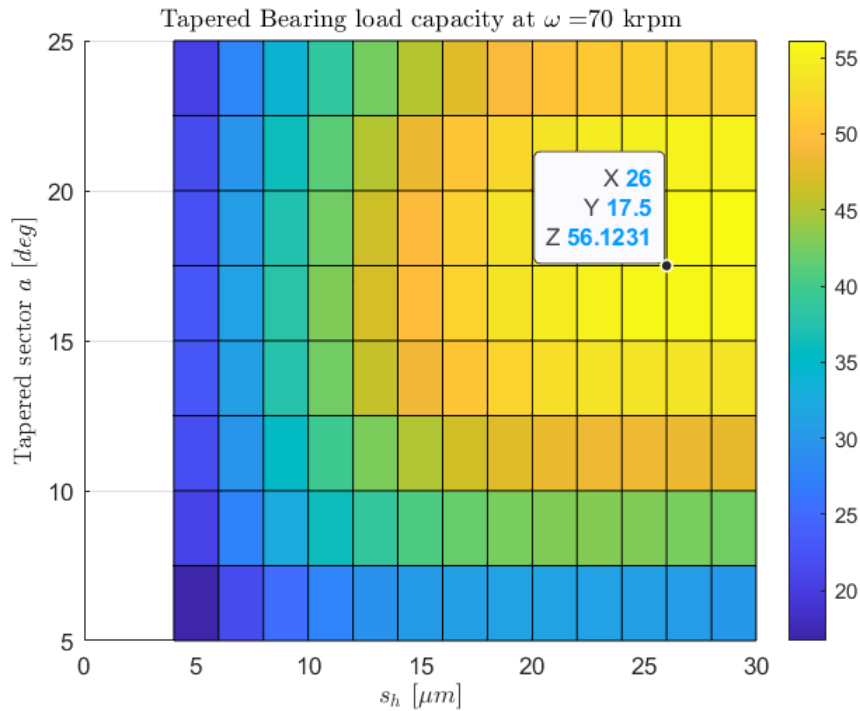


Figure 4.32: Tapered bearing, maximum groove depth s_h and taper sector a effects on load capacity, top view

The optimal geometry for the tapered bearing, as illustrated in **Figure 4.32**, corresponds to a design with $s_h = 26 \mu\text{m}$ and a tapered angular sector of $a = 17.5^\circ$. For comparison, a geometry with the same characteristics as the initially studied tapered bearing was analyzed, featuring $s_h = 25 \mu\text{m}$ and $a = 16^\circ$. This indicates that the initial geometry was already very close to the optimal configuration, as shown in Figure 4.33. While a slight improvement in performance is observed at higher air gap values, the difference is minimal and not highly significant.

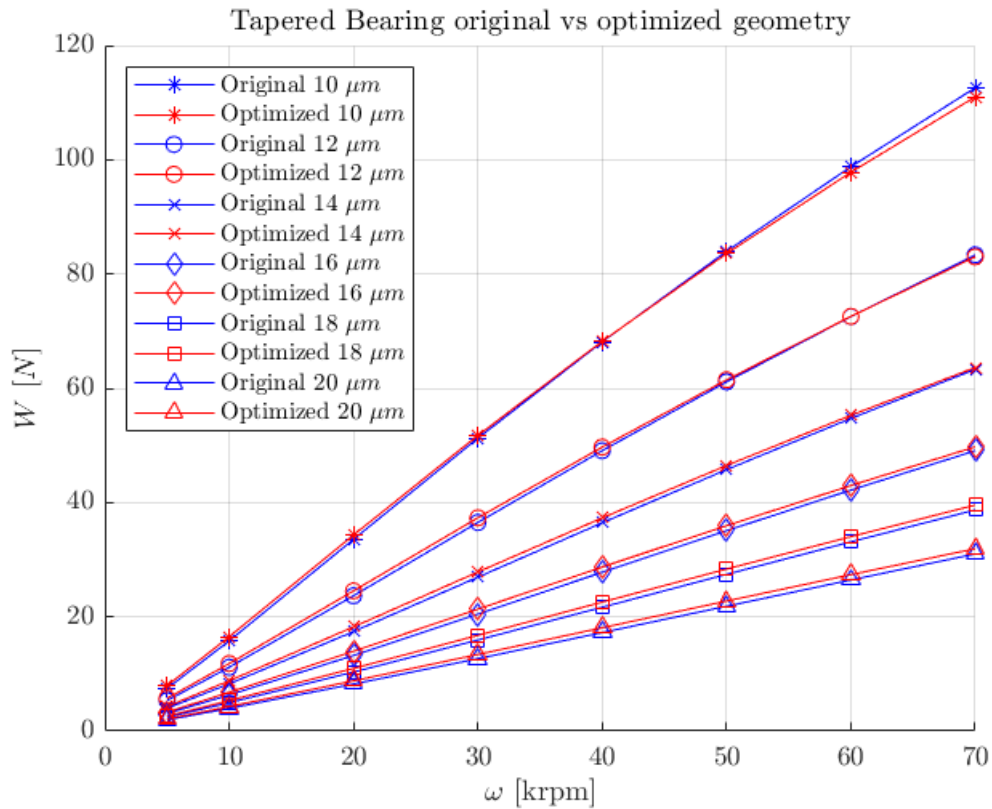


Figure 4.33: Tapered bearing load capacity comparison between initial and optimized parameters at $\omega_{min} = 5 \text{ krpm}$

4.2.5 Spiral

Surface Scan

The measurement data was subsequently imported into Matlab for post-processing, since the data showed some systematic errors. Firstly, the data exhibited a slight tilt, as can be seen in **Figure 4.34**. The surface of the upper part of the bearing (positive y) has a higher value than the lower part (negative y) for example. Rotating the view of **Figure 4.34**, this tilt can be clearly seen, as shown in **Figure 4.35**.

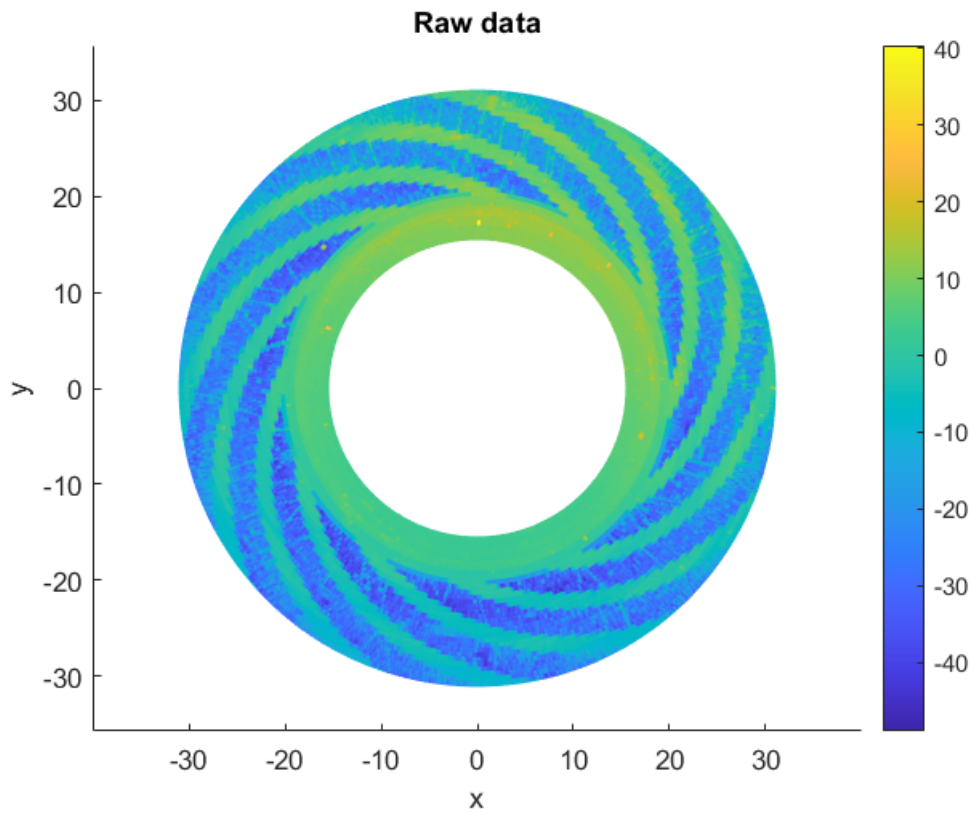


Figure 4.34: Spiral Bearing Surface scan raw data

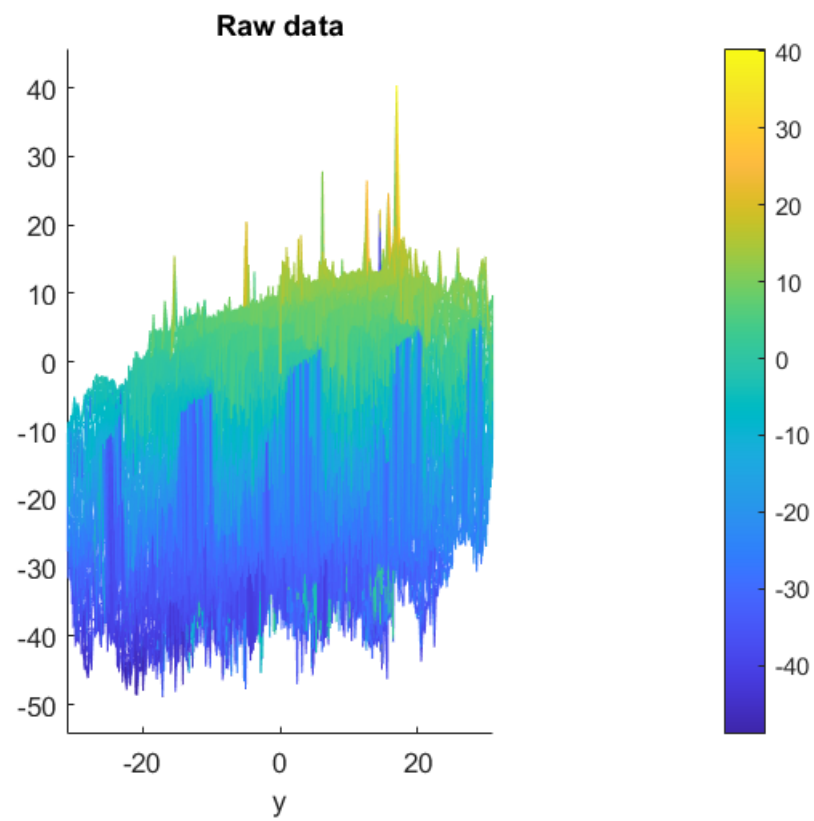


Figure 4.35: Spiral Bearing Surface scan raw data side view

To solve for this observation, a plane was fitted into the data in order to correct the data. This plane only used the points from the inner ring without grooves, since this part was untouched in the manufacturing process, and thus should be flat, and it also has no grooves that may interfere with these corrections. The Matlab application "Curve Fitter" was used in order to verify a correct fit value R^2 . From **Figure 4.36** it can be seen that the value R^2 is acceptable, as it is higher than 0.9, a usual benchmark for the validity of an approximate fit.

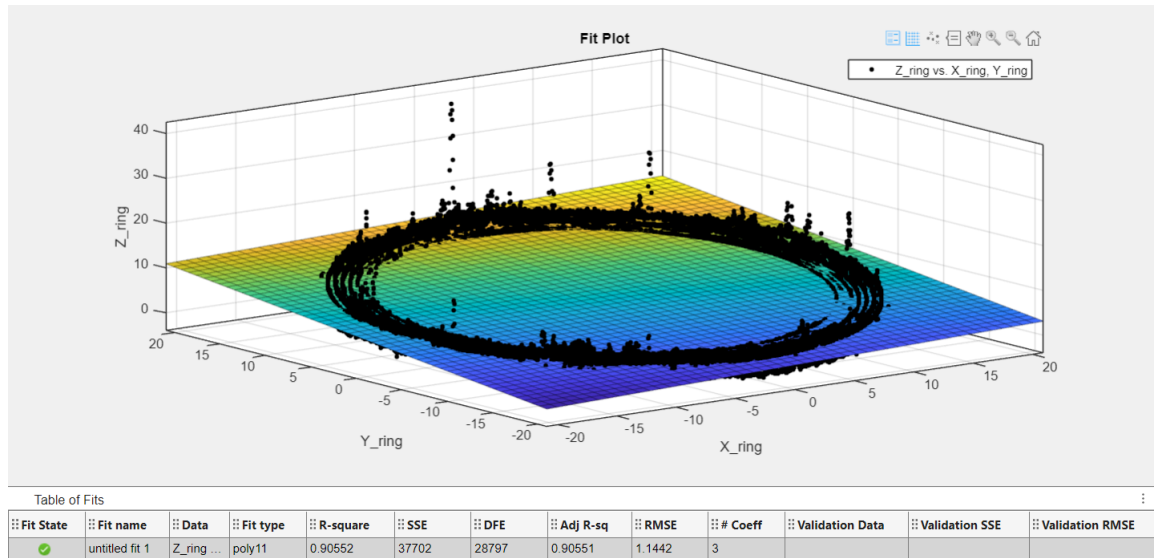


Figure 4.36: Plane fitting using curve fitter

Once the plane was obtained, the next step was to translate the data such that the bearing surface was flat. In order to perform this translation, the distance from any point to the fitted plane was calculated and then all the points were translated in accordance to this distance. Doing it this way ensured that the groove geometry and depth would remain untouched, and thus no data would be lost. The result of this process can be seen in **Figures 4.37-4.38**. The latter (side view) shows clearly how the data is now flat and not tilted as it was previously, specially when compared with **Figure 4.35**

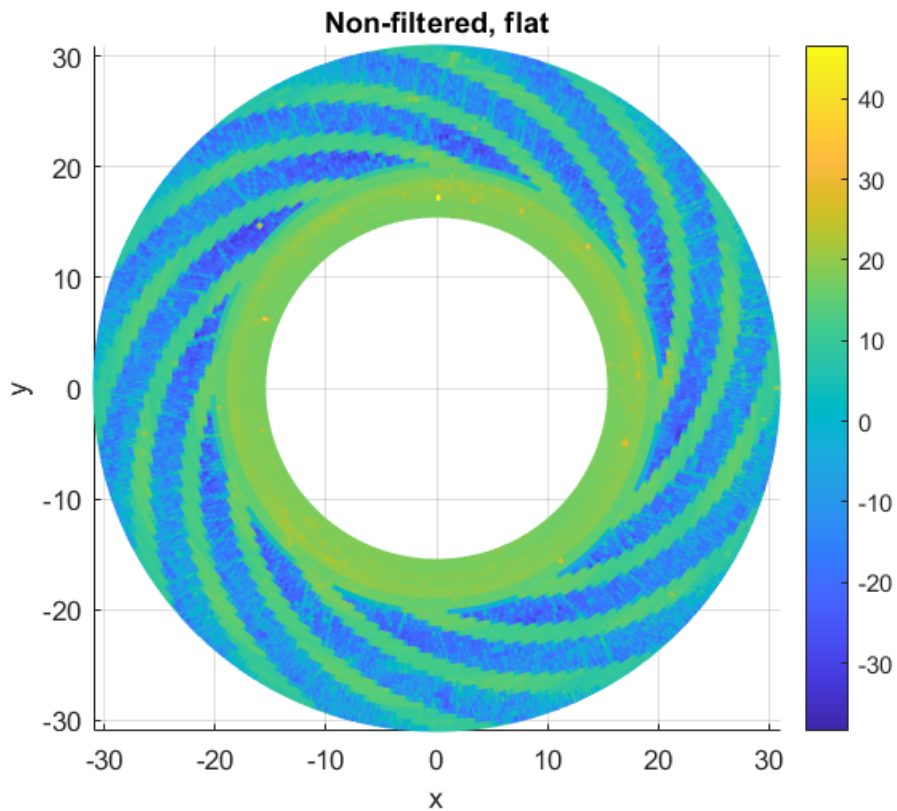


Figure 4.37: Flattened geometry top view

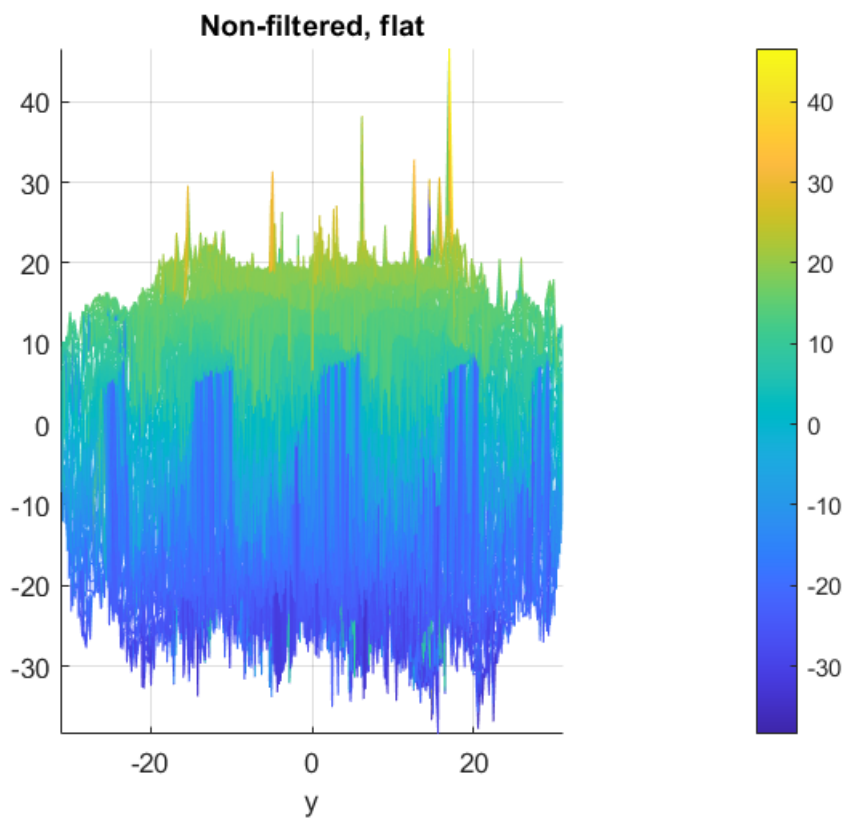


Figure 4.38: Flattened geometry side view

The next step that was done was to get rid of the outlier points in the data. Some of these outliers can be seen in **Figure 4.34-4.38**. In order to do this, Matlab's *isoutlier* function was used. This function automatically detects the outliers and informs their position in the given array. Once identified, the selected method of correction was to take the local average of the points directly connected to the outlier in question. This means that using polar coordinates, the points located one $\Delta\theta$ to each side and one Δr radially were used to calculate the mean. This value then replaced the original outlier. 3600 outliers were found using this method and the resulting data is shown in **Figure 4.39**.

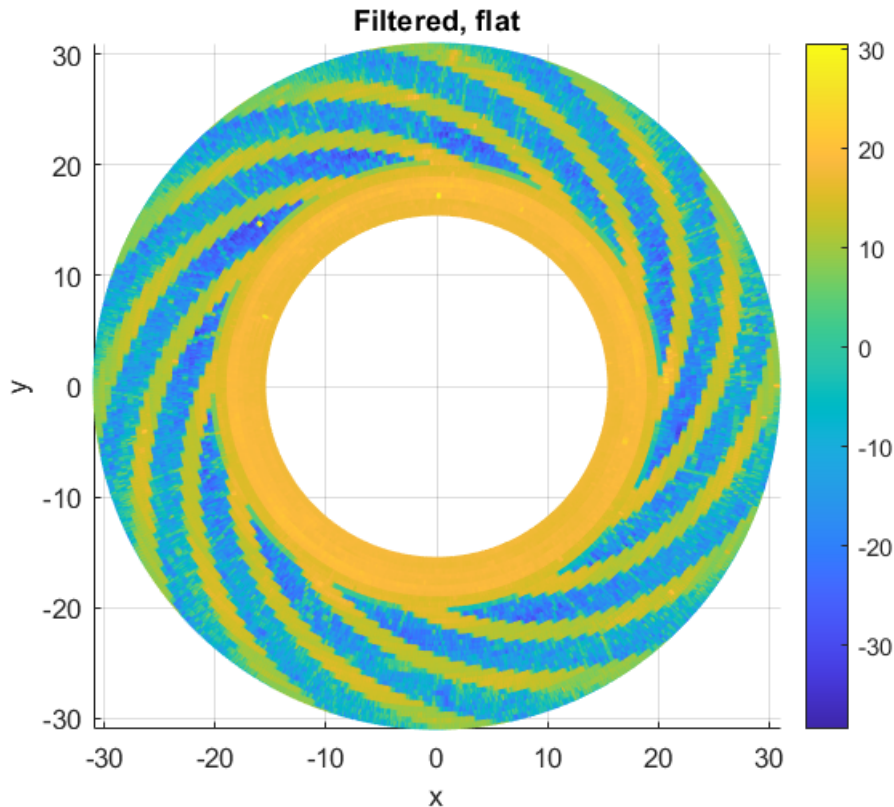


Figure 4.39: Filtered and Flattened geometry data

Once the data was processed accordingly, the analysis of the groove parameters and thus the measurement of their depth could be carried out. In order to get the parameter values, an iterative method using was carried out. After various iterations, the recorded values for the bearing are the ones informed in **Table 4.3** and are seen graphically represented in **Figure 4.40**.

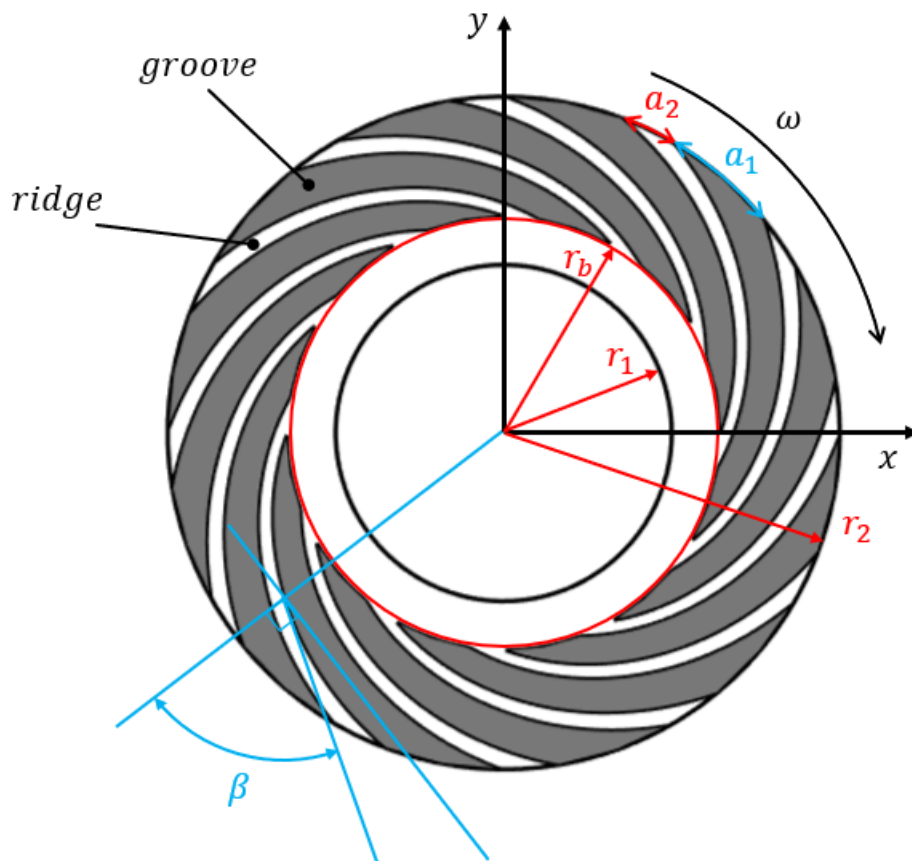


Figure 4.40: Parameters of an aerodynamic Spiral Grooved thrust bearing

$h_{0,mean}$	22.62 mm
$a_{1,f}$	11.5 mm
$a_{2,f}$	6 mm
β	70°
r_1	16 mm
r_b	20 mm
r_2	33 mm
N	12

Table 4.3: Measured properties of the grooved spiral bearing

Table 4.3 informs the measured values of the spiral bearing. Expanding on the meaning of some of these values, $a_{2,f}$ and $a_{1,f}$ are the sector length at the outer radius (r_2) of the groove and the land part of the bearing respectively. α refers to the ratio of a and b such that $\alpha = a_2/a_1$. Note that α stays constant regardless of the radius in which a_1 and a_2 are measured. However, it is a common practice to measure both these parameters at the outer radius.

In order to check that these parameters are in accordance to the physical bearing, a superposition of a theoretical bearing with the parameters from **Table 4.3** and the scanned surface from **Figure 4.39** was done, as show in **Figure 4.41**.

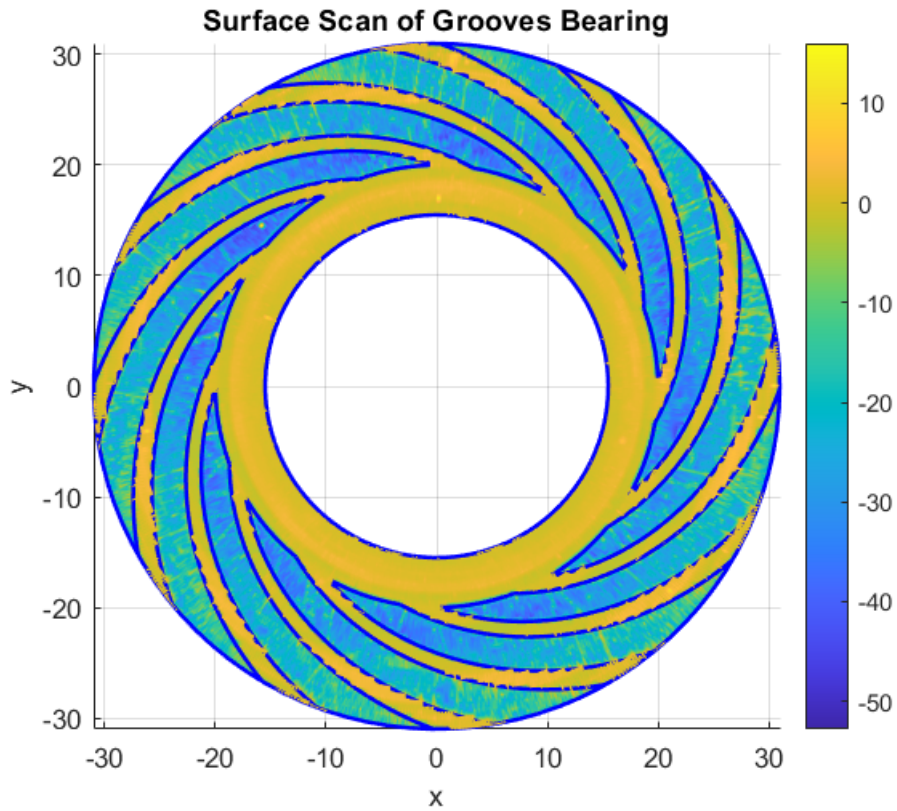


Figure 4.41: Graphical comparison and verification of the parameters of the bearing

With the use of **Figure 4.41**, it was possible to state that the parameters from **Table 4.3** are correct and thus, the mean groove depth can be calculated. To do this calculation, the data was separated into grooved and non-grooved points as shown in **Figures 4.42-4.43**.

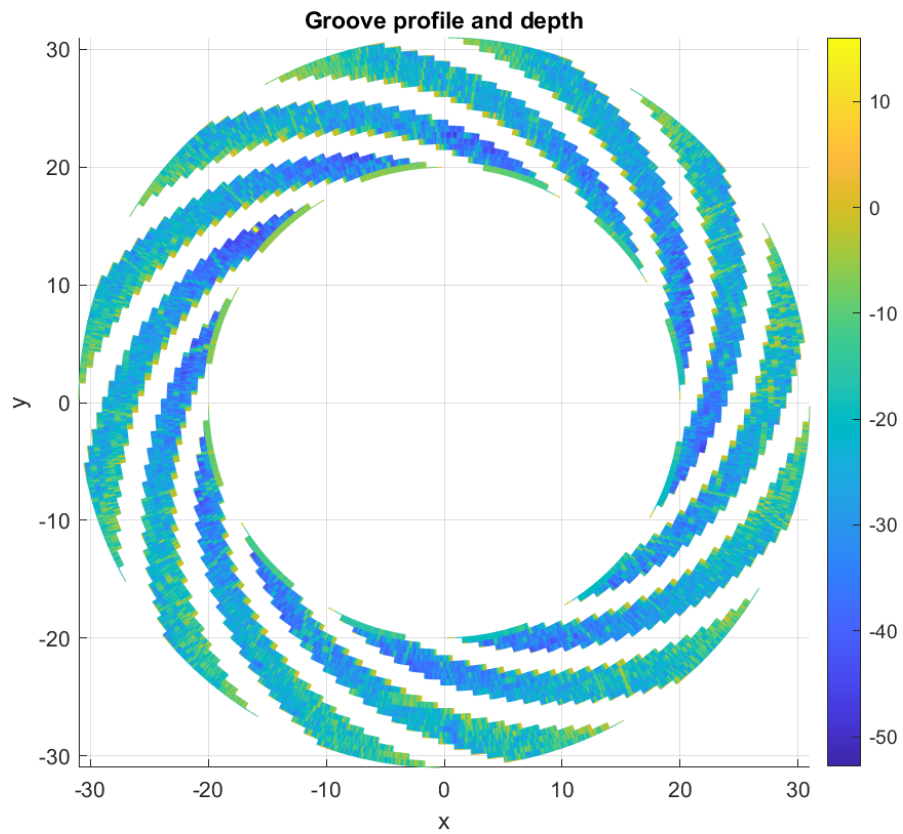


Figure 4.42: Isolated data from the grooves

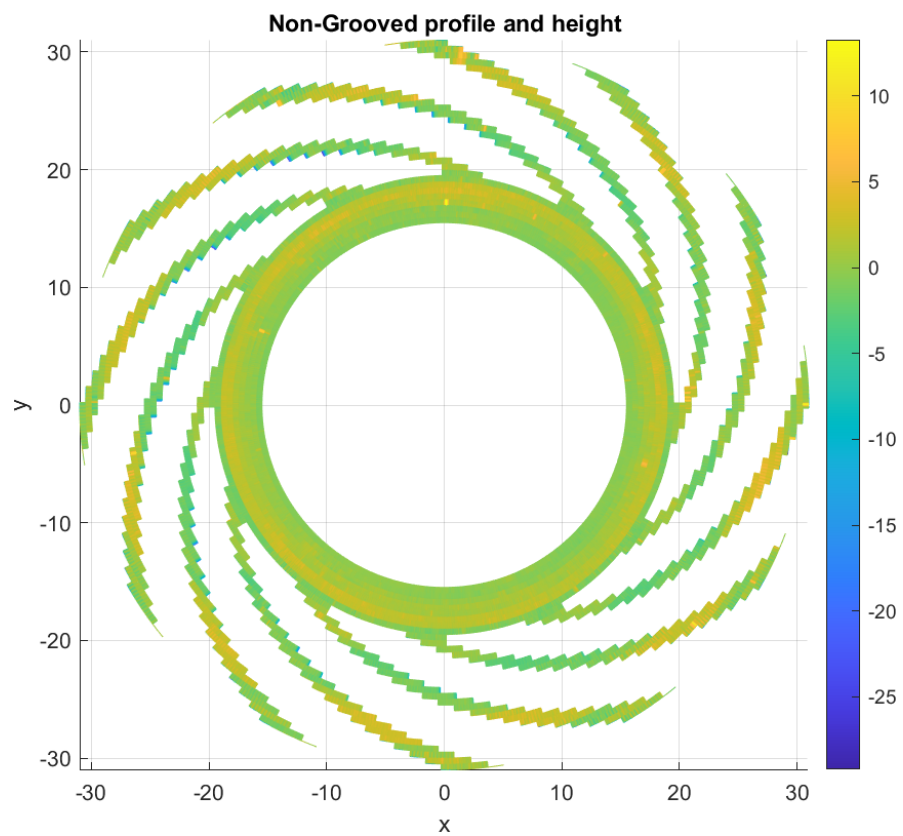


Figure 4.43: Isolated data from the non-grooved part of the bearing

It is important to know that the grooves present in the spiral bearing are not of constant depth, as is clear from the figures present in this chapter. Thus, in order to more accurately simulate the bearing's performance with the numerical model specified in **Section 3.2**, an average radial depth was calculated and then applied to the FDM model. This radial average was obtained by calculating the mean depth of the groove in each sampled ratio in the grooved part of the bearing. For this the data shown in **Figure 4.42** was separated by the value of the radial coordinate of each point. All the groove depths of the points in the same radius were averaged to get the mean groove depth at that specific radius. After this, a 9th degree polynomial function (the highest degree polynomial that Matlab's *Curve Fitter* allows using) was calculated in order to recreate as closely as possible the groove depth profile along the grooves of the mathematical model. The main reason to do this and not just copy and paste the data of the grooves in the model is that, by using symmetry the model will only perform the calculation for a 30° sector of the bearing, and since all the grooves present slightly different groove depth profiles, this method was needed. **Figure 4.44** shows how the result of applying this procedure to the mesh. It is clear by the color gradient how the groove depth varies with the radius, creating a much an environment for the simulation that is much closer to reality than just applying the mean groove depth to the grooved part.

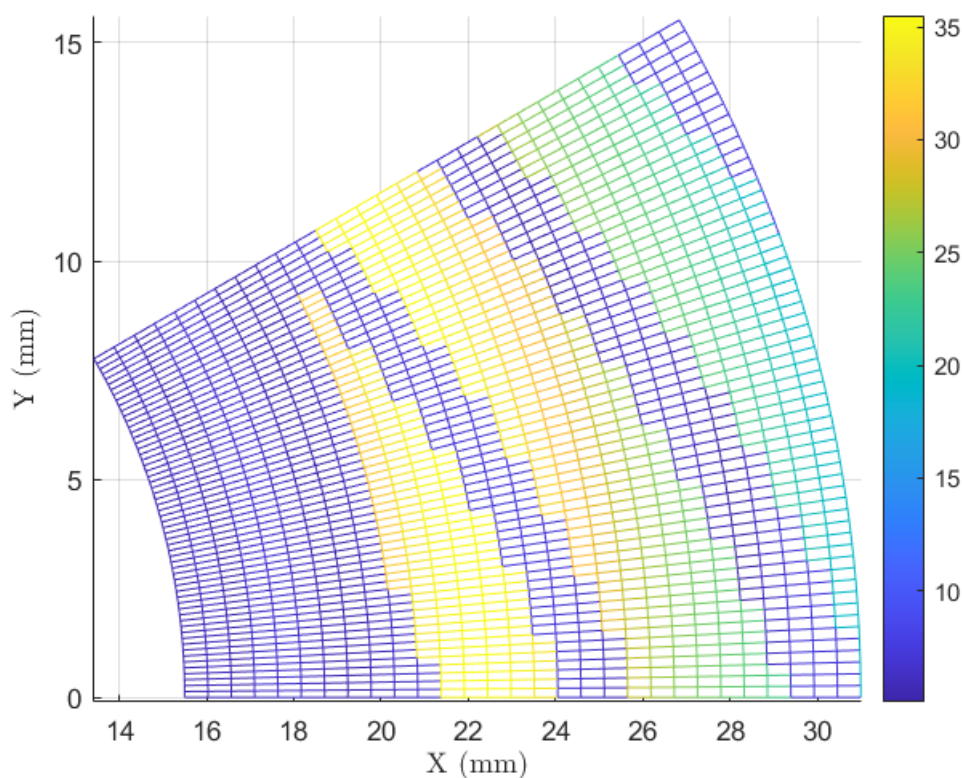


Figure 4.44: 30° Sector meshed with average radial depth applied to the mesh

Simulations

Static The first simulation aimed to calculate the pressure distribution within the bearing domain, as described in Chapter 3. This was achieved by imposing a fixed

air gap and rotational speed, allowing for the evaluation of the aerodynamic thrust bearing's performance under different operating conditions. The analyzed air gaps ranged from 3 to 8 μm , with a step of 1 μm , while the rotational speeds varied from 10krpm to 190krpm, with a step of 20krpm.

To ensure the validity of the results, each simulation iteration was carefully examined. This validation process involved visually analyzing the generated pressure field, as depicted in **Figures 4.45-4.46**. These figures illustrate how the pressure field aligns with the expected behavior of the bearing type and its geometry. Specifically, a distinct pressure peak appears at the start of the spiral, with the pressure gradually increasing toward this region. Additionally, a noticeable increase in pressure was observed at locations where a step in the geometry was present—namely, at the secondary spiral grooves incorporated within the reduced model. This behavior corresponds well with theoretical expectations, further reinforcing the accuracy of the simulation.

Moreover, the absence of irregular pressure peaks confirmed the correctness of the meshing process. In cases where the mesh is poorly structured or contains numerical inconsistencies, unexpected pressure discontinuities may arise. The smooth and well-distributed pressure profile obtained in these simulations indicates that the meshing was successfully implemented.

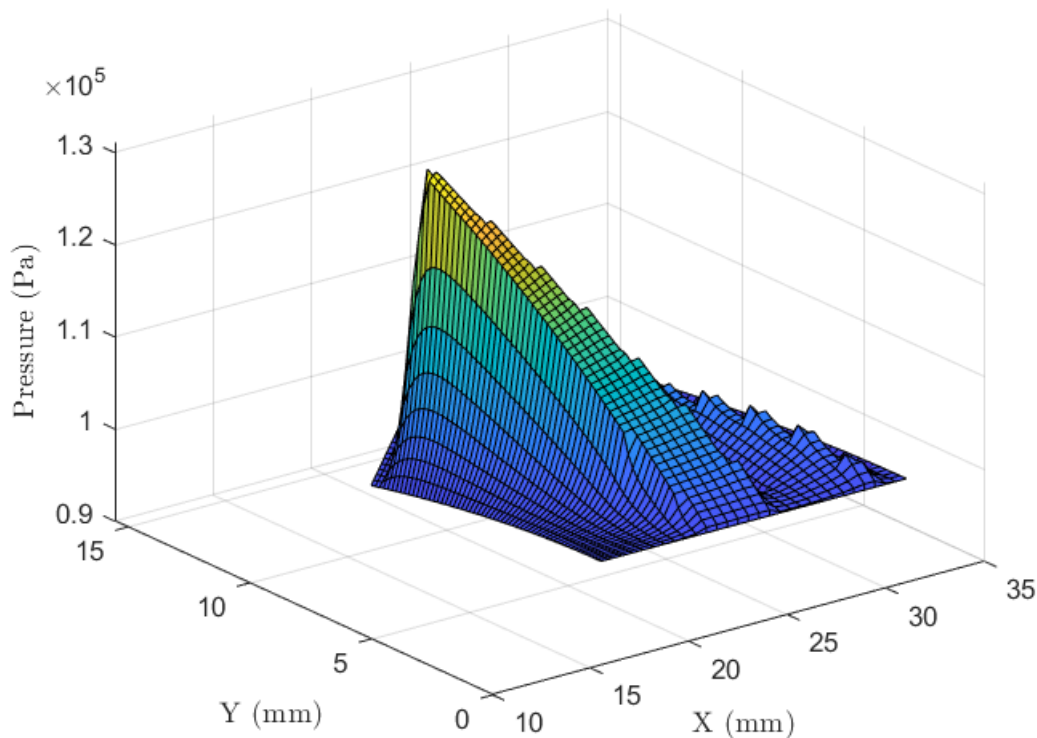


Figure 4.45: Isometric view of the pressure field of the studied spiral bearing section

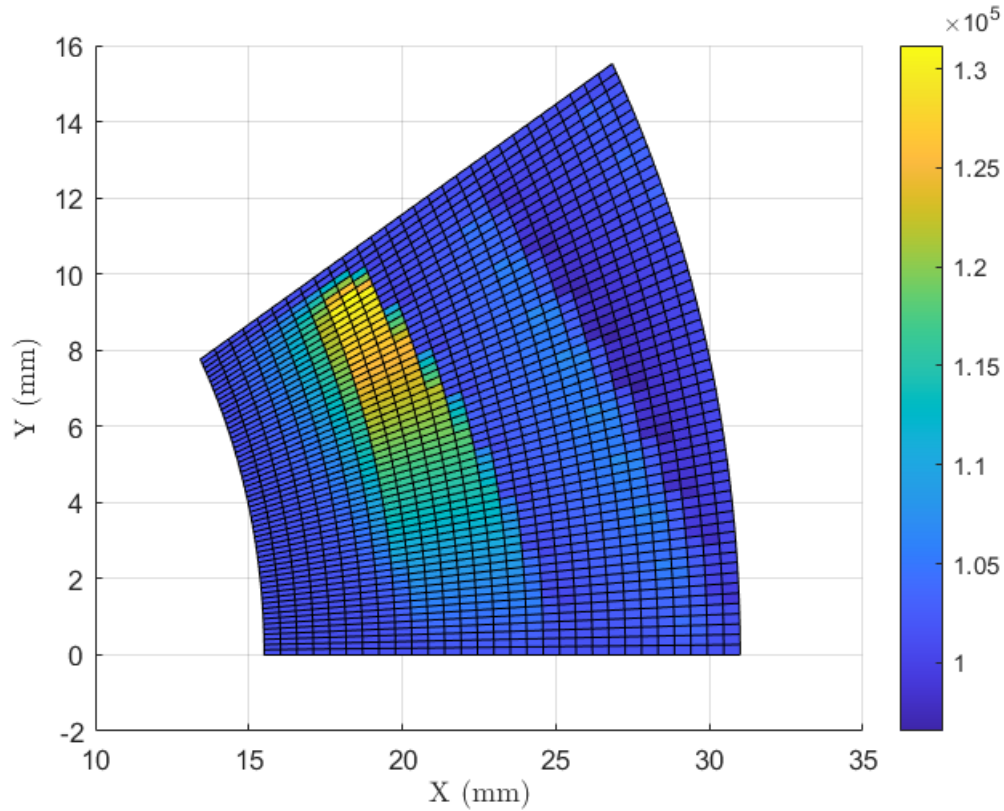


Figure 4.46: Top view of the pressure field of the studied spiral bearing section

The overall results for all air gap values and rotational speeds are presented in **Figure 4.47**. This figure clearly demonstrates how small variations in the air gap significantly influence the bearing's load capacity at each rotational speed. Specifically, as the air gap decreases, the pressure distribution intensifies, leading to a notable increase in the bearing's load-carrying capability. This trend is consistent with theoretical predictions, further validating the numerical model's reliability.

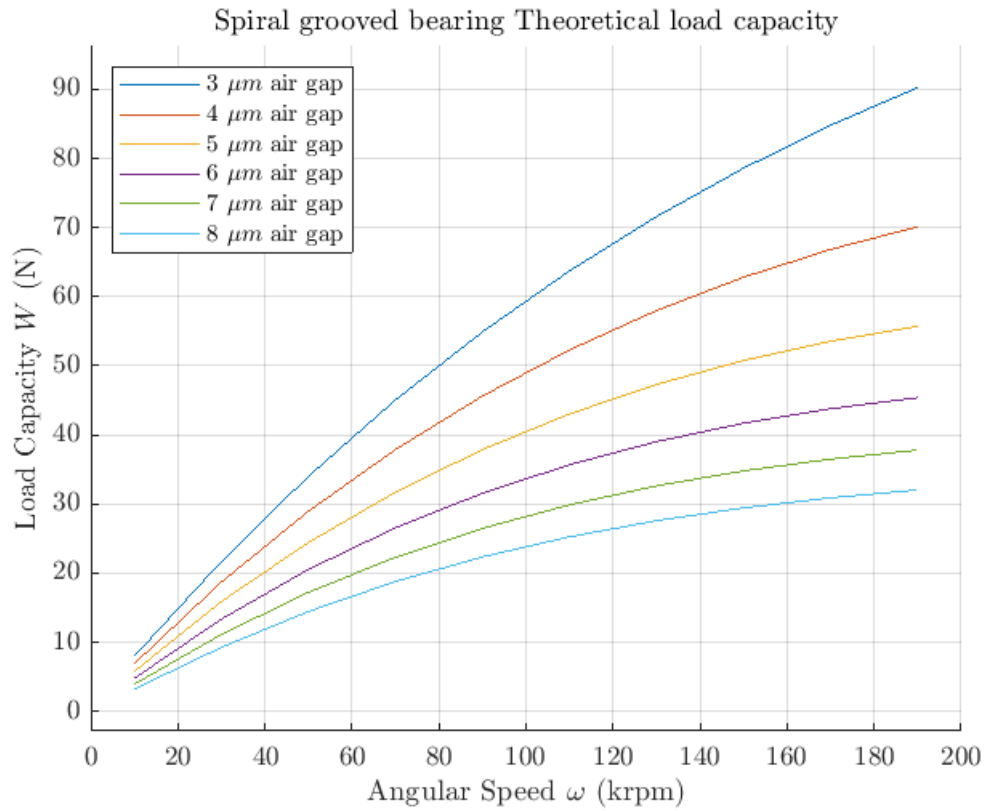


Figure 4.47: Spiral Thrust bearing theoretical load capacity under static conditions

Dynamic

Using the dynamic model introduced at the beginning of this chapter, the theoretical air gap in different load cases were obtained as seen in **Figure 4.48**.

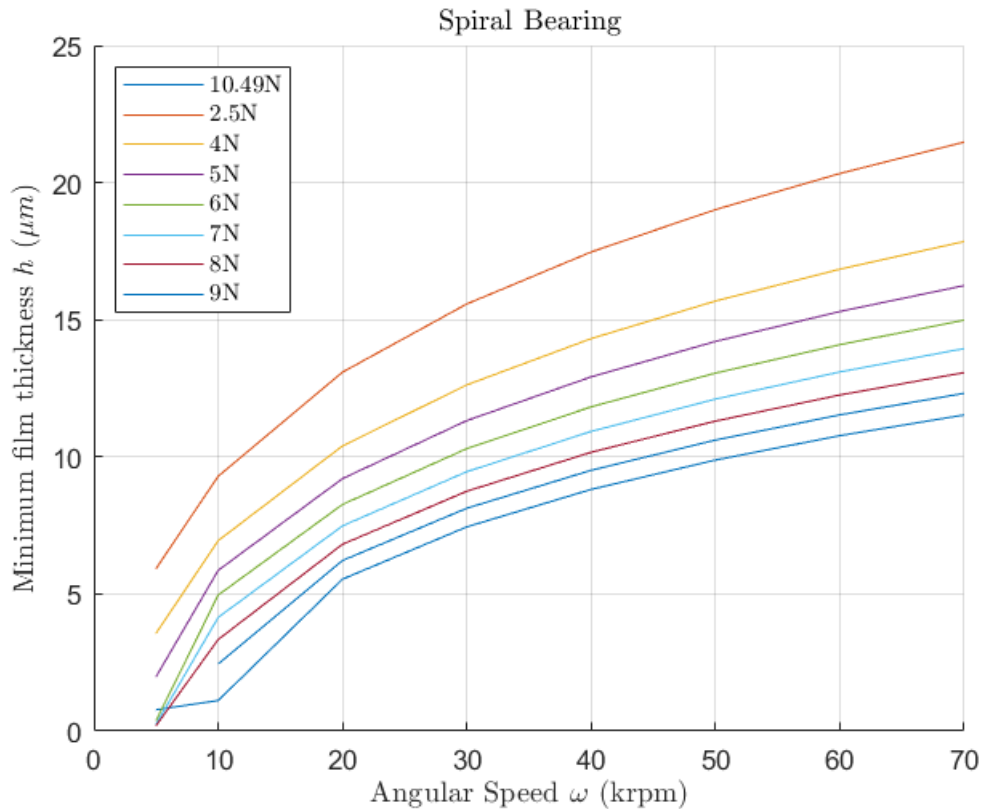
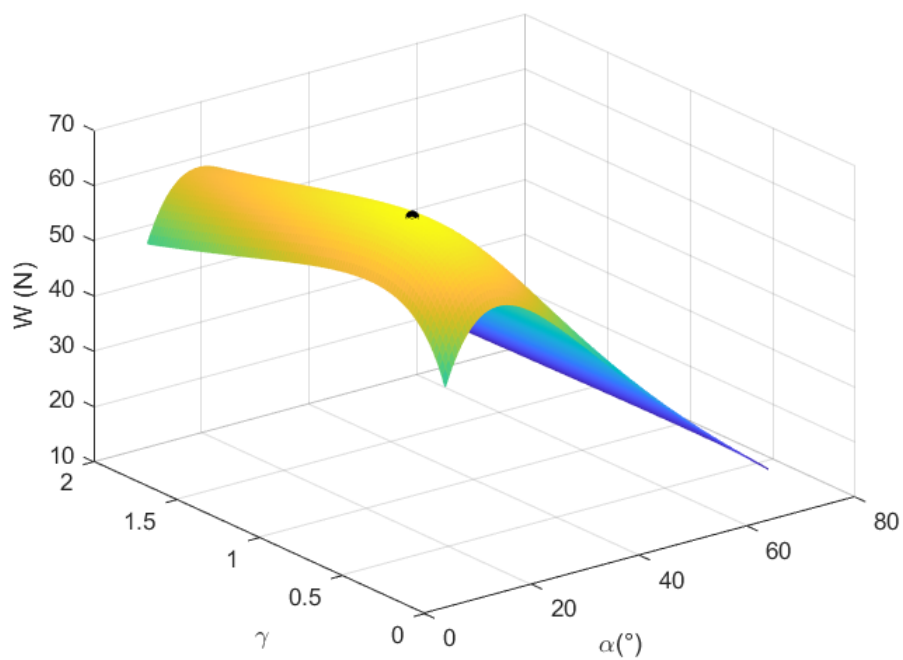
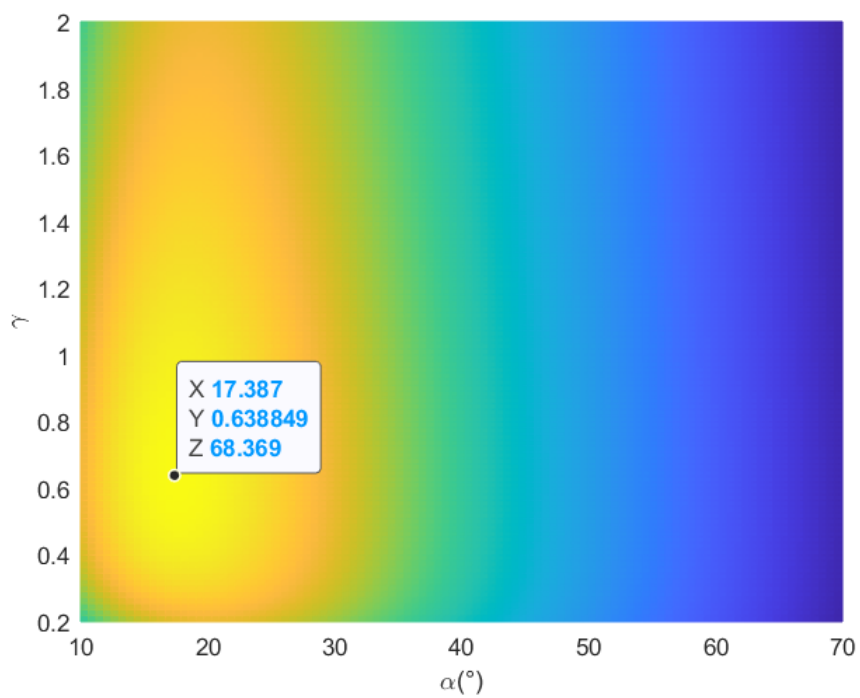


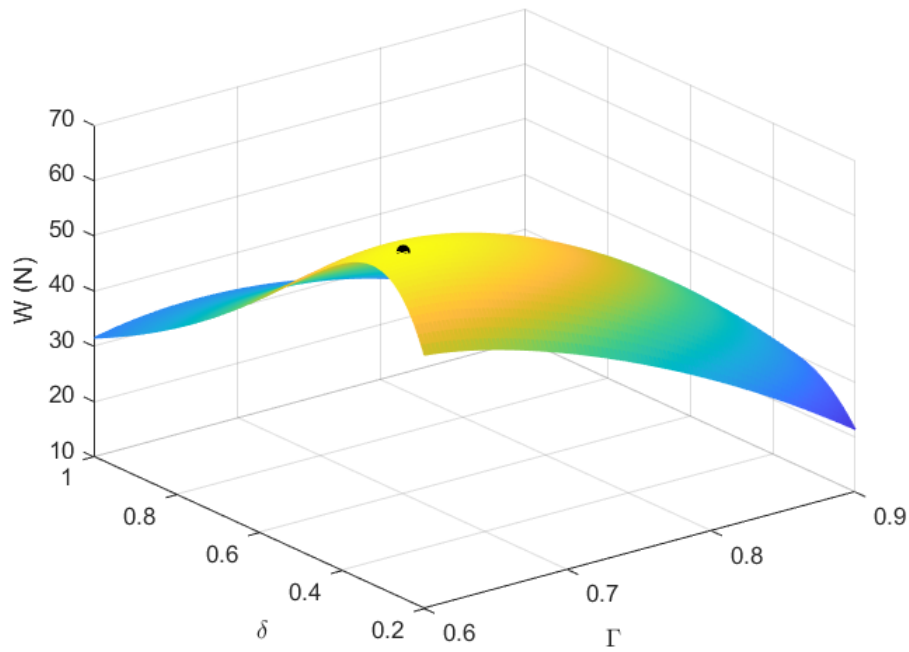
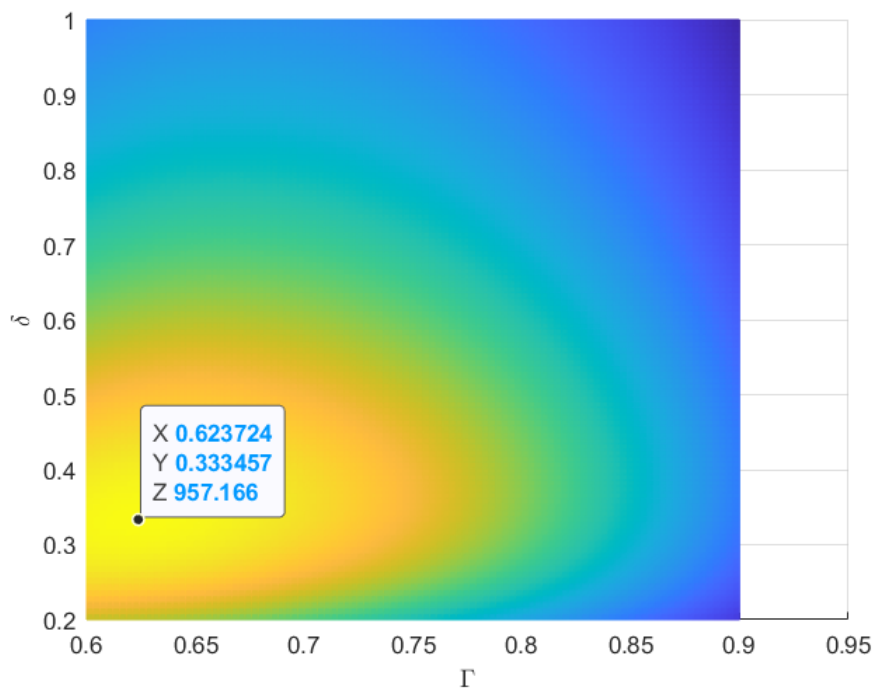
Figure 4.48: Spiral Thrust bearing theoretical load capacity under static conditions

Optimization

Muijderman [5, 4] studied the effect of incompressible air in the Whipple NGT [10, 11] theory and with some adjustments, such as considering grooves along a spiral curvature, arrived at a model that would simplify the numerical calculations of the model and thus could be calculated with a reasonable degree of accuracy. The main parameters of the system created by Muijderman are mostly dimensionless parameters. These parameters are, the spiral angle α , the ratio of nominal air gap to groove depth $\delta = \frac{h_2}{h_0}$, the ratio of groove sector to ridge sector $\gamma = \frac{a_2}{a_1}$ and the ratio of spiral base radius to external radius $\Gamma = \frac{r_b}{r_2}$.

Using the Muijderman model and the basic geometrical parameters of the studied spiral thrust bearing, these being the internal radius r_1 , external radius r_2 and the number of grooves k , more optimal parameters can be obtained. The results of this optimization can be seen in **Figures 4.49-4.52**.

Figure 4.49: Spiral bearing optimization for α and γ Figure 4.50: Spiral bearing optimization for α and γ , top view

Figure 4.51: Spiral bearing optimization for δ and Γ Figure 4.52: Spiral bearing optimization for δ and Γ , top view

By utilizing the parameters that yield the highest load capacity from **Figure 4.50** and **Figure 4.52**, along with the original geometry of the spiral bearing, the resulting optimized geometrical parameters are presented in Table 4.4.

h_0	15 mm
γ	0.64
β	72.61°
r_1	16 mm
r_b	20.6 mm
r_2	33 mm

Table 4.4: Optimal parameters of the spiral bearing

Figures 4.53-4.54 illustrate the differences between the original and optimized geometries. The most noticeable distinction is the significantly narrower grooves in the optimized design, a characteristic commonly observed in this type of bearing. This narrowing enhances the compression effect within the fluid film, leading to improved performance and higher load-carrying capacity.

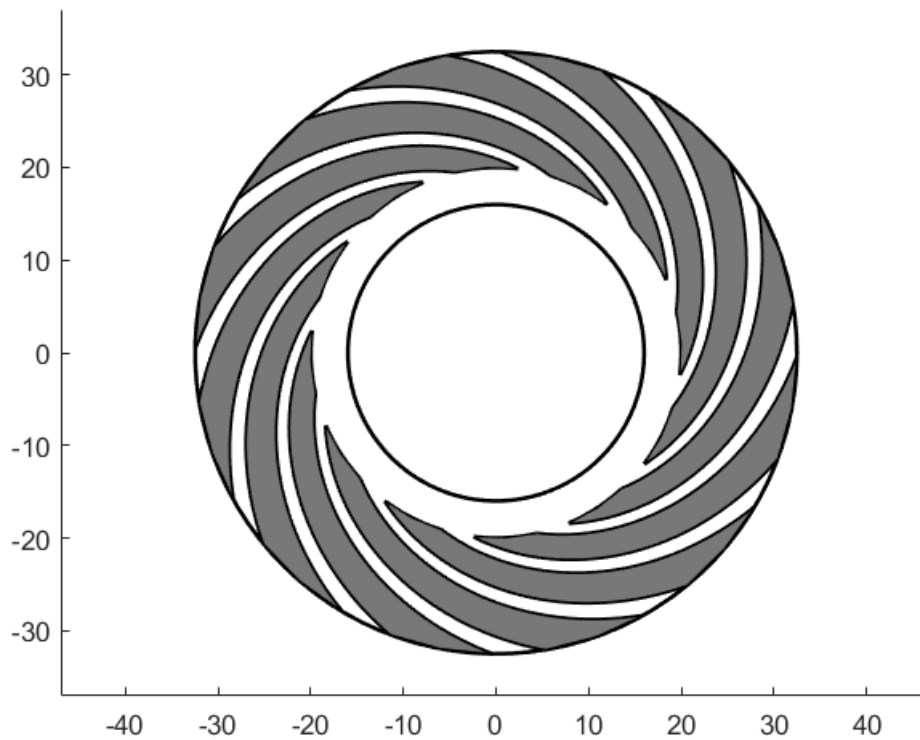


Figure 4.53: Original geometry

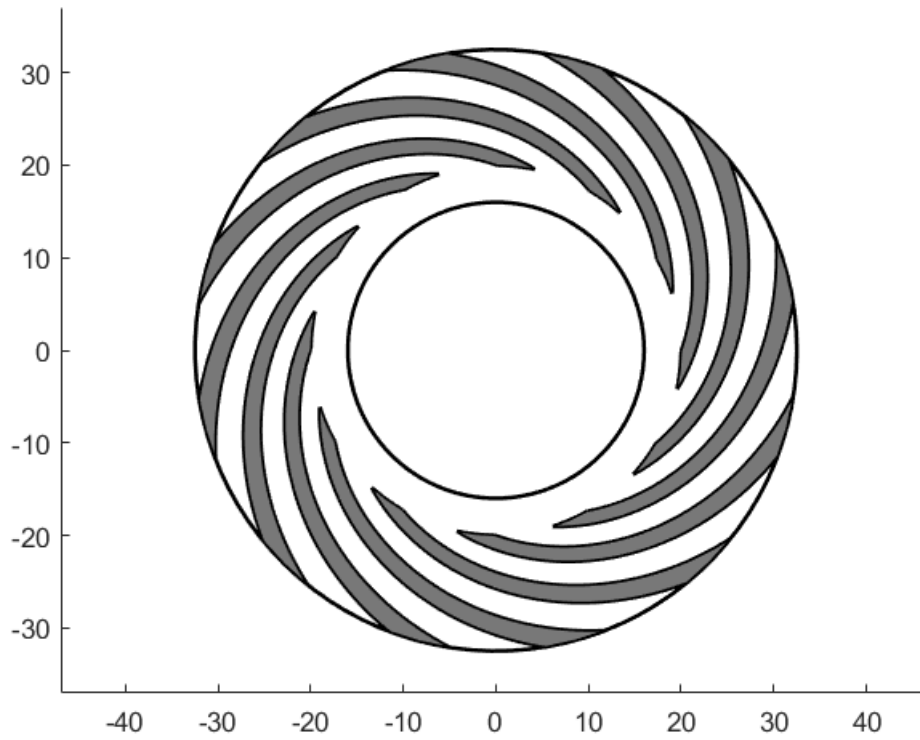


Figure 4.54: Optimized geometry

Using the parameters obtained from the Muijderman system optimization the calculations for the load capacity were done and compared with the original geometry. These results can be seen in **Figure 4.55**, and show how the new design of the spiral bearing is superior in every airgap studied.

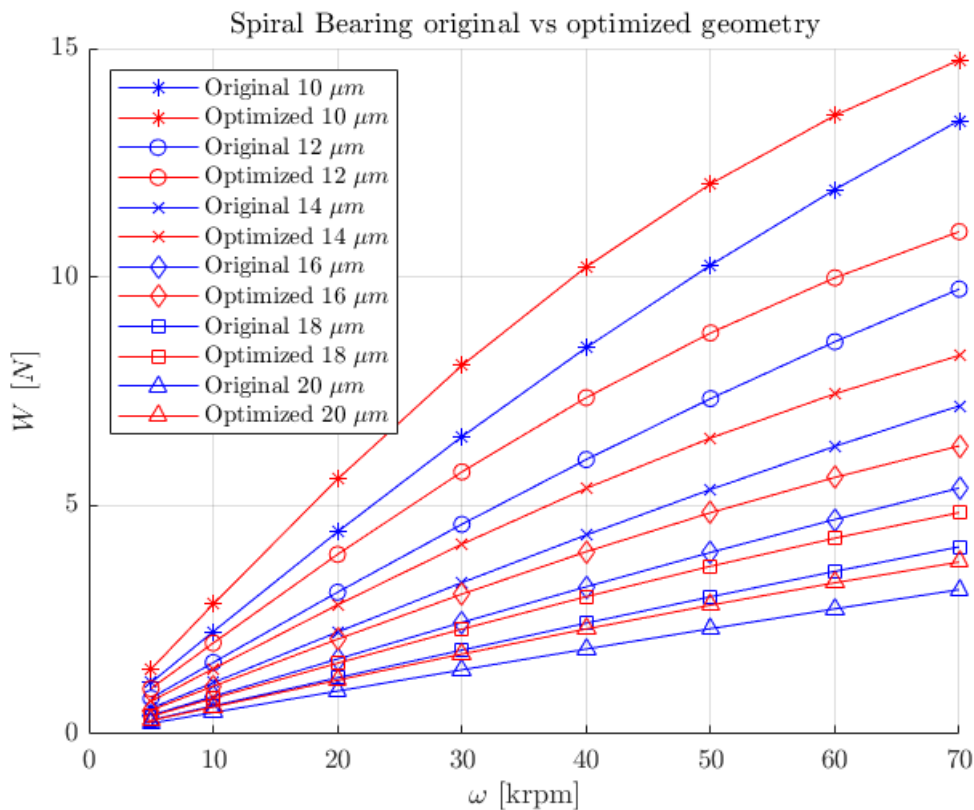
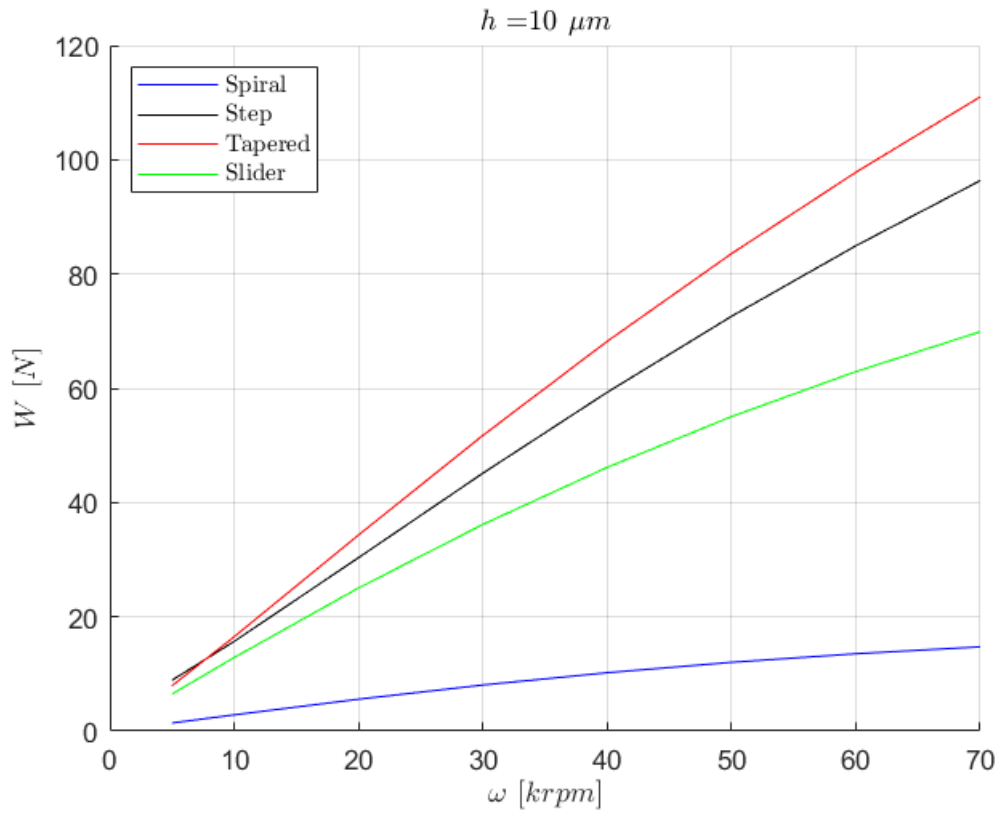
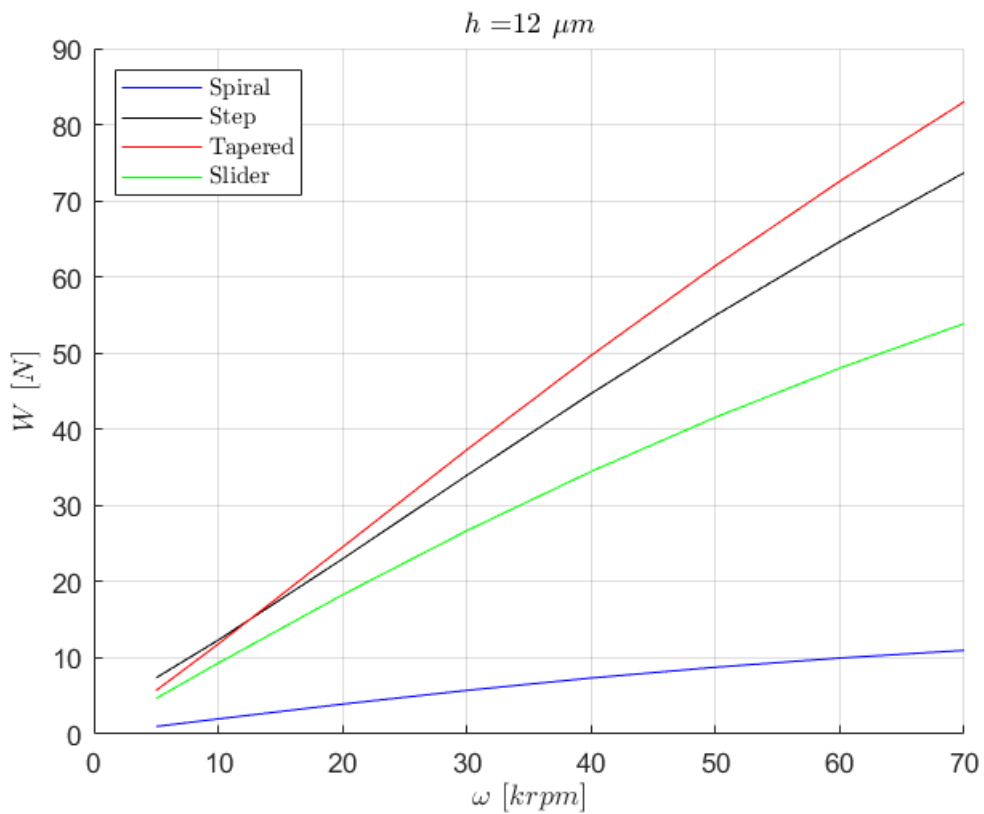


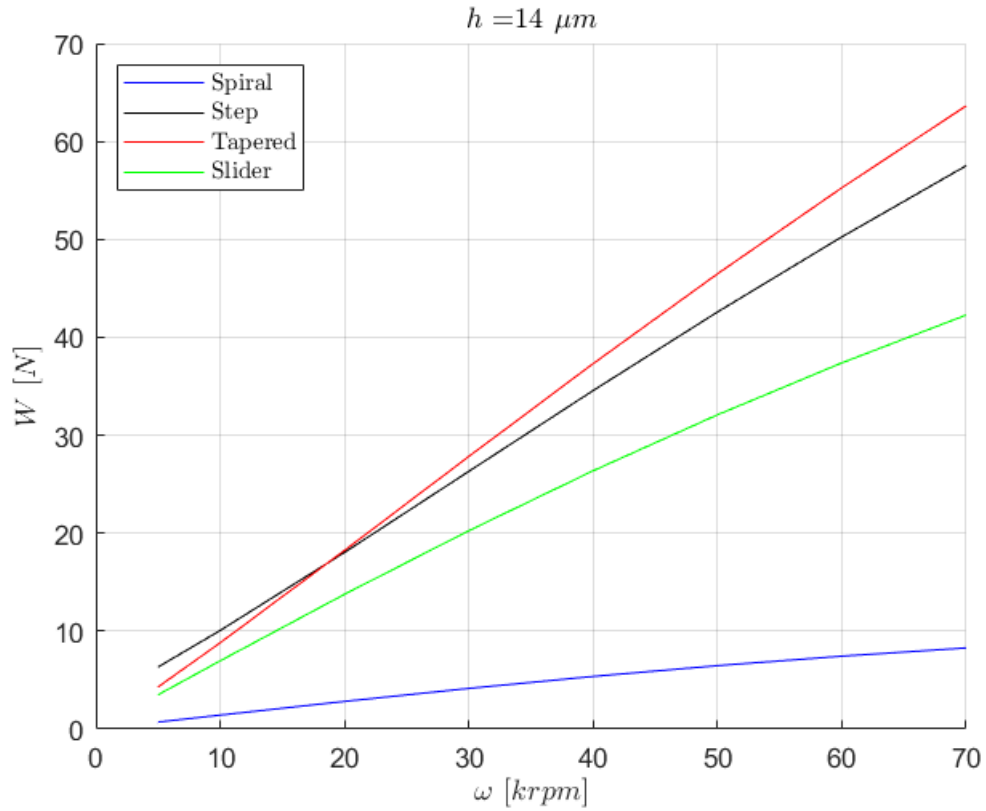
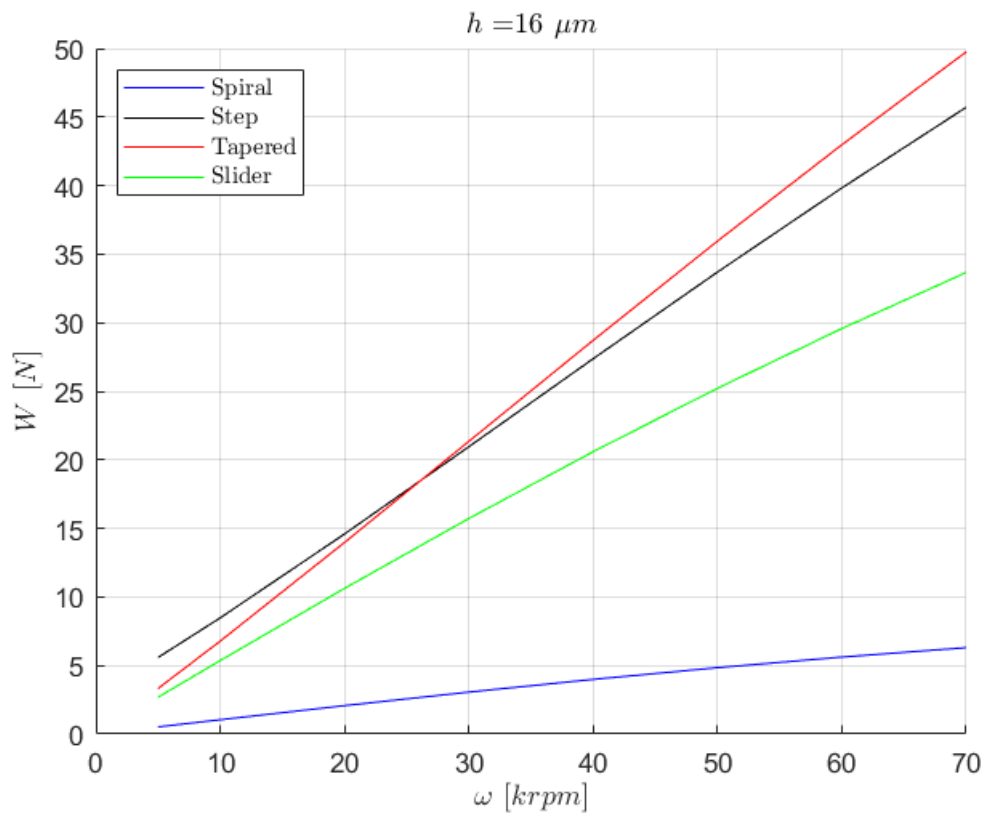
Figure 4.55: Original geometry vs optimized geometry

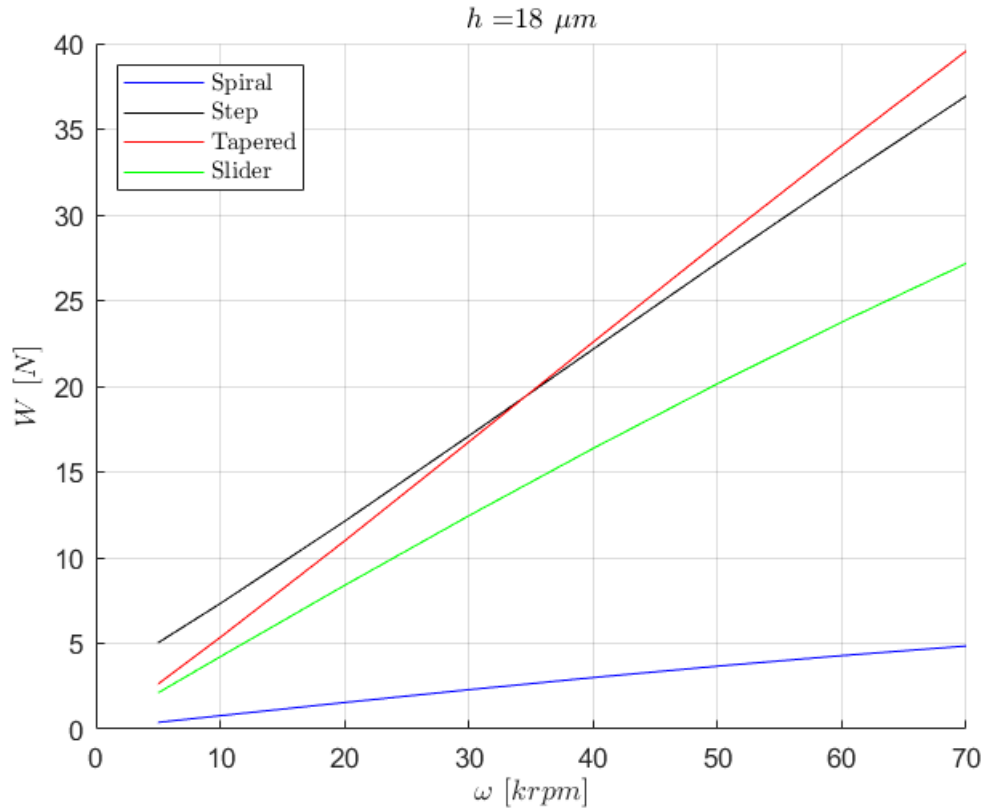
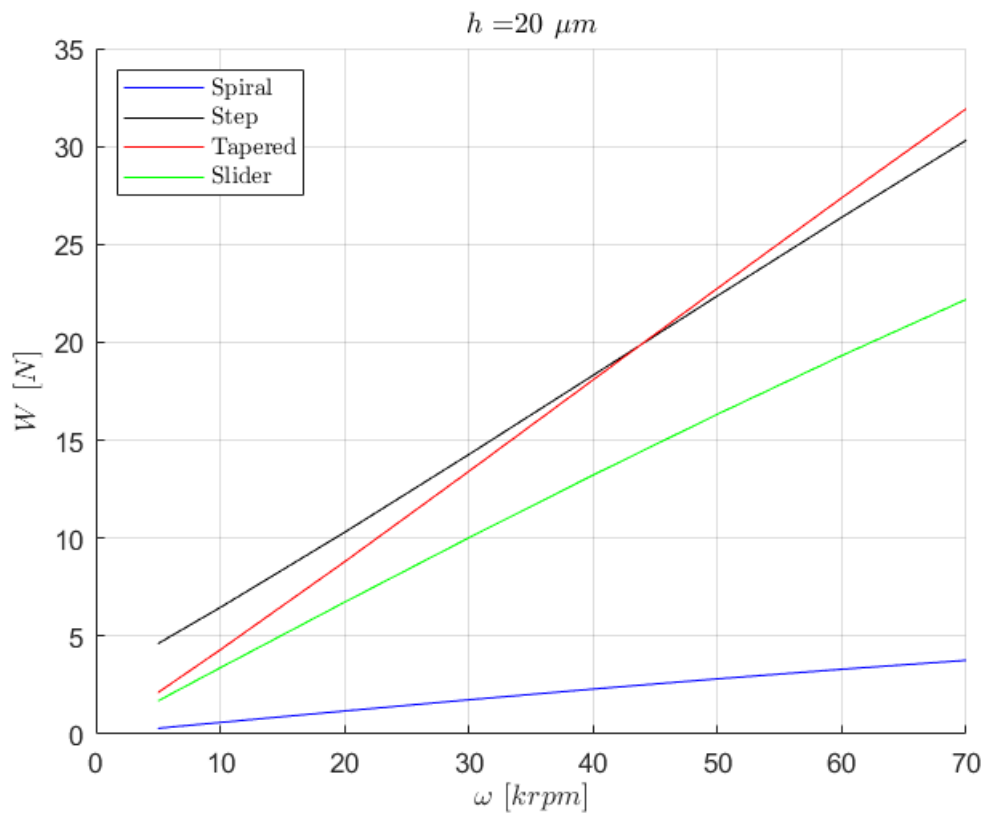
4.2.6 Comparisons

With all the optimized geometries obtained, a comparison of the different bearing types was conducted using the static model. For this analysis, rotational speeds were varied between $\omega_{min} = 5 \text{ krpm}$ and $\omega_{max} = 70 \text{ krpm}$, while the air gap ranged from $h_{2,min} = 10 \mu\text{m}$ to $h_{2,max} = 20 \mu\text{m}$, with a step of $\Delta h = 2 \mu\text{m}$. The results are shown in **Figures 4.56-4.61**. From these figures, it is evident that, under the analyzed conditions, the Step and Tapered bearings exhibit the best performance across all cases. Additionally, as the air gap increases, the speed at which the Tapered bearing surpasses the Step bearing in performance shifts toward a higher rotational speed. This suggests that for lower-speed applications, a Step bearing may be more suitable, whereas at higher rotational speeds, a Tapered bearing would be the preferred choice.

What is more, the spiral bearing in all the simulated results performs considerably worse than the other studied geometries even when the optimized parameters were used. One reason for this, as suggested by Malanoski and Pan[3], could be the number of grooves as they conclude that the best performing spiral thrust bearing is one that presents 18 grooves.

Figure 4.56: Bearing type comparison, $h_2 = 10 \mu m$ Figure 4.57: Bearing type comparison, $h_2 = 12 \mu m$

Figure 4.58: Bearing type comparison, $h_2 = 14 \mu m$ Figure 4.59: Bearing type comparison, $h_2 = 16 \mu m$

Figure 4.60: Bearing type comparison, $h_2 = 18 \mu m$ Figure 4.61: Bearing type comparison, $h_2 = 20 \mu m$

Chapter 5

Conclusions

This study focused on the analysis and optimization of aerodynamic thrust bearings, specifically logarithmic spiral and tapered geometries, through both experimental characterization and numerical modeling. The main objectives were to identify and characterize the bearings, validate numerical models using test bench data, and optimize their geometry to improve performance. A finite difference numerical model, utilizing a central-node finite volume mesh and a forward Euler scheme for time evolution, was developed to simulate the pressure distribution and load capacity of the bearings under varying operating conditions. Moreover, this study aimed to analyze the present, existing test bench in order to improve its design for future projects and versions.

The results demonstrated a strong correlation at higher speeds at lower loads, between experimental measurements and numerical simulations, confirming the validity of the proposed models when more adequate working conditions are met. The static model effectively predicted steady-state pressure distributions, while the dynamic model successfully captured the transient response of the air gap under an applied external load. The study found that bearing performance is highly sensitive to geometric parameters, particularly groove width, groove depth, and angular sector. Among the simulated configurations, the tapered bearing exhibited the best load-carrying capacity at higher rotational speeds, while the step bearing proved to be more efficient at lower speeds. Additionally, the optimization process revealed that narrower grooves for the logarithmic spiral bearing improved the compression effect, further enhancing bearing performance.

The findings of this study highlight the importance of precise geometric optimization in aerodynamic bearing design. By refining groove dimensions and distribution, significant improvements in load capacity and efficiency can be achieved. These insights are particularly relevant for high-speed, oil-free turbomachinery applications, where minimizing friction and maximizing stability are critical design considerations.

Despite the relative success of the numerical models, certain limitations should be acknowledged. The simulations assumed isothermal conditions, neglecting potential thermal effects that could influence gas film behavior at high speeds. Additionally, minor assembly misalignments in the test bench could introduce small uncertainties in the experimental measurements. Addressing these factors in future studies would further improve model accuracy and predictive capability.

Future work could explore the inclusion of thermal effects in the numerical model to account for temperature variations in high-speed applications. Further experimental

validation using different gas compositions and alternative bearing materials could also provide deeper insights into optimizing performance under various operating conditions. Additionally, refining the test bench to enhance measurement accuracy and reduce setup uncertainties would improve data reliability. Moreover, an overhaul of the loading mechanism would greatly improve the research possibilities of the test bench. Such mechanism could be the one used by LaTray *et al.*[2], which consisted of a pneumatic actuator that directly applied a load to the shaft.

Overall, this study provides a comprehensive evaluation of aerodynamic thrust bearings, offering valuable insights for their design, optimization, and practical implementation in high-performance rotating systems. The results serve as a foundation for further advancements in the field, contributing to the development of more efficient and reliable gas-lubricated bearing technologies.

Bibliography

- [1] Carlo Ferraresi and Terenziano Raparelli. *Meccanica Applicata*. CLUT, forth edition, 2007.
- [2] Nguyen LaTray and Daejong Kim. Design of novel gas foil thrust bearings and test validation in a high-speed test rig. *Journal of Tribology*, 142(7):071803, 03 2020.
- [3] S. B. Malanoski and C. H. T. Pan. The static and dynamic characteristics of the spiral-grooved thrust bearing. *Journal of Basic Engineering*, 87(3):547–555, 09 1965.
- [4] E. A. Muijderman. Analysis and design of spiral-groove bearings. *Journal of Lubrication Technology*, 89(3):291–305, 07 1967.
- [5] E.A. Muijderman. Spiral groove bearings. *Industrial Lubrication and Tribology*, 17(1):12–17, 1965.
- [6] M.T. Neves, V.A. Schwarz, and G.J. Menon. Discharge coefficient influence on the performance of aerostatic journal bearings. *Tribology International*, 43(4):746–751, 2010.
- [7] Aaron M. Rimpel, Giuseppe Vannini, and Jongsoo Kim. A rotordynamic, thermal, and thrust load performance gas bearing test rig and test results for tilting pad journal bearings and spiral groove thrust bearings. *Journal of Engineering for Gas Turbines and Power*, 139(12):122501, 08 2017.
- [8] Abraham Schneider. Dynamic modeling of high-speed impulse turbine with elastomeric bearing supports. *Massachusetts Institute of Technology*, 2003.
- [9] Tobias Waumans. On the design of high-speed miniature air bearings: dynamic stability, optimisation and experimental validation. 2007.
- [10] R TP Whipple. Theory of the spiral grooved thrust bearing with liquid or gas lubricant. Technical report, Great Britain Atomic Energy Research Establishment, Harwell, Berks, England, 1951.
- [11] R T.P. Whipple. The inclined groove bearing. Technical report, United Kingdom Atomic Energy Authority. Research Group. Atomic Energy Research Establishment, Harwell, Berks, England, 10 1958.

Chapter 6

Annex

```
1 function [ang,ang1,isGroove] = GetGrooves(r1,r2,x_spiral,y_spiral,n_grooves,beta,delta_beta,R,Theta)
2 % FUNCTION TO IDENTIFY THE LOCATIONS OF LOGARITHMIC SPIRAL GROOVES IN A 2D CIRCULAR MESH
3 %
4 % Inputs:
5 % GEOMETRY DEFINED ACCORDING TO MUIJDERMAN NOTATION:
6 % r1 [m] - Innermost radius of the bearing
7 % r2 [m] - Outer radius of the bearing
8 % x_spiral [adim] - Ratio of groove widths (a1/a2)
9 % y_spiral [adim] - Normalized groove position, defined as (r2-rb)/(r2-r1)
10 % n_grooves - Number of spiral grooves
11 % beta [°] - Base angle of the logarithmic spiral
12 % delta_beta [°] - Phase shift of the spiral with respect to the 0° reference line
13 % R [m] - Array of radial coordinates (MxN)
14 % Theta [°] - Array of angular coordinates (MxN)
15
16 % Outputs:
17 % ang - Array containing the angular position of the logarithmic spiral groove at different radii
18 % ang1 - Array containing the angular position of the second boundary of the groove
19 % isGroove - Logical array of the same size as the input mesh, where 'true'
20 % (1) indicates a groove region and 'false' (0) indicates a land region
21
22 isGroove = false(size(R)); % Initialize logical array for groove locations
23 Theta = Theta - pi; % Shift the angular domain to be within [-pi, pi] for consistency
24
25 %% LOGARITHMIC GROOVE GEOMETRY
26 passo = 2.*pi.*r2./n_grooves; % Circumferential pitch (spacing) of grooves
27 delta_theta = passo./r2; % Angular separation between grooves
28 a2 = passo./(1+x_spiral); % Groove width (a2) based on given ratio
29 a1 = passo-a2; % Complementary land width (a1)
30 b = y_spiral.*(r2-r1); % Radial position of the base of the groove
31 rb = r2-b; % Base radius of the grooves (starting point of the spiral)
32 beta = beta/180*pi; % Convert beta from degrees to radians
33
34 % Generate logarithmic spiral curves for the groove boundaries
35 r = linspace(rb,r2,100); % Radial discretization for the spiral
36 angle = -tan(beta).*log(r./r2) - delta_beta; % Logarithmic spiral equation for first boundary
37 angle1 = angle + a1./r2; % Second boundary of the groove (phase-shifted)
38
39 % Define radial points where grooves start within the mesh
40 R_logic = R(1,R(1,:))>=rb; % Extract radial coordinates where r >= rb
41 [~,pos] = min(abs(R(1,:)-rb)); % Find column index where r = rb
42
43 % Compute angular positions of groove boundaries for these radial points
44 angle_logic = -tan(beta).*log(R_logic./r2) - delta_beta;
45 angle1_logic = angle_logic + a1./r2;
```

```

47 %% GROOVE IDENTIFICATION
48 % Initialize arrays to store angular values for each groove
49 ang = zeros(length(angle),n_grooves);
50 ang1 = zeros(length(angle1),n_grooves);
51
52 % Adjust boundary angles for each groove iteration
53 angle_logic = angle_logic - delta_theta;
54 angle1_logic = angle1_logic - delta_theta;
55
56 for i = 1:n_grooves
57     % Define angular positions for the current groove
58     ang(:,i) = angle + (i-1) * delta_theta;
59     ang1(:,i) = angle1 + (i-1) * delta_theta;
60     angle_logic = angle_logic + delta_theta;
61     angle1_logic = angle1_logic + delta_theta;
62
63     % Ensure angular values remain within the [-pi, pi] domain
64     angle_logic(angle_logic>pi) = angle_logic(angle_logic>pi) - 2*pi;
65     angle1_logic(angle1_logic>pi) = angle1_logic(angle1_logic>pi) - 2*pi;
66
67     % Identify cases where the groove transitions across the -pi to pi boundary
68     pos_log = angle_logic > 0 & angle1_logic < 0;
69     if ~isempty(find(pos_log, 1))
70         % If a groove crosses the angular boundary, handle it separately
71         pos_log = find(pos_log);
72         Theta_log = [false(size(Theta,1),pos-1), ...
73                     Theta(:,pos:end) > angle_logic & Theta(:,pos:end) < angle1_logic];
74
75         Theta_log = Theta_log | [false(size(Theta,1),pos+pos_log(1)-2), ...
76                                 Theta(:,pos_log) > angle_logic(pos_log) | Theta(:,pos_log) < angle1_logic(pos_log), ...
77                                 false(size(Theta,1),size(Theta,2)-pos_log(end)-pos+1)];
78
79     else
80         % Standard case where groove does not cross the angular boundary
81         Theta_log = [false(size(Theta,1),pos-1), ...
82                     Theta(:,pos:end) > angle_logic & Theta(:,pos:end) < angle1_logic];
83     end
84
85     % Update the global logical array, ensuring that only regions inside the groove are marked
86     isGroove = isGroove | Theta_log;
87     isGroove = isGroove & (R >= rb);
88 end
89
90 end

```